Rational Design of Cadmium Sulfide based Nano-hybrid Materials: Synthesis, Characterization and Evaluation of Photocatalytic Properties for Efficient Hydrogen Generation and Organic Dye Degradation

A Dissertation Submitted to the
Indian Institute of Technology Guwahati
As Partial Fulfillment for the Degree of

DOCTOR of PHILOSOPHY

by

Ziyauddin Khan
Roll No: 08612211

Department of Chemistry
Indian Institute of Technology
Guwahati – 781039 (INDIA)
May 2012

STATEMENT

I hereby declare that this thesis entitled, “**Rational Design of Cadmium Sulfide based Nano-hybrid Materials: Synthesis, Characterization and Evaluation of Photocatalytic Properties for Efficient Hydrogen Generation and Organic Dye Degradation”** is the outcome of research work carried out by me under the supervision of Dr. Mohammad Qureshi, at the Department of Chemistry, Indian Institute of Technology Guwahati, India.

In keeping with the general practice of reporting scientific observations, due acknowledgement has been made whenever work described here has been based on the findings of other investigators.

IIT Guwahati

May 2012

Ziyauddin Khan

Candidate

Dr. Mohammad Qureshi
Assistant Professor
Department of Chemistry
Indian Institute of Technology, Guwahati
781036 – India
Tel: +91 – 361 – 2582320; Fax: +91 – 361 – 2582349
Email: mq@iitg.ernet.in

Certificate

Certified that the work described in this thesis entitled "**Rational Design of Cadmium Sulfide based Nano-hybrid Materials: Synthesis, Characterization and Evaluation of Photocatalytic Properties for Efficient Hydrogen Generation and Organic Dye Degradation**" by Mr. Ziyauddin Khan, Department of Chemistry, Indian Institute of Technology Guwahati has been carried out under my supervision and has not been submitted elsewhere for a degree.

Guwahati
May 2012

Mohammad Qureshi
Thesis supervisor
Department of Chemistry
Indian Institute of Technology
Guwahati
Guwahati – 781039

DEPARTMENT OF CHEMISTRY
INDIAN INSTITUTE OF TECHNOLOGY GUWAHATI, INDIA

Certificate

This is to certify that Mr. Ziyauddin Khan has satisfactorily completed all the courses required for the Ph. D. degree. The courses include:

CH 603	Supramolecules: Concepts & Application
CH 621	New Reagents for Organic Synthesis
CH 601	Physical Methods in Chemistry
CH 639	Principles and Applications of Molecular Fluorescence

Mr. Ziyauddin Khan was admitted to the candidacy for Ph.D. degree in 2009 after he successfully completed the oral qualifying examination.

Head of Department,
Chemistry

ACKNOWLEDGEMENTS

Over the last four years of my graduate school time at IITG, I have learned great things not only about science and academics, but also about the life, the truth and the faith. It was a quite tough lesson especially in the beginning, but I have to say I have truly enjoyed every moment of learning and I am so grateful to have these kinds of experience in my life. I believe this is possible only because of all the people supporting me in many ways and I would like to acknowledge them.

First of all, I would like to thank my mentor and Sir, **Dr. Mohammad Qureshi**, for all the support and guidance throughout the years. He gave me many opportunities, which were very important to build up my academic career, and he was always supportive whenever I proposed new research topics or brought some problems of ongoing study or even personal matter. I also thank to the committee members Dr. G. Krishnamoorthy, Dr. A. N. Panda, Dr. C. V. Sastri and Dr. M. Sarma from Chemistry. Also, I want to thank my collaborator Dr. Mahuya De and Mr. N. Vinothkumar from Department of Chemical Engineering, to help me when I started my first research works in their lab. Prof. A. T. Khan gave me helpful comments not only for my research, but also for my future academic career.

Thanks of appreciation to my lab group Momina, Arkalekha, Tridip and Dipankar for their assistance and keeping the lab in good humor during my graduate school time. I really had a wonderful time working in our lab CHL 103 and sincere thanks goes to Rajen Kundu, Sangeeta, Subhashis, Suman, Afsana and Manoj for their co-operation in work and sharing light moments with them. I take the opportunity to thank my seniors and friends Dr. Shams Tabrez, Dr. S. K. Bharadwaj, Dr. Sahoo, Dr. Musawwer, Dr. Nihar, Dr. Rupam and many others who have already completed their work. I also wish to thank my friends Salahuddin, Pramod, Manoj, Dr. Bashar, Kasem, Zaki, Parwaz, Sana, Anil, Saroj, Faizi Bhai, Palashuddin, Raihana, Anu, Julfikar, Barman, Kaka, Rajat Bhiyya, Tarique, Himanshu Bhiyya, Ashif and many others for their help and support.

I am lucky to have friends Tushar, Amit, Sahil, Manab and Shashank. Special thanks to them for their unconditional support and all the help they extended from time to time whenever required either professional or personal. Without the frequent brainstorming tea breaks and relaxing weekly parties with these people it wouldn't have been possible for me to finish. I am very much thankful to all of you for making my stay pleasant at IIT Guwahati.

I want to thank all my friends whose name is not mentioned and hostel mates whom I met during these four years of life for their help and encouragement. Thanks to Ganesh Da and Bani Mandir tea stall who supplied countless cups of tea for novel ideas throughout these years. I wish to thank Mr. Madhurjya, Mr. Chandan, Mr. Senapati and Mr. Kaustav for their constant help in collecting SEM, FE-SEM, TEM and powder X – ray data.

Hearty thanks to Simran, to bear with me for so long throughout these years and for all the fun and fight I share with her. Simran encouraged me a lot during my struggling time.

Finally, I don't have words to express my profound gratitude to my Parents (Mrs. Isakul Khan & Mr. Zaheeruddin Khan), brother and sisters for their support, patience, love and wish.

The financial assistance and facilities provided by the Indian Institute of Technology, Guwahati, are duly acknowledged.

Zia

Synopsis

Thesis Title: Rational Design of Cadmium Sulfide based Nano-hybrid Materials: Synthesis, Characterization and Evaluation of Photocatalytic Properties for Efficient Hydrogen Generation and Organic Dye Degradation

Name of the Student: Ziyauddin Khan

Roll Number: 08612211

Department: Chemistry

Thesis Supervisor: Dr. Mohammad Qureshi

Degree for which submitted: Doctor of Philosophy

Chapter 1 presents the basic concepts and literature survey of the photocatalytic water splitting. Brief overviews on the synthesis of efficient photocatalytic materials for hydrogen generation as well as for dye degradation by the different methodologies are discussed.

Chapter 2 presents the detailed synthesis of CdS based hybrid photocatalysts and their characterization. Special interest is given to the description of in-house built photocatalytic measurement set-up along with the gas chromatographic (GC) instrumentation. This chapter also demonstrates the detailed experimental procedure for hydrogen generation and organic dye degradation. We have explained the method for the calculation of apparent quantum yield for hydrogen generation. A brief description of the freeze-thaw cycle preformed for the mechanistic (for the presence of intermediate, such as superoxide radical) study of dye degradation is also discussed.

Chapter 3 Divided in two parts:

Chapter 3A presents the results of the investigations due to the enhanced specific surface area and the coupling effect of Al_2O_3 and ZnO wide band gap materials with that of CdS on photocatalytic activity. 3D Al_2O_3/CdS and ZnO/CdS exhibits enhanced photocatalytic activity for hydrogen generation with apparent quantum yields (AQY) of 11% and 15% respectively. The high hydrogen production rate of ZnO/CdS is mainly attributed to the enhanced surface area and the facile charge transfer between CdS and ZnO (scheme 1). 3D Al_2O_3/CdS and ZnO/CdS show highly efficient dye degradation in comparison to that of 1D CdS NWs. The kinetic study of methyl orange degradation is carried out and found to follow first order kinetics with apparent rate constant 0.032 min^{-1} for 3D Al_2O_3/CdS and 0.053 min^{-1} for 3D ZnO/CdS. The evidence for the formation of superoxide radical anion ($O_2^{\cdot -}$) and hydroxyl radical (•OH) were performed using freeze-thaw cycle.

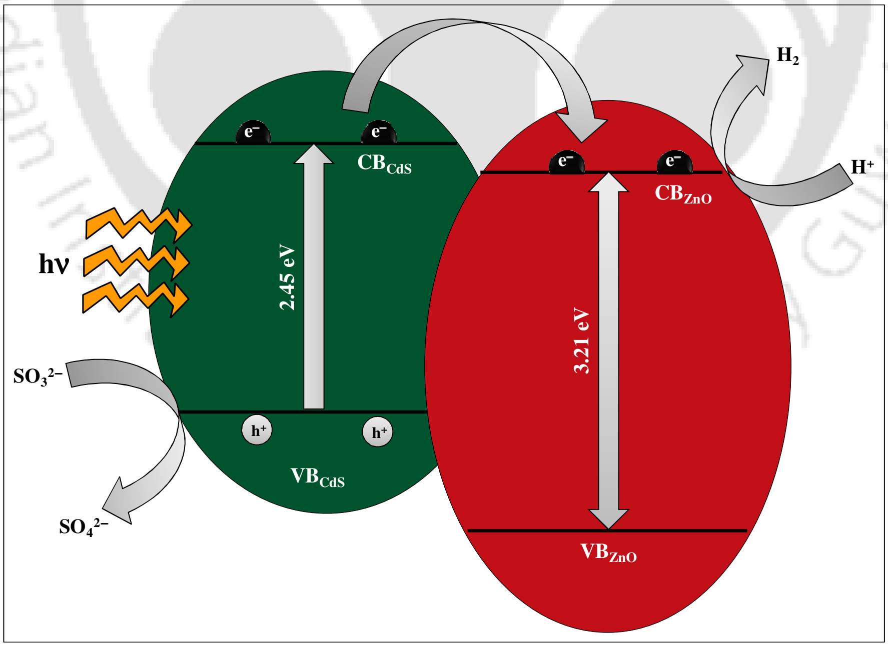

Scheme 1 Schematic illustration of the efficient electron transfer and the band energy positions of ZnO and CdS in the hierarchical 3D ZnO/CdS binary heteroarrays

Chapter 3B describes the effect of enhanced specific surface area and facile charge transfer on the photocatalytic activity. As prepared 3D NiO/CdS show high efficiency for photocatalytic hydrogen generation with an apparent quantum yield (AQY) of 6% in comparison to that of 1D CdS nanowires (NWs) and bulk CdS under visible light irradiation. The enhanced hydrogen production rate in 3D NiO/CdS is attributed to the high specific surface area and facile charge transfer from conduction band (CB) of CdS to CB of NiO due to the favorable energy alignments of CB of CdS and CB of NiO (scheme 2).

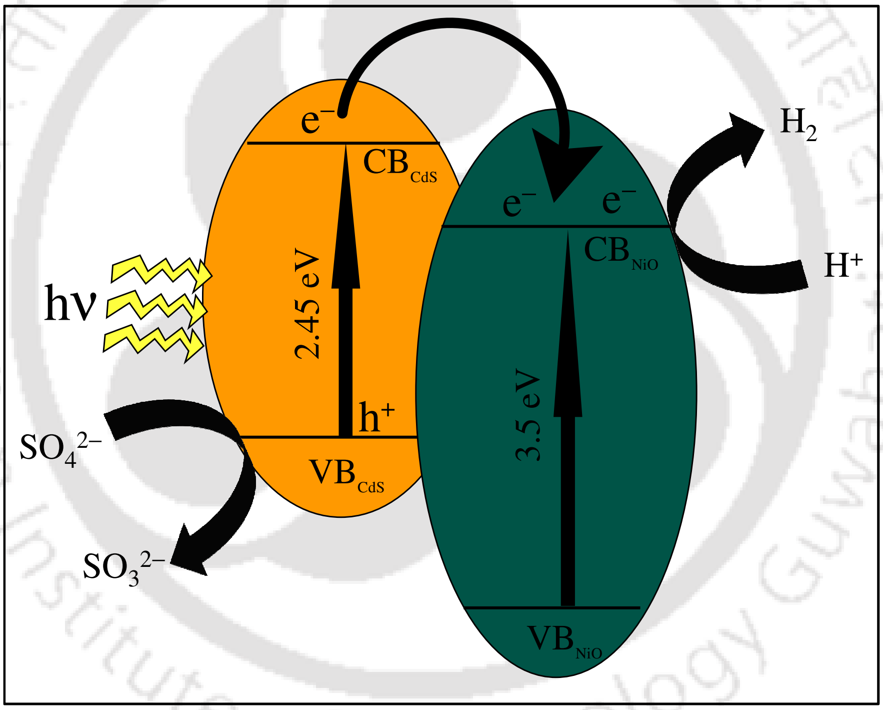

Scheme 2 Schematic illustration of the efficient electron transfer and the band energy positions of NiO and CdS in the hierarchical 3D NiO/CdS binary heteroarchitecture, under visible light irradiation

Chapter 4 describes the effect of enhanced specific surface area and facile charge transfer on photocatalytic activity under UV-Vis irradiation. As synthesized hierarchical 3D SrS/CdS show high efficiency for hydrogen generation with an apparent quantum yield

(AQY) of 10% and ~ 100% methyl orange dye degradation in comparison with 1D CdS NWs, SrS nanoparticles and bulk CdS under UV-Visible light irradiation. The enhance photocatalytic activity of 3D SrS/CdS is attributed to high specific surface area and facile charge transfer from CB of SrS to CB of CdS due to the favorable energy alignments of CB of SrS and CB of CdS (scheme 3). Mechanistic study of dye degradation involving the intermediates such as superoxide radical anion ($O_2^{\cdot -}$) and hydroxyl radical (•OH) were explained.

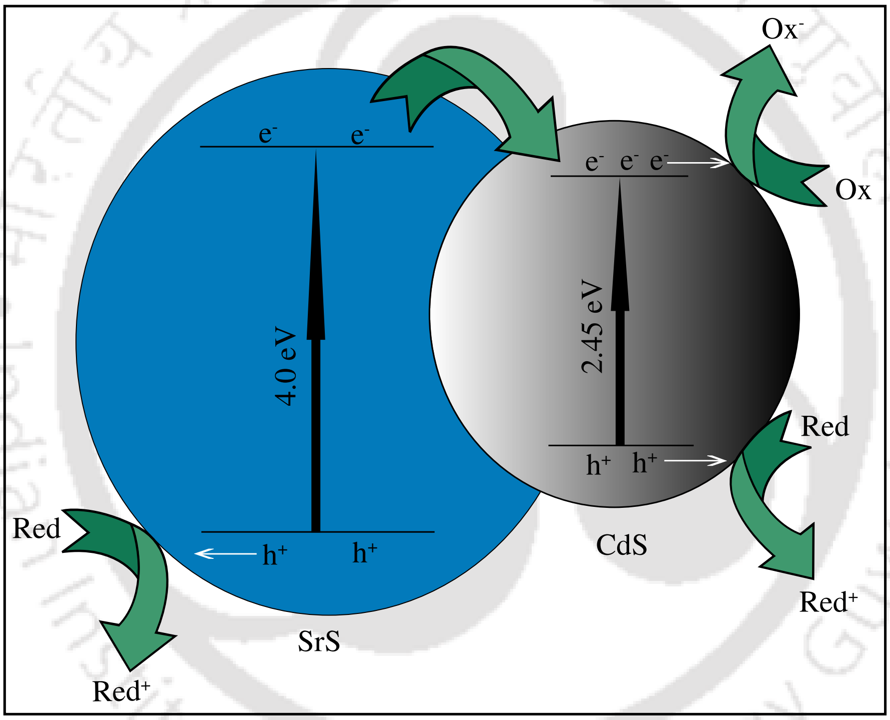

Scheme 3 Schematic presentation of efficient charge transfer, band position of SrS and CdS in hierarchical 3D SrS/CdS heteroarrays under UV-Vis light irradiation

Chapter 5: In this chapter we have demonstrated a single step hydrothermal synthesis of CdS/Metal Oxide (MO = ZnO, Al_2O_3) and examine their photocatalytic activity in presence of graphene oxide. CdS/Al_2O_3/GO and CdS/ZnO/GO both exhibits enhanced photocatalytic activity for hydrogen generation with apparent quantum yields (AQY) of

14% and 30% respectively. Moreover, CdS/MO/GO displayed efficient photodegradation of organic dye; ~ 90% for CdS/Al_2O_3/GO and ~99% for CdS/ZnO/GO. The high photocatalytic activity of CdS/MO/GO is attributed to the presence of graphene oxide which provides large surface area for effective mass transfer and facile charge transfer that reduces the recombination rate of photoinduced charge carriers (scheme 4). The present study highlights the potential application of graphene based materials in the field of energy conversion and environment remediation.

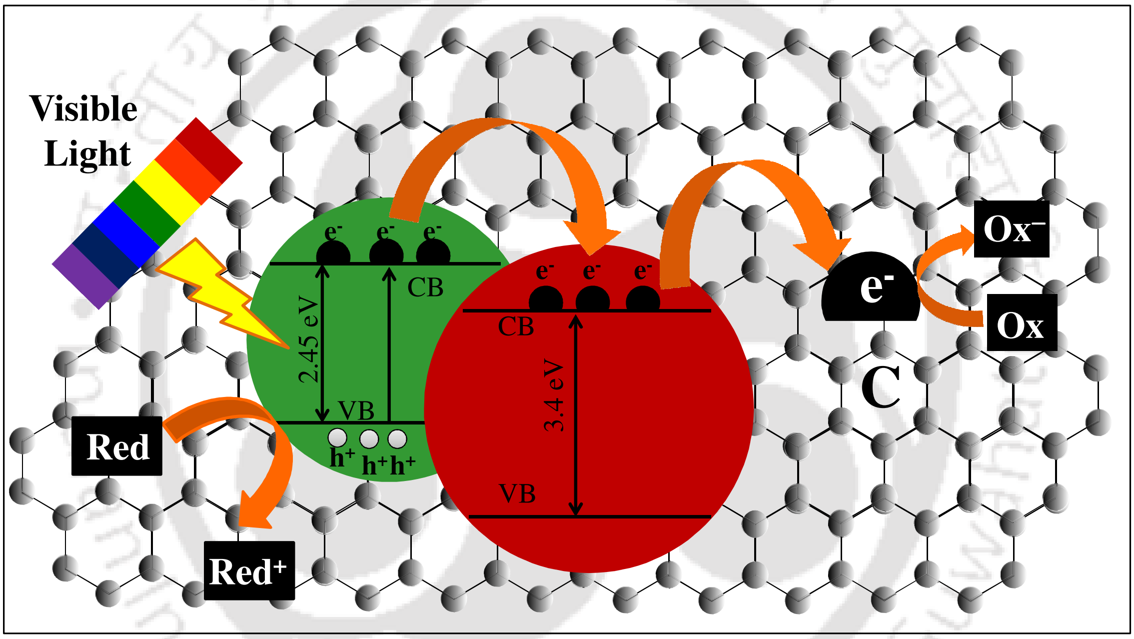

Scheme 4 Schematic presentation of efficient charge transfer, band position and redox processes involve in CdS/ZnO/GO under visible light irradiation

Dedicated to

My Parents

Contents

List of Figures

List of Tables

List of Schemes

Chapter 1

Introduction

This chapter presents the basic concepts and literature survey of the photocatalytic water splitting. Brief overviews on the synthesis of efficient photocatalytic materials for hydrogen generation as well as for dye degradation by the different methodologies are discussed.

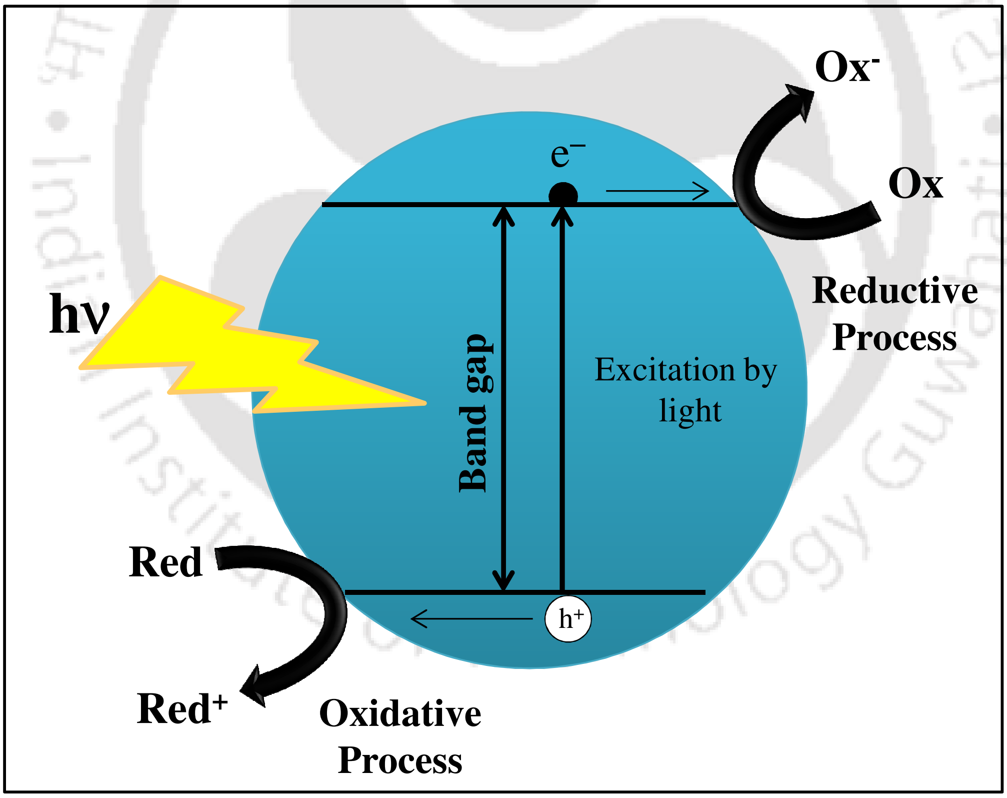

1.1. Overview of the Importance and Demand for Hydrogen

Energy and environmental issues are rife and prominent at global level.[1-3] Currently, world is dealing with two great tasks: Exhaustion of the world's fossil fuel reserves and rising environmental pollution. Therefore, it is very essential to design materials which can resolve these global environmental challenges. The semiconductor materials have scavenging activity which could either be through degradation of organic pollutants or by enabling clean energy production in the form of hydrogen. In terms of environmentally sustainable energy, hydrogen has captivated the scientific community extensively because of its high energy density (117.61 MJ/kg) and eco-friendly nature. Hydrogen combustion yields only water with tremendous amount of energy. Due to these reasons, hydrogen has been recognized as an ideal solution to the energy related environmental problems for future perspective.[1,4] Hydrogen can be produced from a variety of sources such as natural gas, heavy oil, methanol, biomass, coal and solar wind.[5-8] However, at present, large scale hydrogen is produced by reforming of the fossil fuels.[5,9] Since many decades hydrogen is being produced by steam reforming of hydrocarbons and used in industries either as pure gas or in the production of ammonia or methanol.[9,10,11]

$$CH_4 + H_2O \longrightarrow CO + 3H_2 \qquad (1)$$

$$CO + H_2O \longrightarrow CO_2 + H_2 \qquad (2)$$

However, this process involves consumption of fossil fuel and emission of huge amount of carbon dioxide thereby increasing the environmental pollution. In the view of efficient energy generation and carbon free environment, hydrogen can be produced from water using solar irradiation because sun is the most abundant energy system on the planet (in one hour more energy strikes the earth from sun than is consumed on the planet in a year i.e. 14 TW).[5] There are several ways for solar hydrogen production such as electrolysis of water using solar cell, photocatalytic or photoelectrochemical water splitting. Among which the photocatalytic water splitting fascinates much attention because it is a simple, inexpensive and highly efficient process.

In 1972, Honda and Fujishima first discovered the solar hydrogen production by photoelectrochemical water splitting on n-type TiO_2 electrodes.[12] They have demonstrated that on irradiation of UV light on TiO_2 electrons and holes are generated as shown in Figure 1.1. Briefly, on Pt electrode, the photogenerated electron reduces water to hydrogen while the hole oxidizes water to oxygen on TiO_2 electrode on applying the external bias.

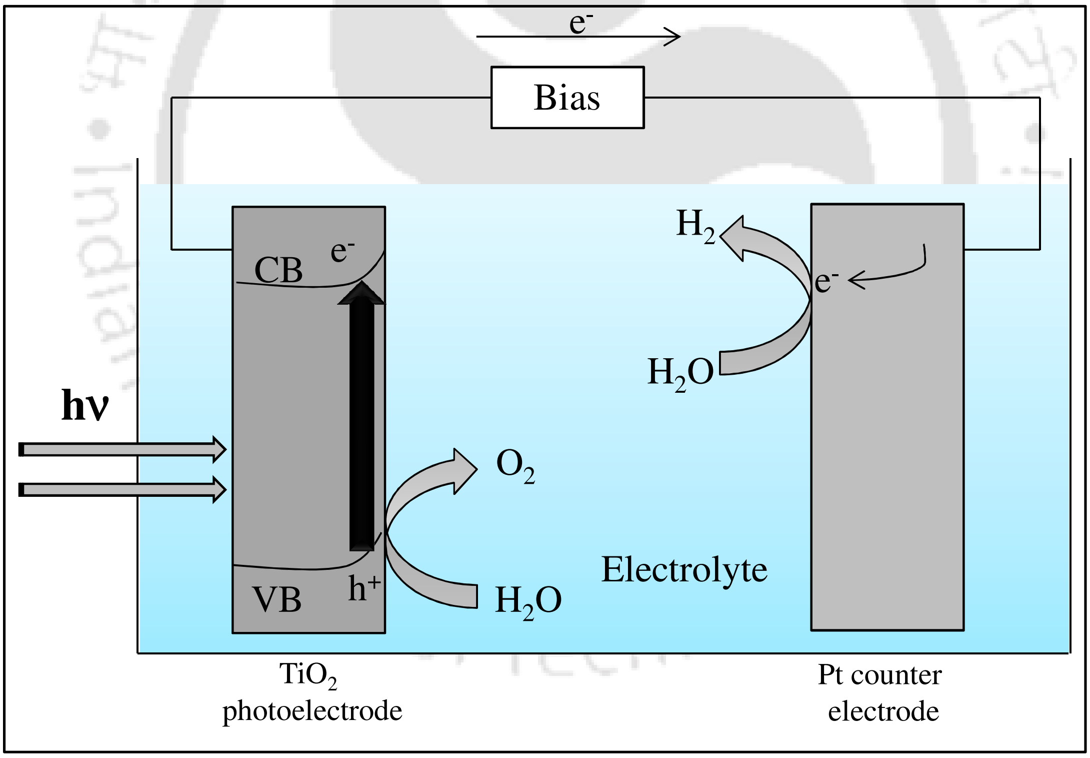

Figure 1.1 Schematic of solar hydrogen generation using a TiO_2 photo-electrode by Honda *et al.*[12]

This work has encouraged the research for hydrogen production by water splitting reaction using semiconductor photocatalysts and considered as one of the most important approaches to solve the world energy crisis.[13] After the successful demonstration of overall water splitting by Honda and Fujishima, semiconductor based photocatalytic water splitting reaction was first realized in 1980 by Lehn *et al.*,[14] Sato and White[15] and Domen *et al.*[16] who observed the stoichiometric evolution of hydrogen and oxygen. Since, then many articles including reviews and books have been published in the field of photocatalytic water splitting performance.[17-33]

1.2. General Mechanism for Semiconductor Photocatalysis

Photocatalysis can be initiated by electron-hole pairs, after the bandgap excitation in semiconductors.

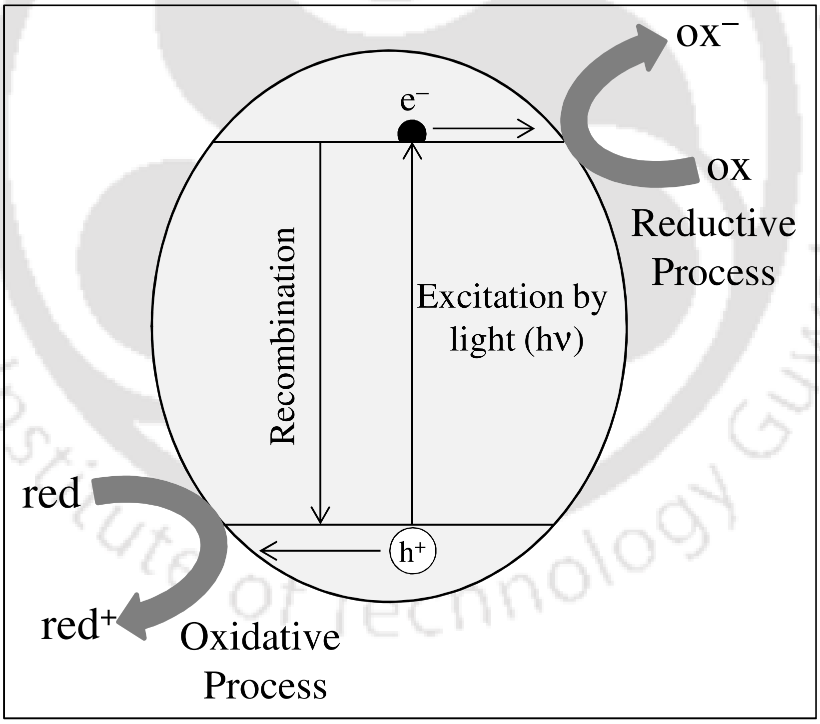

Figure 1.2 Schematic of the general mechanism in semiconductor photocatalysis

When a photocatalytic semiconductor is illuminated with light, electrons in the valence band (VB) of semiconductor will get excited to the conduction band (CB) while the holes are left behind in VB. This state is called photo-excited state of semiconductor. After photoexcitation, the electron-hole pairs can recombine, releasing the input energy as heat, with no chemical effect. However, if these electrons and holes are able to migrate onto the photocatalyst surface without recombination, they can undergo numerous redox reactions with the adsorbed species such as water, and other organic or inorganic species. These redox reactions are the elementary mechanism of photocatalytic hydrogen generation. A schematic representation of the photocatalytic process on semiconductor is depicted in Figure 1.2.

1.3. Basic Principles of Photocatalytic Water Splitting

For photochemical water splitting, catalysts can be used in two different modes (i) Photoelectrochemical cells and (ii) Powdered photocatalytic systems. In photoelectrochemical cells there exist two electrodes dipped in an aqueous electrolyte, one of which is semiconductor photocatalyst exposed to the light. On the other hand in powdered photocatalytic system, powder photocatalyst is dispersed in aqueous solution, in which each particle acts as photo-electrode. These electrodes are involved in both oxidation and reduction process on catalyst surface. However, the advantage of powdered photocatalytic system is that this system is much simple, inexpensive and efficient in comparison to the photoelectrochemical cell.[5]

Elementary mechanism for water splitting on powdered photocatalyst system is presented in Figure 1.3. The main processes involved in the photocatalytic water splitting are discussed below

(i) Absorption of photons by the semiconductor followed by the generation of excited charges (reductive electrons and oxidative holes).

(ii) Recombination of the excited charges, separation of the excited charges, trap of excited charges, and migration of the photoinduced charges to the surface of reaction sites.

(iii) Reduction of adsorbed water molecules by reductive electron to hydrogen and oxidation to oxygen by oxidative hole at the surface of semiconductor.

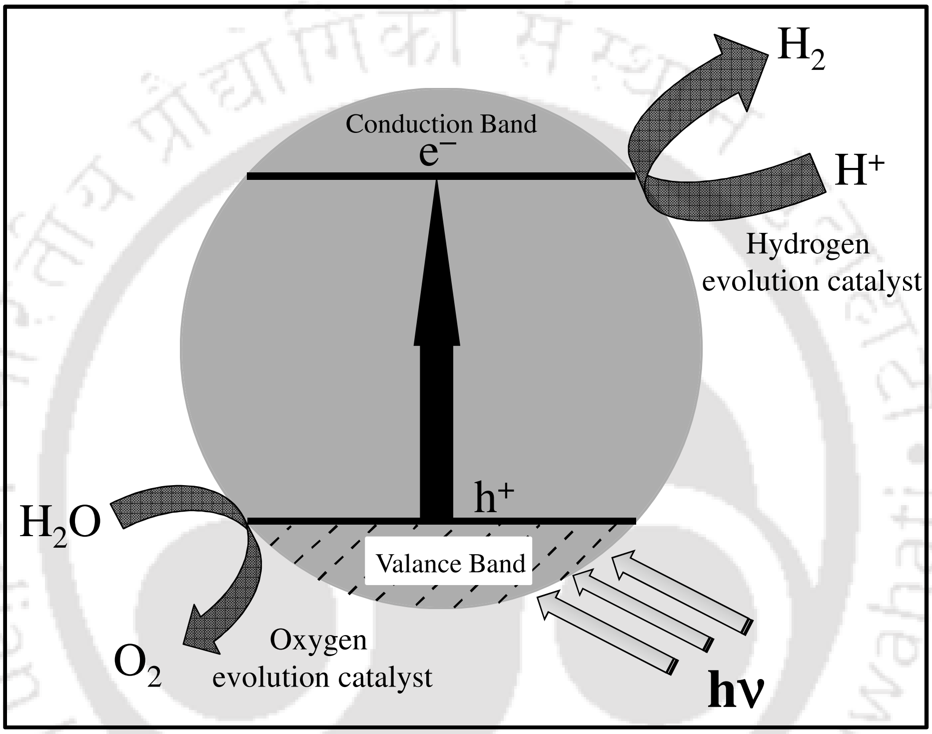

Figure 1.3 Schematic of basic mechanism of powdered photocatalyst for overall water splitting[33]

The overall water splitting reaction involves several steps for the generation of hydrogen and oxygen. Those steps are discussed below

$$\text{Semiconductor} + h\nu \longrightarrow e^{-}_{cb} + h^{+}_{vb} \quad (3)$$

$$\text{oxidation: } H_2O + 2h^{+}_{vb} \longrightarrow 2H^{+} + 1/2O_2 \quad (4)$$

$$\text{reduction: } 2H+ + 2e^{-}_{cb} \longrightarrow H_2 \quad (5)$$

$$\text{overall reaction: } H_2O \longrightarrow H_2 + 1/2O_2 \quad (6)$$

Water splitting into hydrogen and oxygen (shown in equation 7) is nonspontaneous reaction which requires the standard Gibbs free energy change ΔG° of 237 kJ/mol (1.23 eV).

$$H_2O \longrightarrow H_2 + 1/2O_2;\ \Delta G^{\circ} = +237 \text{ kJ/mol} \qquad (7)$$

Therefore, in order to achieve the overall water splitting, the minimum band gap energy of the photocatalyst should be > 1.23 eV (λ = 1000 nm, in the near infrared region). To assist the reduction and oxidation of water on photocatalyst surface by photo-excited reductive electrons and oxidative holes, match of the band gap and positions of CB and VB of the catalyst are critical. The CB and VB positions of various semiconductor materials are shown in Figure 1.4.

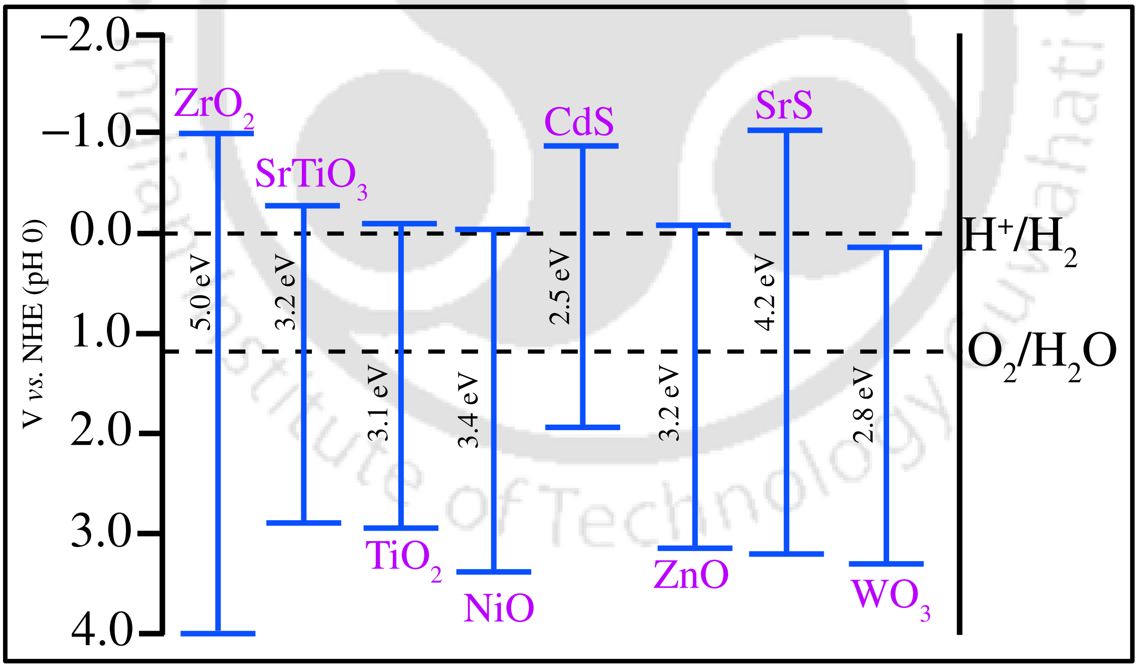

Figure 1.4 Graphic representation of band energy position of extensively used semiconductors for efficient hydrogen or oxygen generation by photocatalytic water splitting[9]

For hydrogen generation by the water reduction, the bottom of the CB of the semiconductor should be at more negative potential than $E_{red}(H^+/H_2)$, 0 V *vs.* NHE at pH

0, and top of the VB at the more positive value than $E_{ox}(H_2O/O_2)$, 1.23 V *vs.* NHE at pH 0. On the other hand for O_2 production by water oxidation the semiconductor photocatalyst requires that top of the VB should be more positive than the $E_{ox}(H_2O/O_2)$, 1.23 V $_{vs.}$ NHE at pH 0. From Figure 1.4, materials $SrTiO_3$, TiO_2, ZnO, CdS and NiO are the efficient photocatalysts due to their band positions which satisfies the thermodynamic requirement for overall water splitting. Although, CdS has a suitable band gap and band position for hydrogen generation by water reduction under visible light irradiation. CdS displays photocorrosion property in which S^{2-} in CdS is oxidized by photogenerated holes[34] as shown in the equation (8).

$$CdS + 2h^+ \longrightarrow Cd^{2+} + S \qquad (8)$$

However, in presence of any hole scavenger (electron donor such as alcohol, S^{2-}, SO_3^{2-} etc.), CdS exhibits excellent photocatalytic activity for hydrogen generation by water splitting. The band structure of a semiconductor is just a thermodynamic requirement but not a sufficient condition. Therefore, to design an efficient photocatalyst for hydrogen generation by water splitting suitable band engineering is essential. There are several factors which affect the photocatalytic hydrogen generation process like crystal structure, calcination temperature, crystallinity, surface area, recombination rate of charge carriers *etc.* but more precisely three factors which greatly affect the photocatalytic activity these are crystallinity, specific surface area and efficient charge separation. Higher the crystallinity, lower is the defects in the crystal structure. Defects act as trapping and recombination centers for photoinduced electrons and holes thereby leading decrease in photocatalytic activity. High surface area provides two fold advantages in photocatalytic activity, firstly, more number of reaction sites and secondly, the photoinduced electrons and holes have to migrate shorter distance to the reaction sites increasing the photocatalytic activity.

1.4. Photocatalytic H_2 or O_2 Evolution by Water Splitting

The photocatalytic activity of the semiconductor is frequently evaluated in the presence of reducing reagents (electron donor, such as sulfides, sulfites and alcohol *etc.*) or oxidizing reagents (electron acceptor, such as Ag^+, Fe^{3+}, persulfate) to assist water splitting process in order to produce hydrogen or oxygen.[9] These reagents are usually known as sacrificial reagents. The mechanism for the generation of H_2 and O_2 in presence of sacrificial reagents is schematically presented in Figure 1.5.

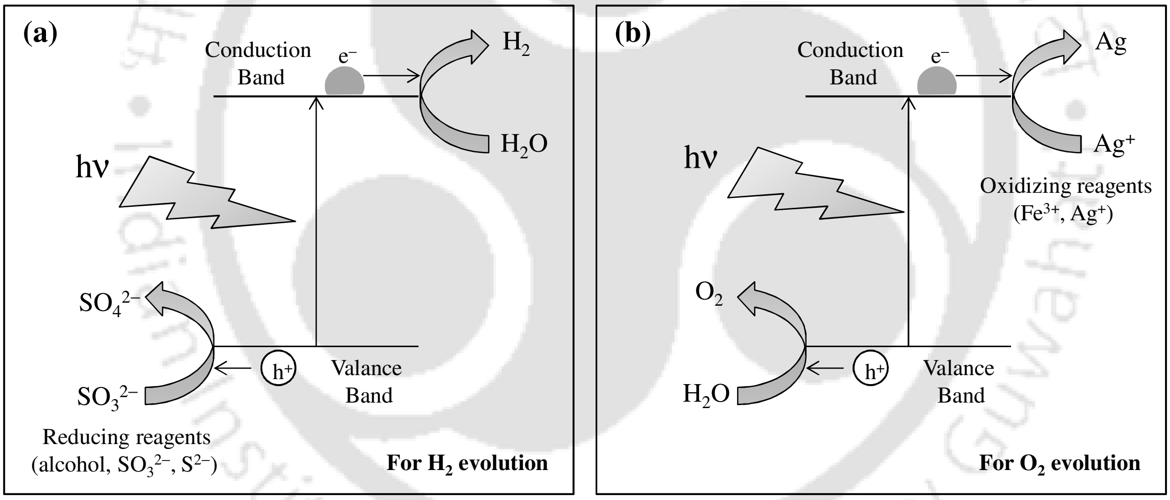

Figure 1.5 Photocatalytic (a) Evolution of H_2 (b) Evolution of O_2 by water splitting in presence of different sacrificial reagents[9]

When the photocatalytic water splitting reaction is carried out in presence of reducing reagents, the photoinduced holes oxidize the reducing reagent instead of water. It enhances the reductive electrons in the photocatalyst facilitating hydrogen evolution as shown in Figure 1.5 (a). In the similar fashion the photoinduced electrons in the CB of photocatalyst are consumed by oxidizing reagents thereby leading enhancement in the production of oxygen evolution as shown in Figure 1.5 (b). Therefore, the production of

H_2 and O_2 are regarded as half reactions of water splitting in presence of sacrificial reagents. The reaction that uses sacrificial reagents is not “overall” water splitting reaction but these reactions are often carried out to examine H_2 or O_2 evolution.[35-38]

In the literature, variety of photocatalysts for the generation of hydrogen and oxygen by water splitting, are present. Among them some photocatalysts are ultraviolet light driven and others are visible light driven photocatalyst which are discussed below:

1.5. Ultraviolet (UV) Light driven Photocatalyst for Water Splitting

A wide range of materials have been reported as photocatalyst under UV irradiation for water splitting in the literature, some of them are listed in Table 1.1. The UV light driven photocatalyst can be typically classified into four groups:

1- d^0 metal oxide photocatalyst (Ti^{4+}, Zr^{4+}, Nb^{5+}, Ta^{5+} and Mo^{6+})
2- d^{10} metal oxide photocatalyst (In^{3+}, Ga^{3+}, Ge^{4+} and Sn^{4+})
3- f^0 metal oxide photocatalyst (Ce^{4+})
4- non-oxide photocatalyst (ZnS, GaN)

Table 1.1 Overview of UV-light driven photocatalysts for H_2 and/or O_2 evolution by water splitting

photocatalyst	**synthetic method**	**co-catalyst**		**QY (%)**	**ref**
		H_2 evolution (µmol/h/g)	**O_2 evolution (µmol/h/g)**		
TiO_2 (anatase)	MCB TiO_2	Rh/1497	-	29	39
TiO_2 (anatase)	MCB TiO_2	NiO_x/32	NiO_x/48	-	40
TiO_2 (anatase)	P25 TiO_2	Pt/353	Pt/177	1.4	41

photocatalyst	synthetic method	co-catalyst		QY (%)	ref
		H_2 evolution (µmol/h/g)	O_2 evolution (µmol/h/g)		
TiO_2	hydrolysis	Pt/3300	-	-	42
colloid TiO_2	hydrolysis	Pt-RuO_2/4000	-	30	43
TiO_2 nanotubes	hydrothermal	285	-	-	44
TiO_2/SnO_2	polyol	Pd/83	-	-	45
$SrTiO_3/TiO_2$	solid state	560	-	-	46
$CaTiO_3$	-	Pt/76	Pt/18	-	47
$SrTiO_3$	-	NiO_x/70	NiO_x/32	-	33
ZrO_2	-	309	167	-	48
Zr-MCM-41	hydrothermal	224	-	-	49
$BaZrO_3$	Pechini process	522.5	131	3.7	50
$BaZr_{0.7}Sn_{0.3}O_3$	Pechini process	690	185	-	51
$NaNbO_3$	polymerized	RuO_2/650	RuO_2/160	-	52
$KNbO_3$	hydrothermal	Pt/5170	-	-	53
$Sr_2Nb_2O_7$	hydrothermal	RuO_2/475	RuO_2/220	32	54
Ta_2O_5	solid state	NiO_x/1154	NiO_x/529	-	55
$NaTaO_3$	hydrothermal	NiO/1700	NiO/822	-	56
$NaTaO_3$:La	solid state	NiO/19800	NiO/9660	56	37

photocatalyst	synthetic method	co-catalyst		QY (%)	ref
		H_2 evolution (µmol/h/g)	O_2 evolution (µmol/h/g)		
$CaTa_2O_6$	solid state	NiO/72	NiO/32	-	57
$SrTa_2O_6$	solid state	NiO/960	NiO/490	7	57
$SrSnO_3$	hydrothermal	Pt/8200	2500	-	58
Ga_2O_3:Zn	-	Ni/4100	Ni/2200	~20	59
GaN	NH_3 nitridation	$Rh_{2-x}Cr_xO_3$/63.3	$Rh_{2-x}Cr_xO_3$/31.7	0.7	60
ZnS	Precipitation	Pt/34037	-	90	61
InP	-	Pt/100	-	-	62

1.6. Methodologies to Develop Efficient Visible Light driven Photocatalysts

A large number of metal chalcogenides have been reported for photocatalytic hydrogen generation. Metal chalcogenides have bandgap corresponding to the UV and visible region, but researchers have focused on the synthesis of visible light driven photocatalysts, because of more than ten-fold contribution of visible light in the solar spectrum, in contrast to UV light.[63] For example, Titania (TiO_2) is the most extensively studied photocatalyst because of its high activity, nontoxicity, chemical inertness, low cost and no-photocorrosion.[64] However, the main disadvantage of titania is that it requires UV irradiation (~ 4% in solar spectrum) for effective photocatalysis, which limits its practical application.[65,66] It is extremely necessary to develop and design a photocatalyst which can use visible light (λ = 400-800 nm) efficiently under sun light irradiation. Many efforts have been carried out to develop new or modified semiconductor photocatalysts that are capable of using visible-light. Therefore, on the basis of various experiments performed in last few decades, a variety of common approaches have been adopted in order to synthesize efficient visible light driven photocatalysts for water splitting into hydrogen and/or oxygen as listed below:

1- Metal and nonmetal doping for tuning in the band gap (band gap engineering)
2- Developing solid solutions to control the band structure
3- Surface modification by co-catalyst deposition
4- Sensitization
5- Rational design of photocatalyst to control size, morphology and defects

1.6.1. Band Structure Engineering through Solid Solution

In addition to metal/nonmetal ion doping, solid solution of wide and small band gap semiconductor is also an important technique to control the band structure of photocatalyst. Solid solutions of two or more semiconductors can be formed if both the semiconductors have same lattice structure. The band gap and band position in the solid solution can be adjusted by altering the ratio of the compositions of the small and large band gap semiconductor. The band formation of photocatalyst by making solid solution is shown in Figure 1.6. Zhang *et al.* has demonstrated the sulfide solid solutions of $Cd_xZn_{1-x}S$, formed by combining large band gap semiconductor ZnS with small band gap semiconductor CdS which exhibits the highest hydrogen production with quantum yield of 10.23% without aid of any noble metal as cocatalyst.[67] Some other examples of solid solutions are GaN-ZnO,[68] $ZnS-AgInS_2$,[69] and CdS-CdSe.[70]

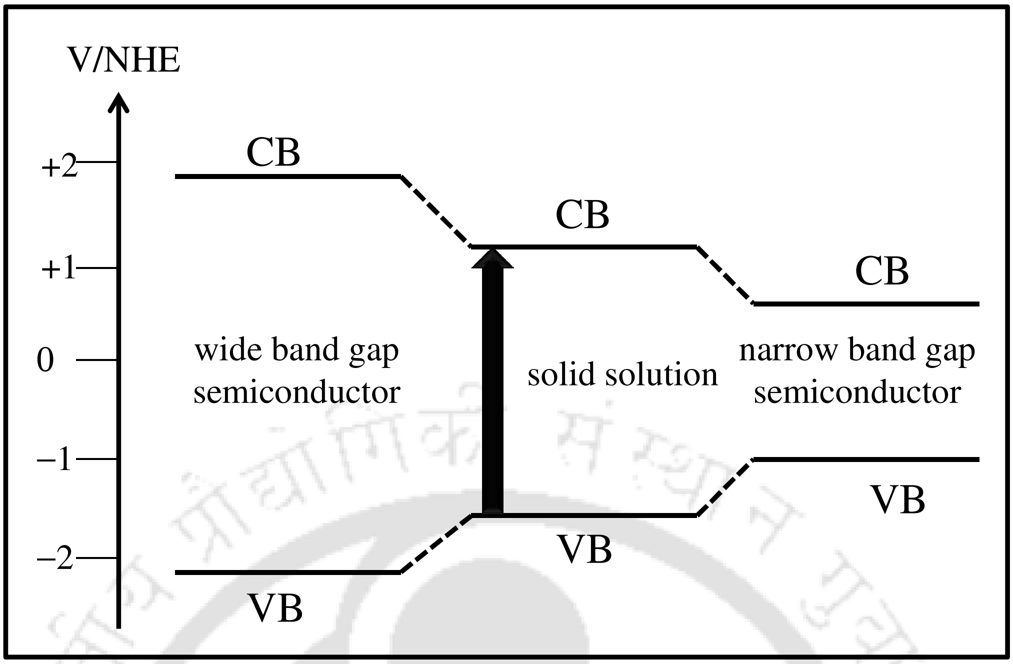

Figure 1.6 Schematic of band structure engineering by making solid solution of wide and narrow band gap semiconductor[33]

1.6.2. Surface Modification by Co-catalyst Deposition

The photocatalytic water splitting process is a surface process which involves the migration of photoinduced electrons and holes to the surface of photocatalyst followed by the redox reaction of water molecule (adsorbed onto the surface of photocatalyst). The photocatalytic efficiency of the catalyst can be further enhanced by the addition of noble metal such as Pt, Pd, Rh, NiO and RuO_2 etc. which are known as co-catalyst.[33] When the noble metal is deposited onto the photocatalyst surface, the photoinduced electrons migrate to the surface of photocatalyst and are trapped by the co-catalyst because the Fermi level of noble metal is lower than the photocatalyst, at the same time, the photoinduced holes migrate to the catalyst surface. This causes the efficient separation of photoinduced electrons and holes which improves the photocatalytic efficiency (Figure 1.7).

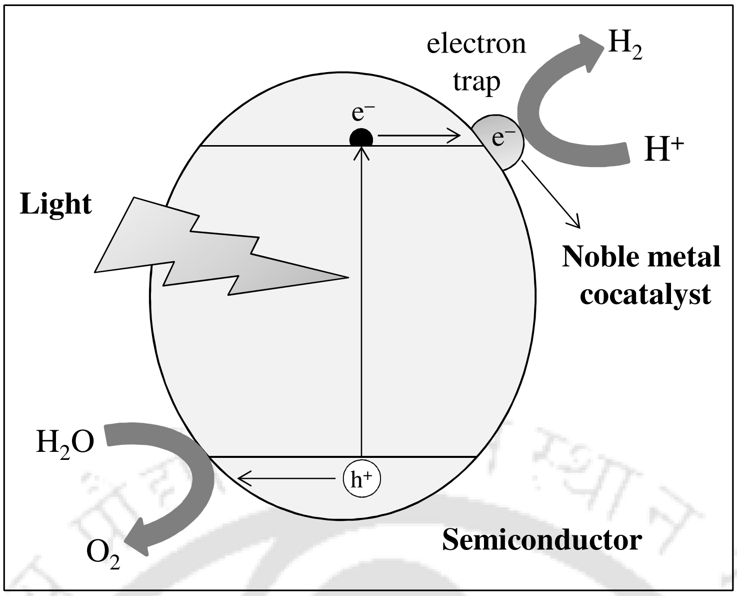

Figure 1.7 Schematic of the processes involved in the photocatalysis using cocatalyst[9]

1.6.3. Sensitization by Semiconductor Coupling

The sensitization technique which has been extensively studied is the coupling of low band gap semiconductor with wide band gap semiconductor having more negative CB level (i.e., hybrid or composite photocatalyst) with the formation of hetero-junction structure. For composite synthesis, the selection of semiconductor is based on its CB alignment with other the semiconductor, if the CB of both semiconductors are in the proximity which can facilitate efficient charge migration thereby, reducing the recombination rate of photoinduced electrons and holes pair (Figure 1.8), by making the photocatalytic process more efficient. Thus, sensitization by coupling of semiconductors is the most effective way to enhance the efficiency of photocatalytic process.

Cadmium sulfide, a visible light driven photocatalyst, has intrinsic photocorrosion property because of its self-oxidation by photogenerated oxidative holes in the VB which makes CdS unstable to light. Thus, in order to improve the stability and photocatalytic activity of CdS it has been coupled with the wide band gap semiconductors like CdSe,

TiO_2, ZnO, SrS and $LaMnO_3$ etc.[70-75] Among all these, CdS/TiO_2 is the most extensively studied coupled semiconductor due to the CB alignment of CdS and TiO_2. Under the visible light irradiation, the photoinduced electrons in the CB of CdS rapidly transfer to the CB of TiO_2 whereas the photoinduced hole stays in the VB of CdS. This facilitates the efficient electron hole pair separation causes improved photocatalytic activity. Some of the examples of semiconductor coupled materials for water splitting under visible light irradiation present in literature are listed in Table 1.2.

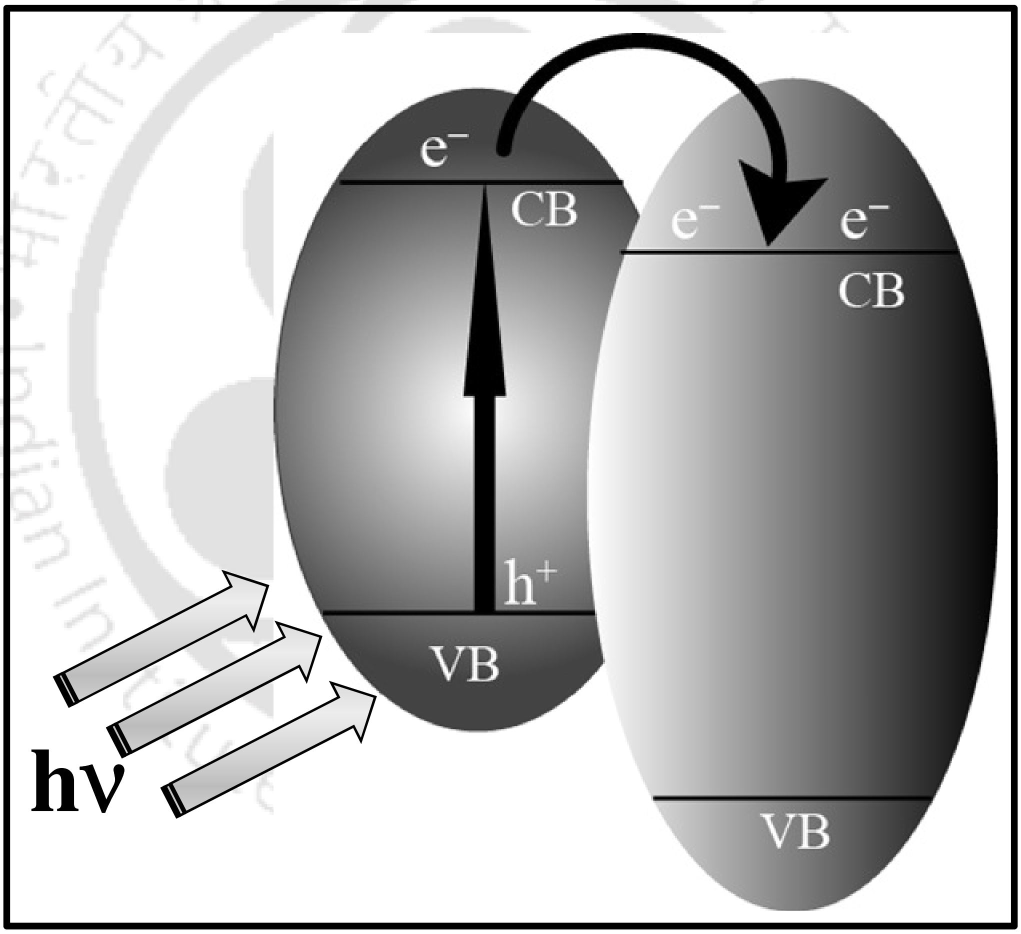

Figure 1.8 Schematic illustration of coupled semiconductors for efficient charge separation under visible light irradiation

Table 1.2 Coupled semiconductor visible light driven photocatalysts for water splitting

photocatalyst	**synthetic method**	**co-catal./H_2 evolution (µmol/h/g)**	**QY (%)**	**reference**
CdS/TiO_2	precipitation	Pt/6400	-	71
Bi_2S_3/TiO_2	hydrothermal	2900	-	76
CdS/ZnO	precipitation	Pt/3870	3.2	73
CdS/SrS	precipitation	Pt/123	5.83	74
$CdS/LaMnO_3$	reverse micelle	375	-	75
$CdS/KNbO_3$	precipitation	NiO_x/203.5	8.8	77

1.6.4. Rational Design of Photocatalyst to Control Size, Morphology and Defects

The water splitting reaction is carried out at the surface of semiconductor if the photogenerated charge carriers (electrons and holes) can reach to the bulk of catalyst without getting recombined. Therefore, for effective photocatalysis, the generation and maximum separation of these charge carriers is the fundamental condition to be fulfilled by the photocatalyst. The mobility of photoexcited charge carriers is determined by crystalline nature, particle size, structural defects and morphology of the photocatalyst semiconductor. A high degree of crystallinity (less defects) of the photocatalyst reduces the trapping center for charge carriers thereby leading efficient photocatalysis. The particle size is also an important factor which affects the photocatalytic efficiency. In case of nano-sized particle, the required distance that photoinduced charge carriers need to migrate to the surface of photocatalyst becomes short which results in the reduction of recombination rate (Figure 1.9).

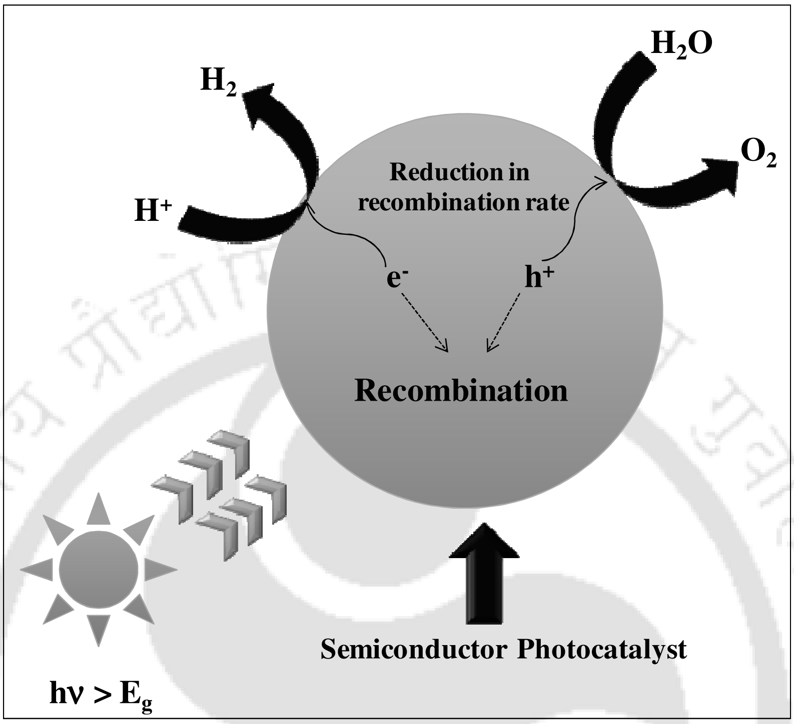

Figure 1.9 Schematic showing the effect of particle size on the photocatalytic activity

The morphology of the semiconductor material is also one of the critical factors which greatly affect the photocatalytic activity. Recently, much of the scientific work is devoted on hierarchical three dimensional (3D) nanomaterials due to their advantages on maximizing the specific surface area via creating porous spaces which results in the reduction of recombination rate of photoinduced electrons and holes thereby increasing the photocatalytic activity.[78-81] Wang *et al.* demonstrated the superior photocatalytic activity of colloidal TiO_2 catalysts when the particles have a tendency to form 3D networks.[82] Therefore, taking into account of these issues many efforts have been made for the rational design of materials having high crystallinity, small sized particle, high surface area and effective charge separation.

1.7. Photocatalysis for Dye Degradation

Recently, it was also found that several semiconductors has been extensively studied and widely used for environmental application such as water treatment and air purification.[83-86] Organic dyes are one of the numerous new chemicals which could be used in many industrial activities. Due to the extensive use of these dyes in industries, they become an essential part of industrial sewage. In fact, 450,000 ton of organic dyes were annually produced worldwide in which 11% are lost in sewages during manufacture and application processes.[87] Most of these dyes are noxious and carcinogenic in nature. Therefore, their removal from the industrial sewages is a major environmental problem.[88] Numerous methods have been used for the removal of organic dyes from water; these include the biodegradation, adsorption, coagulation, advanced oxidation process (AOP) and membrane process.[89-94] All these processes have some advantages and disadvantages over the other methods. However, among all these techniques, the advanced oxidation processes appear to be the most promising field for degradation of soluble organic contaminants from water and soil.[95] Several AOPs are well-known like photolysis (UV or UV-Vis), $H_2O_2/h\nu$, $O_3/h\nu$ and photocatalysis, among which photocatalysis fascinates much attention because it is inexpensive and converts organic contaminates to carbon dioxide and water. Photocatalytic water remediation is believed to take place by the following steps which are discussed below and shown in Figure 1.10:

1- Promotion of electrons from the VB to the CB leaving behind holes in the VB of photocatalyst upon the irradiation of light.

2- Migration of these reductive electrons and holes to the catalyst surface. Photoinduced holes oxidized water to hydroxyl radical (•OH) while electron can react with dissolved oxygen to produce superoxide radical anion ($O_2^{-\bullet}$).

3- Hydroxyl radical and superoxide radical anion react causes the discoloration of dye.

$$
\begin{aligned}
&\text{Catalyst} + h\nu \longrightarrow e^{-}_{cb} + h^{+}_{vb}\\
&O_2 + e^{-}_{cb} \longrightarrow O_2^{-\bullet}\\
&H_2O + h^{+}_{vb} \longrightarrow \bullet OH + H^{+}\\
&O_2^{-\bullet} + H_2O \longrightarrow H_2O_2\\
&H_2O_2 \longrightarrow 2\bullet OH\\
&\bullet OH + \text{dye} \longrightarrow CO_2 + H_2O
\end{aligned}
$$

Scheme 1.1 Primary steps involved in the degradation of a dye by semiconductor photocatalysis

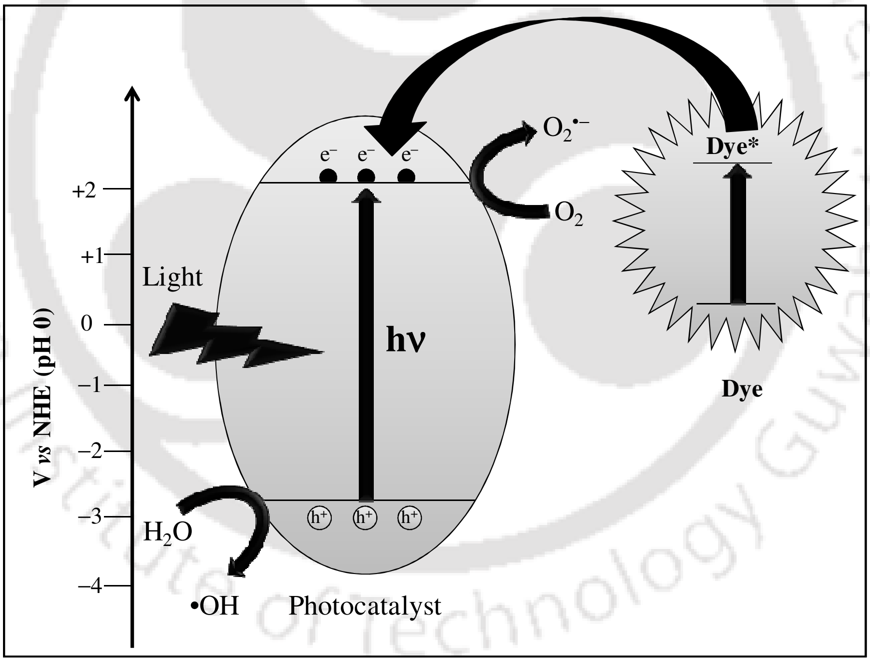

Figure 1.10 Schematic presentation of degradation of organic dye by semiconductor photocatalyst

For photocatalytic water remediation, VB holes are the important component for organic dye degradation. These positive holes can directly oxidize the organic dye but they readily react with water to form hydroxyl radical (•OH) which is a strong oxidizing agent with the oxidation potential of 2.8 V (NHE). Hydroxyl radical rapidly attacks the organic dye at the surface and as well as in solution and can decompose organic dye into CO_2, H_2O, etc. Therefore, in this regard, photocatalysis by semiconductor is regarded as one of the advanced oxidation treatments based on the generation of •OH radicals.

In conclusion, Cadmium Sulfide (CdS) is the most extensively used photocatalyst due to its suitable band gap (~2.4 eV) belongs to visible region and appropriate band positions. However, CdS has intrinsic photocorrosion property because of its self-oxidation by photogenerated holes in the valence band which makes CdS unstable to light (equation 8). Thus, in order to improve the stability and photocatalytic activity of CdS it has been embedded in different kind of matrices as well as coupled with wide band gap semiconductors like TiO_2, ZnO, SrS and $LaMnO_3$ *etc.*[96-99] Among all these, CdS/TiO_2 is the most extensively studied coupled semiconductor due to the CB alignment of CdS and TiO_2. Under the visible light irradiation, the photoinduced electrons in CdS rapidly transfer to CB of TiO_2 whereas the photoinduced hole stays in VB of CdS. This facilitates the efficient electron hole pair separation so improving the photocatalytic reactivity. However, in CdS/TiO_2 the possibility of recombination of photogenerated electron in CB of TiO_2 with the photogenerated holes in CdS VB makes it less efficient for photocatalytic processes. Therefore, it is necessary to develop a photocatalyst which can efficiently reduce the recombination rate of photoinduced electrons and holes by charge transfer. Along with facile charge transfer (by coupling with wide band gap semiconductor) the other factor which affects the photocatalytic activity of CdS is the low surface area. To improve photocatalytic efficiency different CdS based one dimensional (1D) semiconductor nanostructure materials such as nanorods, nanowires, nanotubes and nanobelts have fascinated the scientific community. Recently, the hierarchical 3D structured nanomaterials captivated the researchers worldwide because of its advantages on (i) maximizing the surface area for mass transfer and reactants access via creating porous spaces (ii) as well as reducing the recombination rate of photogenerated electrons and holes.

1.8. Motivation and objective of the present work

Among all the semiconductor materials, CdS is found to be the most active material for photocatalysis. However, the disadvantage of CdS is low photocatalytic efficiency and stability. Therefore, further improvements of CdS efficiency and stability are highly desirable. In this context, the enhancement of CdS efficiency and stability, by coupling CdS with the wide band gap semiconductor material and by maximizing the surface area of photocatalyst is the main focus of presented work. The following points are the outline of the objectives of the present work:

1- To rationally design CdS based photocatalyst having broad absorption range over entire UV and visible range

2- Utilizing the UV and visible light irradiation equivalent to solar energy for effective photocatalysis

3- To perform the hydrogen generation and dye degradation experiment and evaluate the photocatalytic activity of hybrid materials

4- To understand the mechanism for efficient hydrogen generation

5- To understand the organic dye degradation mechanism by the confirmation of reactive intermediates

References

1) Muradov, N. Z.; Veziroglu T. N. *Int. J. Hydrogen Energy* **2008**, *33*, 6804.

2) Nowotny, J.; Veziroglu, T. N. *Int. J. Hydrogen Energy* **2011**, *36*, 13218.

3) Hoffmann, M. R.; Martin, S. T.; Choi, W.; Bahnemann, D. W. *Chem. Rev.* **1995**, *95*, 69.

4) Bockris, J. O'M. *Int. J. Hydrogen Energy* **2002**, *27*, 731.

5) Yerga, R. M. N.; Galvan, M. C. Á.; del Valle, F.; Mano, J. A. V.; Fierro, J. L. G. *ChemSusChem*, **2009**, *2*, 471.

6) Armor, J. A.; *Appl. Catal. A* **1998**, *176*, 159.

7) Trimm, D. L.; Onsan, Z. I. *Catal. Rev. Sci. Eng.* **2001**, *43*, 31.

8) Navarro, R. M.; Pena, M. A.; Fierro, J. L. G. *Chem. Rev.* **2007**, *107*, 3952.

9) Kudo, A.; Miseki, Y. *Chem. Soc. Rev.* **2009**, *38*, 253.

10) R.-Nielsen, J. R.; Sehested, J. S.; Nrskov, J. K. *Adv. Catal.* **2002**, *47*, 65.

11) R.-Nielsen, J. R. in *Catalysis Science and Technology* (Eds.: J. R. Anderson, M. Boudart), Springer Verlag, Berlin, **1984**, Ch. 1.

12) Fujishima, A.; Honda, K. *Nature* **1972**, *238*, 37.

13) Mao, S. S.; Chen, X. *Int. J. Energy Res.* **2007**, *31*, 619.

14) Lehn, J. M.; Sauvage, J. P.; Ziessel, R.; *Nouv. J. Chim.* **1980**, *4*, 623.

15) Sato, S.; White, J. M. *Ind. Eng. Chem. Prod. Res. Dev.* **1980**, *19*, 542.

16) Domen, K.; Naito, S.; Suma, M.; Onishi, T.; Tamaura, K.; *J. Chem. Soc. Chem. Commun.* **1980**, 543.

17) Grätzel, M. *Energy Resources through Photochemistry and Catalysis*, Academic Press, New York, **1983**.

18) Serpone, N.; Pelizzetti, E. *Photocatalysis*, Wiley, New York, **1989**.

19) Yoneyama, H. *Crit. Rev. Solid State Mater. Sci.* **1993**, *18*, 69.

20) Domen, K.; Kondo, J. N.; Hara, M.; Takata, T. *Bull. Chem. Soc. Jpn.* **2000**, *73*, 1307.

21) Kudo, A. *J. Ceram. Soc. Jpn.* **2001**, *109*, 81.

22) Zou, Z.; Arakawa, H. *J. Photochem. Photobiol., A* **2003**, *158*, 145.

23) Yamashita, H.; Takeuchi, M.; Anpo, M. *Encyclopedia of Nanoscience and Nanotechnology*, American Scientific Publishers, California, **2004**, 10, p. 639.

24) Anpo, M.; Dohshi, S.; Kitano, M.; Hu, Y.; Takeuchi, M.; Matsuoka, M. *Annu. Rev. Mater. Res.* **2005**, *35*, 1.

25) Kudo, A. *Int. J. Hydrogen Energy* **2006**, *31*, 197.

26) Zhang, W.; Park, S. B.; Kim, E. *Photo/Electrochemistry and Photobiology in the Environment*, Energy and Fuel, **2006**, 295.

27) Maeda, K.; Teramura, K.; Saito, N.; Inoue, Y.; Kobayashi, H.; Domen, K. *Pure Appl. Chem.* **2006**, *78*, 2267.

28) Shanguan, W. *Sci. Technol. Adv. Mater.* **2007**, *8*, 76.

29) Osterloh, F. E. *Chem. Mater.* **2008**, *20*, 35.

30) Pleskov, Y. V.; Gurevich, Y. Y. in *Semiconductor Photoelectrochemistry*, ed. P. N. Bartlett, Plenum, New York, **1986**.

31) Kudo, A. *Pure Appl. Chem.* **2007**, *79*, 1917.

32) Maeda, K.; Domen, K. *J. Phys. Chem. C* **2007**, *111*, 7851.

33) Chen, X.; Shen, S.; Guo, L.; Mao, S. S. *Chem. Rev.* **2010**, *110*, 6503.

34) Pleskov, Y. V.; Gurevich, Y. Y. in *Semiconductor Photoelectrochemistry*, ed. P. N. Bartlett, Plenum, New York, **1986**.

35) Yoshimura, J.; Ebina, Y.; Kondo, J.; Domen, K.; Tanaka, A. *J. Phys. Chem.* **1993**, *97*, 1970.

36) Kudo, A.; Omori, K.; Kato, H. *J. Am. Chem. Soc.* **1999**, *121*, 11459.

37) Kato, H.; Asakura, K.; Kudo, A. *J. Am. Chem. Soc.* **2003**, *125*, 3082.

38) Kim, H. G.; Hwang, D. W.; Lee, J. S. *J. Am. Chem. Soc.* **2004**, *126*, 8912.

39) Yamaguti, K.; Sato, S. *J. Chem. Soc., Faraday Trans. I* **1985**, *81*, 1237.

40) Kudo, A.; Domen, K.; Maruya, K.; Onishi, T. *Chem. Phys. Lett.* **1987**, *133*, 517.

41) Tabata, S.; Nishida, H.; Masaki, Y.; Tabata, K. *Catal. Lett.* **1995**, *34*, 245.

42) Shi, J.; Chen, J.; Feng, Z.; Chen, T.; Lian, Y.; Wang, X.; Li, C. *J. Phys. Chem. C* **2007**, *111*, 693.

43) Duonghong, D.; Borgarello, E.; Grätzel, M. *J. Am. Chem. Soc.* **1981**, *103*, 4685.

44) Jitputti, J.; Pavasupree, S.; Suzuki, Y.; Yoshikawa, S. *Jpn. J. Appl. Phys.* **2008**, *47*, 751.

45) Sasikala, R.; Shirole, A.; Sudarsan, V.; Sakuntala, T.; Sudakar, C.; Naik, R.; Bharadwaj, S. R. *Int. J. Hydrogen Energy* **2009**, *34*, 3621.

46) Zielinska, B.; Borowiak-Palen, E.; Kalenczuk, R. J. *Int. J. Hydrogen Energy* **2008**, *33*, 1797.

47) Mizoguchi, H.; Ueda, K.; Orita, M.; Moon, S. C.; Kajihara, K.; Hirano, M.; Hosono, H. *Mater. Res. Bull.* **2002**, *37*, 2401.

48) Zou, J. J.; Liu, C. J.; Zhang, Y. P. *Langmuir* **2006**, *22*, 2334.

49) Liu, S. H.; Wang, H. P. *Int. J. Hydrogen Energy* **2002**, *27*, 859.

50) Yuan, Y.; Zhang, X.; Liu, L.; Jiang, X.; Lv, J.; Li, Z.; Zou, Z. *Int. J. Hydrogen Energy* **2008**, *33*, 5941.

51) Yuan, Y. P.; Zhao, Z. Y.; Zheng, J.; Yang, M.; Qiu, L. G.; Li, Z. S.; Zou, Z. G. *J. Mater. Chem.* **2010**, *20*, 6772.

52) Li, G.; Kako, T.; Wang, D.; Zou, Z.; Ye, J. *J. Phys. Chem. Solids* **2008**, *69*, 2487.

53) Ding, Q. P.; Yuan, Y. P.; Xiong, X.; Li, R. P.; Huang, H. B.; Li, Z. S.; Yu, T.; Zou, Z. G.; Yang, S. G. *J. Phys. Chem. C* **2008**, *112*, 18846.

54) Kudo, A.; Kato, H.; Nakagawa, S. *J. Phys. Chem. B* **2000**, *104*, 571.

55) Sayama, K.; Arakawa, H. *J. Photochem. Photobiol., A* **1994**, *77*, 243.

56) Kato, H.; Kudo, A. *J. Phys. Chem. B* **2001**, *105*, 4285.

57) Kato, H.; Kudo, A. *Catal. Today* **2003**, *78*, 561.

58) Chen, D.; Ye, J. *Chem. Mater.* **2007**, *19*, 4585.

59) Sakata, Y.; Matsuda, Y.; Yanagida, T.; Hirata, K.; Imamura, H.; Teramura, K. *Catal. Lett.* **2008**, *125*, 22.

60) Maeda, K.; Teramura, K.; Saito, N.; Inoue, Y.; Domen, K. *Bull. Chem. Soc. Jpn.* **2007**, *80*, 1004.

61) Reber, J. F.; Meier, K. *J. Phys. Chem.* **1984**, *88*, 5903.

62) Ohmori, T.; Mametsuka, H.; Suzuki, E. *Int. J. Hydrogen Energy* **2000**, *25*, 953.

63) Li, Shi-K.; Huang, Fang-Z.; Wang, Y.; Shen, Yu-H.; Qiu, Ling-G.; Xie, An-J.; Xu, Shou-J. *J. Mater. Chem.* **2011**, *21*, 7459.

64) Bian, Z.; Zhu, J.; Wang, S.; Cao, Y.; Qian, X.; Li, H. *J. Phys. Chem. C* **2008**, *112*, 6258.

65) Yang, H. G.; Sun, C. H.; Qaio, S. Z.; Zou, J.; Liu, G.; Smith, S. C.; Cheng, H. M.; Lu, G. Q. *Nature* **2008**, *453*, 638.

66) Yang, H. G.; Liu, G.; Qiao, S. Z.; Sun, C. H.; Jin, Y. G.; Smith, S. C.; Zou, J.; Cheng, H. M.; Lu, G. Q. *J. Am. Chem. Soc.* **2009**, *131*, 4078.

67) Zhang, K.; Jing, D.; Xing, C.; Guo, L. J. *Int. J. Hydrogen Energy* **2007**, *32*, 4685.

68) Matsumura, M.; Saho, Y.; Tsubomura, H. *J. Phys. Chem.* **1983**, *87*, 3807.

69) Inoue, Y.; Asai, Y.; Sato, K. *J. Chem. Soc. Faraday Trans.* **1994**, *90*, 797.

70) Kambe, S.; Fujii, M.; Kawai, T.; Kawai, S. *Chem. Phys. Lett.* **1984**, *109*, 105.

71) Jang, J. S.; Kim, H. G.; Joshi, U. A.; Jang, J. W.; Lee, J. S. *Int. J. Hydrogen Energy* **2008**, *33*, 5975.

72) Jang, J. S.; Li, W.; Oh, S. H.; Lee, J. S. *Chem. Phys. Lett.* **2006**, *425*, 278.

73) Wang, X.; Liu, G.; Chen, Z.; Li, F.; Wang, L.; Lu, G.; Cheng, H. *Chem. Commun.* **2009**, *23*, 3452.

74) Liu, H.; Zhang, K.; Jing, D.; Liu, G.; Guo, L. *Int. J. of Hydrogen Energy* **2010**, *35*, 7080.

75) Kida, T.; Guan, G.; Yoshida, A. *Chem. Phys. Lett.* **2003**, *371*, 563.

76) Brahimi, R.; Bessekhouad, Y.; Bouguelia, A.; Trari, M. *Catal. Today* **2007**, *122*, 62.

77) Choi, J.; Ryu, S. Y.; Balcerski, W.; Lee, T. K.; Hoffmann, M. R. *J. Mater. Chem.* **2008**, *18*, 2371.

78) Bai, H.; Liu, Z.; Sun, D. D. *Chem. Commu.* **2010**, *46*, 6542.

79) Zhao, Y.; Zhang, X.; Zhai, J.; He, J.; Jiang, L.; Liu, Z. *Appl. Catal. B:Environ.* **2008**, *83*, 24.

80) Fonzo, F. D.; Casari, C. S.; Russo, V.; Brunella, M. F.; Bassi, A. L.; Bottani, C. E. *Nanotechnology* **2009**, *20*, 1.

81) Zhao, T.; Liu, Z.; Nakata, K.; Nishimoto, S.; Murakami, T.; Zhao, Y. *J. Mater. Chem.* **2010**, *20*, 5095.

82) Wang, C. Y.; Bättcher, C.; Bahnemann, D. W.; Dohrmann, J. K. *J. Mater. Chem.* **2003**, *13*, 2322.

83) Lia, Y.; Du, J.; Peng, S.; Xie, D.; Lu, G.; Li, S. *Int. J. Hydrogen Energy* **2008**, *33*, 2007.

84) Guo, Y.; Wang, J.; Yang, L.; Zhang, J.; Jiang, K.; Li, W.; Wang, L.; Jiang, L. *CrystEngComm* **2011**, *13*, 5045.

85) Wang, Z.; Pan, L.; Wang, L.; Wang, H. *Solid State Sciences* **2011**, *13*, 970.

86) Silva, L. A.; Ryu, S. Y.; Choi, J.; Choi, W.; Hoffmann, M. R. *J. Phys. Chem. C* **2008**, *112*, 12069.

87) Forgas, E.; Cserhati, T.; Oros, G. *Environmental International* **2004**, *30*, 953.

88) Parsons, S. in *Advanced Oxidation Processes for Water and Wastewater Treatment*, IWA Publishing, **2004**.

89) Derudi, M.; Venturini, G.; Lombardi, G.; Nano, G.; Rota, R. *European Journal of Soil Biology* **2007**, *43*, 297.

90) Martin, M.J.; Artola, A.; Balaguer, M.D.; Rigola, M. *Chemical Engineering Journal* **2003**, *94*, 231.

91) Ahmad, A. L.; Puasa, S.W. *Chemical Engineering Journal* **2007**, *132*, 257.

92) Arslan, I.; Balcioglu, I. A.; Bahnemann, D. W. *Dyes and Pigments* **2000**, *47*, 207.

93) Mo, J. H.; Lee, Y. H.; Kim, J.; Jeong, J. Y.; Jegal, J. *Dyes and Pigments* **2008**, *76*, 429.

94) Rauf, M. A.; Ashraf, S. S.; Alhadrami, S. N. *Dyes and Pigments* **2005**, *66*, 197.

95) Perez, M. H.; Penuela, G.; Maldonado, M. I.; Malato, O.; Ibanez, P. F.; Oller, I.; Gernjak, W.; Malato, S. *Appl. Catal. B: Environ.* **2006**, *64*, 272.

96) Ke, D.; Liu, S.; Dai, K.; Zhou, J.; Zhang, L.; Peng, T. *J. Phys. Chem. C* **2009**, *113*, 16021.

97) Wang, X.; Liu, G.; Chen, Z.; Li, F.; Wang, L.; Lu, G.; Cheng, H. *Chem. Commun.* **2009**, *23*, 3452.

98) Liu, H.; Zhang, K.; Jing, D.; Liu, G.; Guo, L. *Int. J. of Hydrogen Energy* **2010**, *35*, 7080.

99) Kida, T.; Guan, G.; Yoshida, A. *Chem. Phys. Lett.* **2003**, *371*, 563.

Chapter 2

Experimental Section

This chapter describes the details of the synthesis of CdS based hybrid photocatalysts and their characterization. Special interest is given to the description of in-house built photocatalytic measurement set-up along with the gas chromatographic (GC) instrumentation. This chapter also demonstrates the detailed experimental procedure for hydrogen generation and organic dye degradation. We have explained the method for the calculation of apparent quantum yield for hydrogen generation. A brief description of the freeze-thaw cycle preformed for the mechanistic (for the presence of intermediate, such as superoxide radical) study of dye degradation is also discussed.

2.1. Introduction

Cadmium Sulfide (CdS) is one of the most studied photocatalyst for hydrogen generation and organic dye degradation since last few decades due to its favorable band gap and band alignment. The photocatalytic efficiency of CdS is low due to the high recombination rate of photoinduced charge carriers. Therefore, in order to enhance the photocatalytic efficiency various CdS based hybrid semiconductor photocatalysts were synthesized. Syntheses of various novel CdS/Metal Chalcogenides based hybrids were described in this chapter using hydrothermal route, which offers products with good crystallinity and good yield.

2.2. Chemicals Details

Cadmium acetate dihydrate, Aluminum nitrate nonahydrate, Zinc chloride, Nickel chloride hexahydrate, Strontium chloride hexahydrate, Sodium sulfide, Thioglycolic acid, aq. Ammonia (25%), Sodium nitrate, Hydrogen peroxide (50%) and Potassium permanganate were purchased from Merck while graphite was purchased from Loba Chemie, India and all chemicals were used as received without any further purification.

2.3. Synthesis

2.3.1. Synthesis of CdS Nanowires (NWs)

One dimensional (1D) CdS NWs were synthesized via one step hydrothermal route reported by Maleki *et al.*[1] In brief, 1 gm. of $Cd(OOCCH_3)_2.2H_2O$ was dissolved in 25 mL of ethylenediamine. The solution was stirred at room temperature. Finally, stoichiometric amount of sulfur powder was added under the vigorous stirring which resulted in the formation of turbid solution. The solution was then transferred to a Teflon-lined stainless steel autoclave and maintained at 140 °C for 7 h. After cooling down to room temperature, the obtained reaction mixture was centrifuged and the pellet obtained was washed with water and ethanol. Finally, the product was dried in an oven at 70 °C for 4-5 h.

2.3.2. Synthesis of CdS Nanoparticles (NPs)

A typical procedure for the CdS nanoparticles (NPs) synthesis; 0.5 g of $Cd(OOCCH_3)_2.2H_2O$ was dissolved in 25 mL of ethylenediamine in a flask at room temperature. A milk-white sol was formed which was heated to 100 °C, followed by the addition of pure Na_2S under vigorous stirring and kept on stirring at this temperature for about 6 hours until the milk white reaction mixture gradually turned to a yellow color. The final product was then collected, washed with distilled water and ethanol and dried in vacuum.

2.3.3. Synthesis of ZnO NPs

ZnO NPs were synthesized by the method reported by Becheri *et al.*[2] $ZnCl_2$ (5.5 g, 40 mmol) was dissolved in 200 mL water at 90 °C, followed by the addition of 16 mL of 5 M NaOH solution drop wise with gentle stirring for 10 min. ZnO NPs were formed and separated from the supernatant dispersion by the sedimentation method (the supernatant solution was discarded) and the suspension was washed with water to remove excess metal ion on or salts. The particles were treated ultrasonically in 2-propanol for 10 min, collected by centrifugation, and finally maintained at 250 °C for 5 h in a Teflon-lined stainless steel autoclave to obtain the ZnO nanoparticles.

2.3.4. Synthesis of SrS NPs

SrS nanoparticles were synthesized by modified precipitation method.[3] $SrCl_2.6H_2O$ (1 g) was dissolved in 50 mL distilled water followed by the drop wise addition of excess amount of Na_2S solution (~4-fold) under vigorous stirring in presence of thioglycolic acid. The reaction mixture was then stirred at room temperature for 24 h and the resulting white precipitate was filtered and washed with water-ethanol mixture. The product was dried at 70 °C for 12 h in an electronic oven.

2.3.5. Synthesis of Graphene Oxide (GO)

Graphene oxide was prepared through oxidation of graphite as reported by Hummers *et al.*[4] Graphite powder (0.5 g) and $NaNO_3$ (0.5g) were mixed in 30 mL of H_2SO_4 (95%) at temperature (0-5 °C). The reaction mixture was stirred for 30 min at this temperature followed by the slow addition of $KMnO_4$ (1.5g) to the suspension. The addition rate of $KMnO_4$ was controlled cautiously to keep the reaction temperature lower than 15 °C. There after ice bath was removed, and reaction mixture was stirred at 35 °C for 7 h until it became pasty brownish and then diluted with 50 ml of water. The reaction temperature was rapidly increased to 98 °C, stirred it for 6 h, and then color changed to brown color. Further this solution was diluted by adding 50 ml water and finally treated with 1 ml H_2O_2 (30 wt %) to remove excess $KMnO_4$, if any. For purification, the mixture was washed by rinsing and centrifugation with 10% HCl and then deionized (DI) water several times. After filtration and drying under vacuum at room temperature, GO was obtained as a powder which on ultrasonic treatment yields GO nano-sheet.

2.3.6. General Scheme for Hierarchical 3D CdS/Metal Chalcogenides Heteroarrays Synthesis

Hierarchical 3D CdS/Metal Chalcogenides binary heteroarrays were synthesized by hydrothermal route. In a typical synthesis, metal salts (3.9 mmol) was dissolved in 15 mL distilled water followed by the addition of aqueous NH_3 (to maintain pH 7) under vigorous stirring. After the addition of $Cd(OOCCH_3)_2.2H_2O$ (9.0 mmol) and thioglycolic acid (9.0 mmol), reaction mixture was stirred at room temperature for 30 min. The resultant suspension was transferred to a Teflon-lined stainless steel autoclave, in an electronic oven at 140 °C. After cooling down to room temperature, the solution obtained was centrifuged and the solid product was washed with water and ethanol to remove excess metal ions and thioglycolic acid, if any. After being dried at 70 °C for 5 h in an oven under atmospheric condition, the samples were ready for further characterizations and photocatalytic activity test. The optimized temperature and metal ion ratio for the synthesis of different 3D CdS based binary heteroarrays are listed below in Table 2.1.

Table 2.1 Optimized reaction condition for the synthesis of hierarchical 3D CdS/Metal Chalcogenides binary heteroarrays

Metal Ions	**Reaction Condition**	**Approximate Metal Ion Ratios**
Cd^{2+}/Al^{3+}	140 °C, pH 7, 48 h	1:0.42
Cd^{2+}/Zn^{2+}	140 °C, pH 7, 48 h	1:0.42
Cd^{2+}/Ni^{2+}	140 °C, pH 7, 24 h	1:0.42
Cd^{2+}/Sr^{2+}	140 °C, pH 7, 24 h	1:0.42

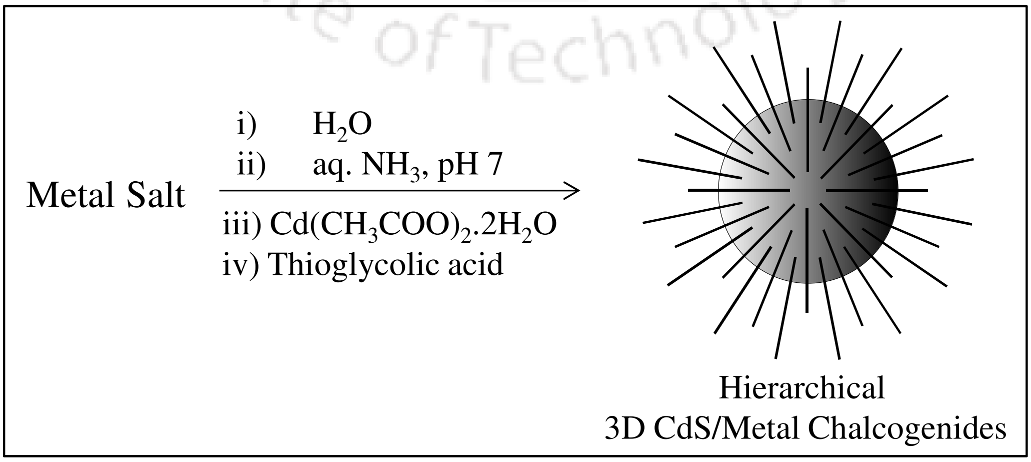

2.3.7. Synthesis of CdS/Metal Oxide/GO Photocatalyst

CdS/Metal Oxide/GO was synthesized by solid state route. Briefly, 0.2 g of as prepared CdS/Metal Oxide was thoroughly ground with 1 wt% of as prepared GO by using mortar pestle for 30 min. The rationale behind the grounding of CdS/Metal Oxide and GO is to make uniform contact between them. The obtained powder of CdS/Metal Oxide/GO was used for to examine the effect of graphene oxide on photocatalytic hydrogen generation and for dye degradation.

2.3.8. Photocatalytic Water Splitting Experiment

In order to evaluate the photocatalytic efficiency of the samples, photocatalytic hydrogen production experiments were performed separately in 100 mL double walled quartz round-bottom flask having water inlet and outlet to maintain the temperature of the photoreactor. The photocatalytic reaction was carried out at atmospheric conditions. It is well known that CdS has intrinsic photocorrosion property, therefore, to avoid the photocorrosion reaction the whole experiment was performed under N_2 atmosphere in presence of sacrificial reagents. A 500-W Phoenix tungsten halogen lamp (or 300 W Xenon arc lamp) was used as a light source to initiate the photocatalytic reaction. In a typical photocatalytic experiment, 0.2 g of sample was dispersed in 50 mL water containing Na_2SO_3 (0.25 mol/L) and Na_2S (0.35 mol/L) as a sacrificial reagent. The solution containing photocatalyst was degassed for 30 min and irradiated with visible light accompanying proper stirring to ensure uniform exposure of suspension throughout the process. The produced gas was analyzed by gas chromatography (Varian CP 3800 GC, Carbosieve S II column), using thermal conductivity detector (TCD), after passing through moisture and oxygen traps. A schematic presentation of the photochemical reactor setup is shown in Figure 2.1. In the absence of either light or the photocatalyst, no hydrogen was detected, suggesting the role of photocatalysts in hydrogen production. The apparent quantum yield (AQY) of the photocatalyst was measured under the same reaction condition and was calculated using the following equation and method discussed below:

$$\mathrm{AQY} = \frac{\text{Number of reacted electrons}}{\text{Number of incident photons}} \times 100\ \%$$
$$= \frac{2 \times \text{Number of } \mathrm{H_2} \text{ molecules evolved in 1 hour}}{\text{Number of incident photons in 1 hour}} \times 100\ \%$$

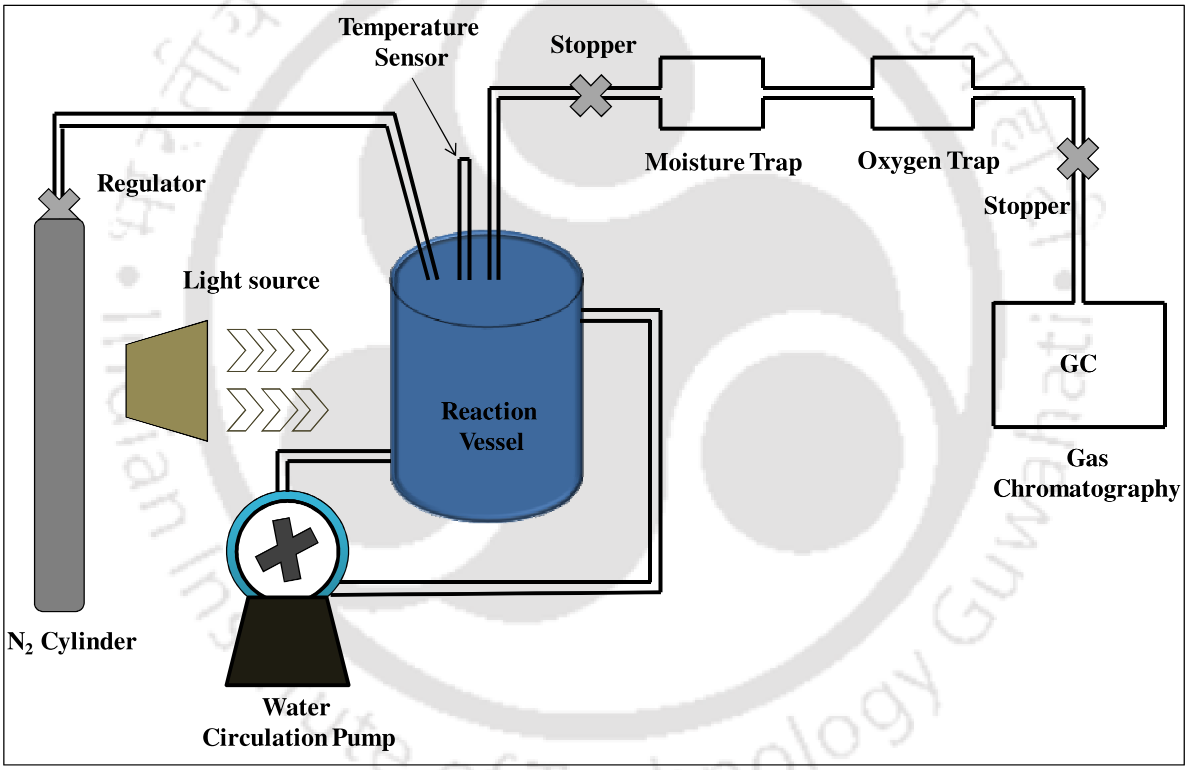

Figure 2.1 Schematic of the experimental set-up for photocatalytic hydrogen generation by water splitting

2.3.9. Quantum Efficiency Calculation

The AQY is calculated following the method reported by Sasikala *et al.*[5] The total light intensity incident at the sample position is measured by using Lutron LX101 lux meter; the lux meter is placed at the center where the reactor is placed for irradiation.

Assuming uniform intensity distribution of the lamp, a correction for the difference in the area of the sensor of lux meter and the reactor surface area is evaluated. The UV–Vis diffused reflectance absorption spectra of the all photocatalysts show the absorption steeps in the wavelength range of 250–600 nm. Therefore, the fraction of light intensity only in this wavelength region (vary with different samples) is considered for quantum efficiency calculation. The emission profile of the lamp gives the incident light intensity in the range of 250–600 nm. The energy of a single photon of the polychromatic light source is considered as the weighted average energy (E_a) of all the photons in 250–600 nm wavelength range. Now, the contribution of photon of each wavelength λ_i towards the total energy can be calculated as

$$E_i = \frac{I_{\lambda i}}{I_{total}} \times \frac{hc}{\lambda_i},$$

where $I_{\lambda i}$ is the intensity at wavelength λ_i and I_{total} is obtained from the lamp emission profile by adding the intensities of all photons in the wavelength range of 250–600 nm. The weighted average energy of single photon (E_a) is calculated as

$$E_a = \sum_{\lambda_i=250}^{600} E_i(\lambda_i)$$

Total number of incident photons in 250–600 nm range (N) is given by

$$N = \frac{E_m}{E_a},$$

where the factor E_m is calculated by multiplying the total incident intensity with the ratio of the area in 250–600 nm range to the total area of the emission profile.

2.3.10. Photocatalytic Dye Degradation Experiment

Photocatalytic degradation experiments for various photocatalyst were performed separately in 100 mL double walled quartz round-bottom flask (schematic of experimental setup for dye degradation is shown in Figure 2.2 and Figure 2.3). In a typical photocatalytic degradation experiment, 50 mL of aqueous methyl orange (concentration = 1×10^{-5} M) and 0.2 g photocatalyst samples were loaded into a quartz photoreactor. Prior to irradiation, reaction mixture was stirred for an hour in dark at room temperature to maintain adsorption/desorption equilibrium among the photocatalyst, dye, solubilized oxygen and atmospheric oxygen. During the degradation process, 500-W Phoenix tungsten halogen lamp (or 300 W Xenon arc lamp) was placed horizontally 30 cm above the photoreactor. The suspension was stirred during the irradiation to make the solution homogenous. 3 mL of samples were collected every 3 or 5 minutes from the photoreactor and absorption measurements were performed within 200-800 nm after removing the solid catalyst particles by centrifugation. The concentration of the aqueous methyl orange was determined from the absorbance value at 464 nm.

Degradation of methyl orange is not observed in the absence of either photocatalyst or light. Detailed mechanistic study for the presence of reactive intermediate involved in MO degradation, dye degradation experiments were also performed with deoxygenated water. Deoxygenated water was prepared by performing four cycles of freeze-thaw cycle (Figure 2.4).

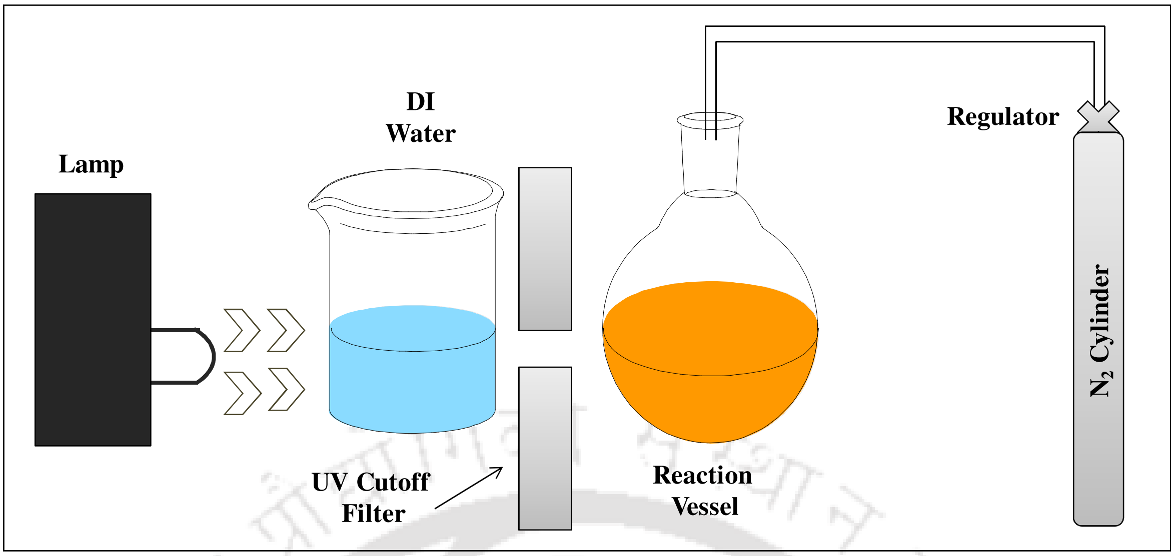

Figure 2.2 Schematic of the experimental set-up for the photocatalytic dye degradation

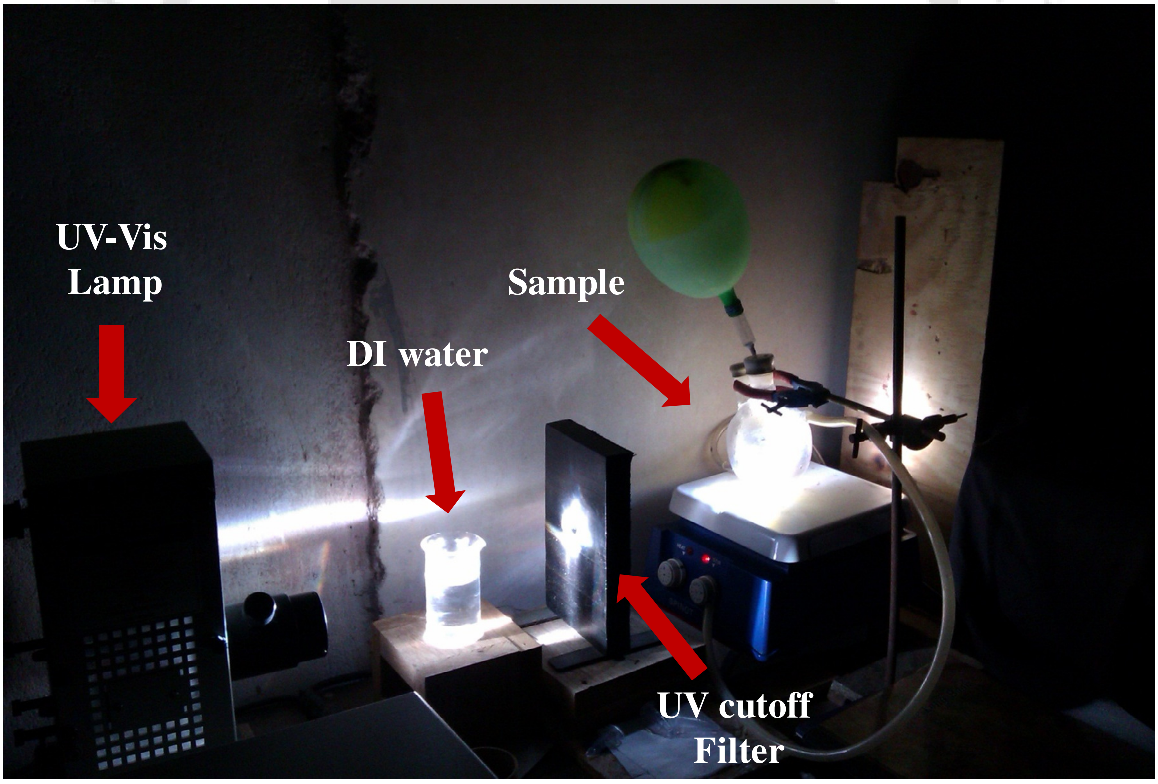

Figure 2.3 Experimental setup used for the degradation of organic dye

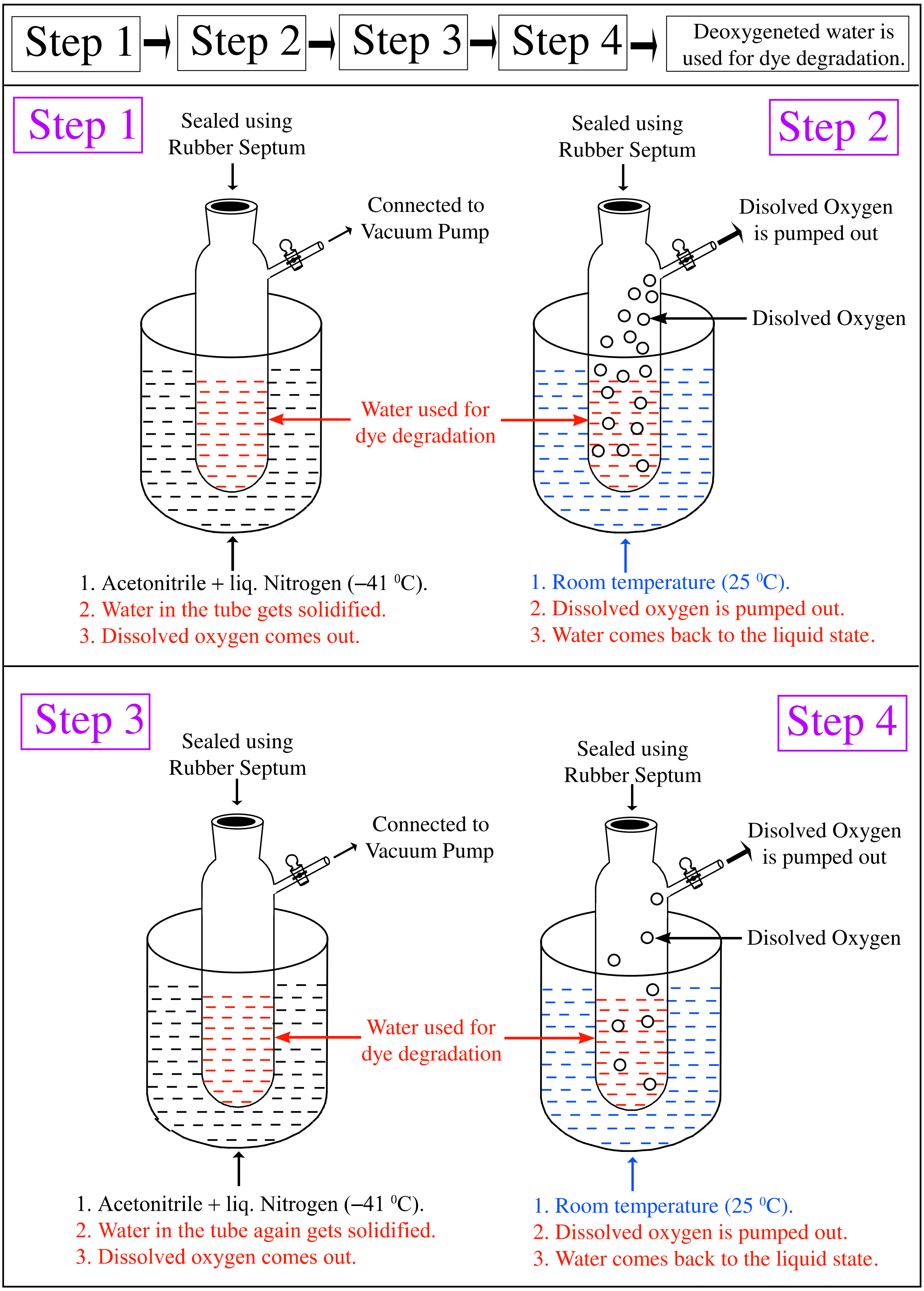

Figure 2.4 Schematic illustrations for the preparation of deoxygenated water by freeze thaw cycle

2.4. Characterization

The compounds synthesized were characterized employing various techniques. The instrumental techniques employed in the present investigations include:

1. Powder X-ray diffraction **(XRD)** with Brucker D8 X- ray diffractometer Cu Kα radiation (λ = 0.154 nm) source
2. Scanning Electron Microscope **(SEM)**, Leo 1430vp
3. Field Emission Scanning Electron Microscopy **(FE-SEM)**, Zeiss Sigma
4. 200 kV Transmission Electron Microscope **(TEM)**, JEOL JEM 2100
5. Energy-dispersive X-ray **(EDX)** spectroscopic analysis INCA, Oxford instruments
6. UV-Visible diffuse reflectance spectra **(DRS)** (Jasco V-650 spectrophotometer) with integrating sphere of 150 mm
7. N_2 adsorption desorption isotherm (BECKMAN-COULTER SA 3100)
8. Gas Chromatography (Varian CP 3800 GC)

2.4.1. Gas Chromatography

Gas chromatography (GC) is a chromatography technique used in analytic chemistry for separating and analyzing compounds that can be vaporized without decomposition. In GC, the mobile phase is a carrier gas, usually an inert gas such as helium or nitrogen. The stationary phase is a microscopic layer of liquid or polymer on an inert solid support, inside a piece of glass or metal tubing called a column. Varian CP 3800 GC is equipped with Carbosieve S II column and thermal conductivity detector (TCD). Carbosieve S II column is mainly used for analyzing the mixtures of gases (hydrogen, oxygen, nitrogen, carbon monoxide etc.) and C1-C2 hydrocarbons (methane, ethane, ethylene, and acetylene). Thermal conductivity detector senses change in the thermal conductivity of the column effluent and compares it to a reference flow of carrier gas. The schematic of gas chromatography is shown in Figure 2.5.

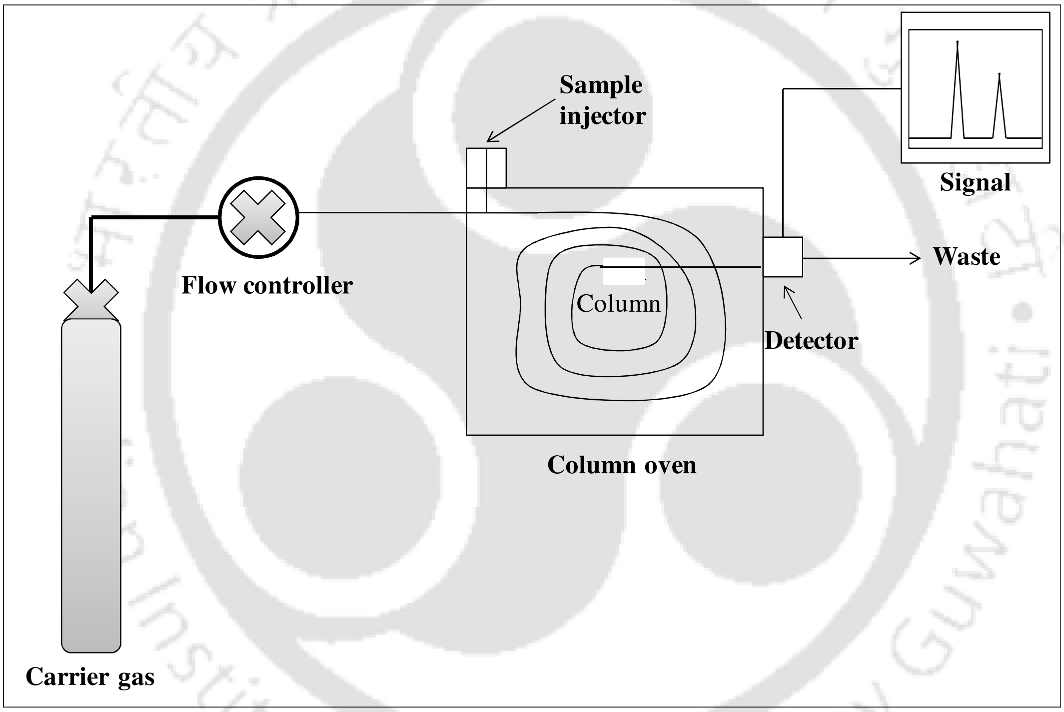

Figure 2.5 Schematic presentation of the gas chromatography[6]

References

1) Maleki, M.; Mirdamadi, Sh.; Ghasemzadeh, R.; Ghamsari, M. S. *Mater. Lett.* **2008**, *62*, 1993.

2) Becheri, A.; Dürr, M.; Nostro, P. L.; Baglioni, P. *J. Nanopart. Res.* **2008**, *10*, 679.

3) Liu, H.; Zhang, K.; Jing, D.; Liu, G.; Guo, L. *Int. J. of Hydrogen Energy* **2010**, *35*, 7080.

4) Hummers, W.; Offeman, R. *J. Am. Chem. Soc.* **1958**, *80*, 1339.

5) Sasikala, R.; Sudarsan. V.; Sudakar, C.; Naik, R.; Sakuntala, T.; Bharadwaj, S. R. *Int. J. Hydrogen Energy* **2008,** *33*, 4966.

6) http://en.wikipedia.org/wiki/Gas_chromatography

Chapter 3

Part A

Synthesis, Characterization and Evaluation of Photocatalytic Activities of Hierarchically Grown Urchin-like 3D CdS/ZnO and 3D CdS/Al_2O_3 Heteroarrays

This chapter describes simple single pot hydrothermal synthesis of hierarchical 3D CdS/ZnO and 3D CdS/Al_2O_3 heteroarrays confirmed by SEM and TEM. Hierarchical 3D CdS/ZnO and 3D CdS/Al_2O_3 heteroarrays exhibit excellent photocatalytic water splitting and efficient photodegradation of organic dye; Methyl Orange. The high photocatalytic activity of 3D CdS/Al_2O_3 is attributed to the enhanced surface area while for 3D CdS/ZnO; high activity is ascribed due to superior surface area and efficient charge separation.

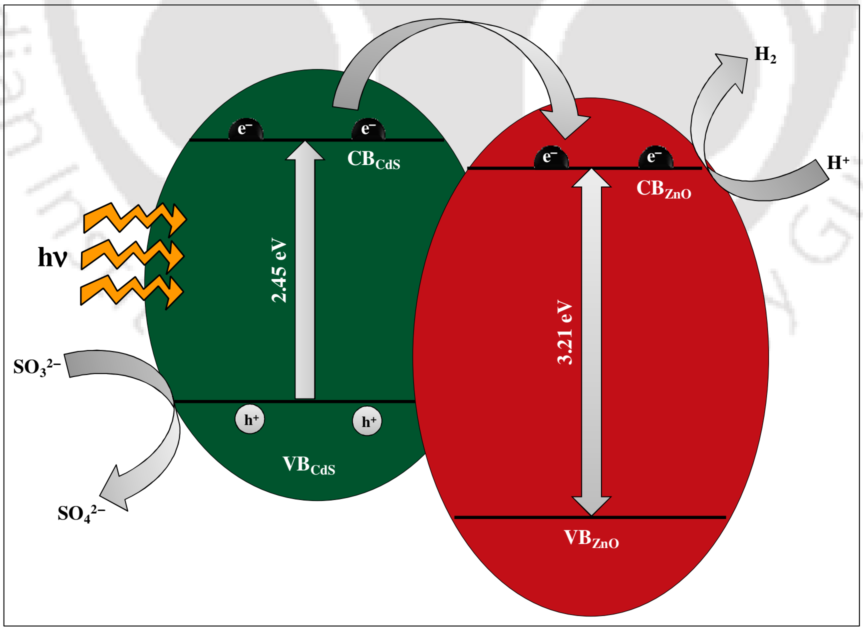

Mater. Lett. **2011**, *65*, 1168

J. Phys. Chem. C **2012**, *116*, 150

3A.1. Introduction

Cadmium Sulfide (CdS) is the most extensively studied semiconductor photocatalyst for the solar energy conversion to chemical energy and the degradation of organic dyes under visible light irradiation. CdS has a conduction band edge suitably more negative than the reduction potential of hydrogen and relatively narrow band gap which can efficiently absorb visible light.[1,2] However, it was found that due to the several issues the photocatalytic activity of CdS is low. For example, CdS has the tendency to form larger particles by aggregation which results the reduction in surface area and an increment in the recombination rate of photoinduced charge carriers.[3] However, researchers are exploring many photocatalytic systems in order to improve the photocatalytic efficiency of CdS, such as preparation of quantum dots,[4] nanoparticles (NPs)[5], nanorods,[6] nanowires (NWs),[7] nanotubes,[8] deposition of noble metals,[9] preparation of heterogeneous semiconductors,[10,11] and incorporation of semiconductor particles in the interlayer region of layered compounds.[12] It is found that the photocatalytic efficiency of CdS can be enhanced by coupling CdS to a suitable wide-band gap metal oxide semiconductor (ZnO, TiO_2) such that the charge transfer can occur from the CB of CdS to that of the metal oxide so that effective charge separation can be attained.[13,14] The present work demonstrates the efficient photocatalysis by the use of three dimensional (3D) CdS/Al_2O_3 and 3D CdS/ZnO heteroarrays (hereafter, CdS/oxide) having urchin-like morphology. In this chapter, we have demonstrated the growth of 1D CdS NWs on ZnO and Al_2O_3 and study their photocatalytic properties for hydrogen generation and degradation of organic dye. These semiconductor nanostructured metal chalcogenides metal oxide heteroarrays have unveiled exceptionally high rates of photocatalytic H_2 generation from water and photodegradation of organic dye. The present report mainly highlights the cost effective synthesis of hierarchical 3D catalyst by hydrothermal method which exhibits high rate of hydrogen production and efficient dye degradation without use of noble metals as co-catalyst.

3A.2. Experimental Section

3A.2.1. Synthesis of Hierarchical 3D CdS/Metal Oxide Binary Heteroarrays

Freestanding CdS NWs were synthesized by the method discussed in chapter 2 section 2.3.1. In a typical synthesis of hierarchical 3D CdS/Al_2O_3; $Al(NO_3)_3.9H_2O$ (1.5 g, 3.9 mmol) was dissolved in 10 mL of water, followed by the addition of aqueous NH_3 (to attain pH ~7), thioglycolic acid (1 mL, 9 mmol) under vigorous stirring, and $Cd(CH_3COO)_2.2H_2O$ (2.39 g, 9 mmol). The reaction mixture was stirred for 30 min at room temperature and then kept in an oven at 140 °C for 48 h in a Teflon-lined stainless steel autoclave. Products were washed with warm ethanol and dried under vacuum. ZnO-templated growth of CdS was carried out on ex situ-generated ZnO, followed by the same procedure adopted in the case of CdS/Al_2O_3. 1D CdS NWs were grown hydrothermally by mixing thioglycolic acid and $Cd(CH_3COO)_2.2H_2O$ in appropriate mole ratio in the absence of any template. CdS-free ZnO NPs were also synthesized by adopting the procedure reported by Becheri *et al.*[15] as discussed in the chapter 2 section 2.3.3. $ZnCl_2$ (5.5 g, 40 mmol) was dissolved in 200 mL of distilled water at 90 °C, and 16 mL of 5M NaOH aquous solution was then added dropwise with gentle stirring over a time period of 10 min. ZnO NPs were separated from the supernatant dispersion by sedimentation method and the remaining suspension was washed with distilled water. Purified particles were treated with 2-propanol in the ultrasonic bath for 10 min at room temperature, collected by centrifugation, and maintained at 250 °C for 5 h in a Teflon-lined stainless steel autoclave to obtain the ZnO nanoparticles. Directed growth process of CdS NWs into alumina particles was *in-situ*, whereas that of ZnO was *ex-situ*. The *ex-situ* generation of ZnO was introduced to avoid the formation of zinc sulfide under in situ reaction conditions pertaining to the solubility product issues.

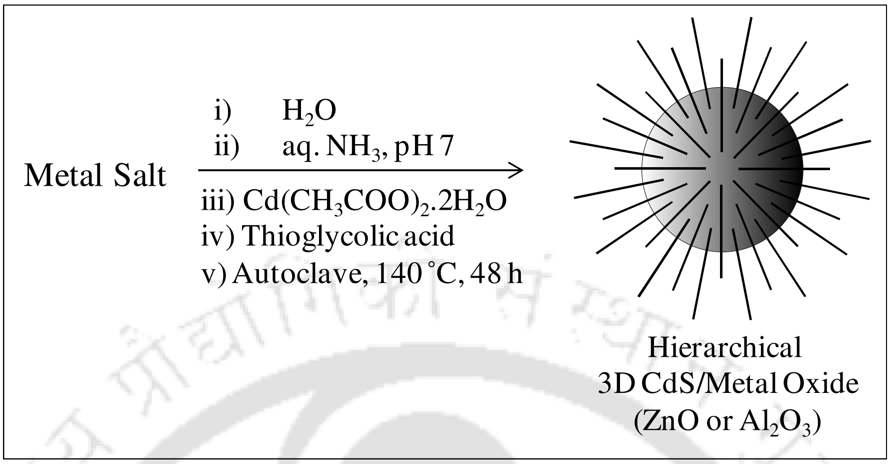

3A.3. Results and Discussions

3A.3.1. Mechanism for the Formation of Hierarchical 3D CdS/Al_2O_3

The mechanistic aspects of 1D CdS NWs growth on alumina appear to be following two steps as shown in Scheme 3A.1: (i) Dissociation of aluminum nitrate to form nano alumina particles and (ii) Formation of a CdS layer followed by the growth of saturated cadmium sulfide into nanowires as depicted in Scheme 3A.1**.** The principle reason behind choosing alumina as a template is evident from the fact that alumina has the typical Lewis acid character with the acidity center on Al^{3+}; hence S^{2-} ions will preferably attach to the alumina.[16] The presence of cadmium ions in the solution induces the formation of CdS colloidal particles on the alumina. Saturated CdS particles will act as a seed crystal for the growth of nanowires from the supersaturated vapors of Cd^{2+} and S^{2-} at a temperature of 140 °C in hydrothermal conditions. Please note that the self-seeded CdS NWs were hardly observed in the reaction mixture in the presence of alumina, although pure cadmium sulfide nanowires were grown in the same reaction condition without the alumina particles, indicating that the heterogeneous surface growth dominated the reaction kinetics at this stage.

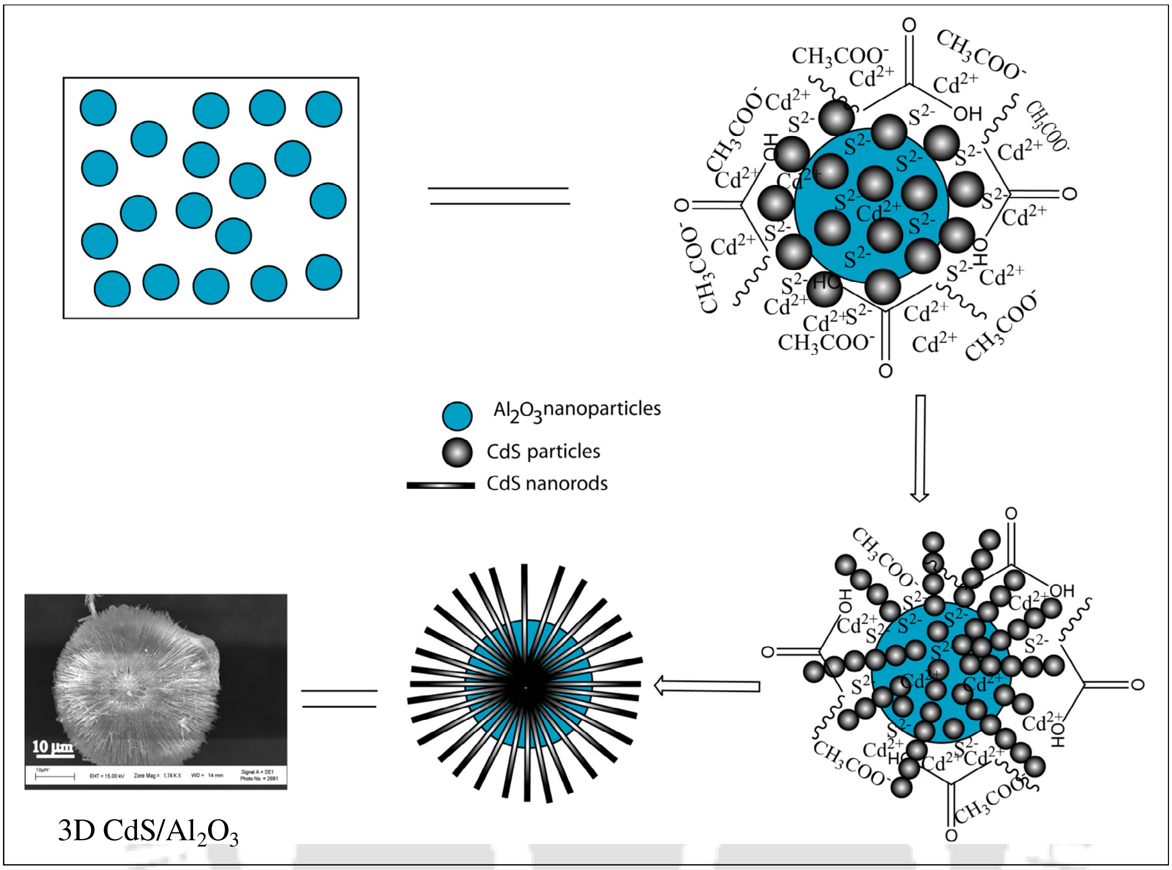

Scheme 3A.1 Schematic of the growth mechanism of CdS NWs, chemically anchored by an *in-situ* generated alumina template

3A.3.2. Powder X-ray Diffractogram

Powder X- ray diffraction patterns for 1D CdS NWs, ZnO NPs, 3D CdS/Al_2O_3, and 3D CdS/ZnO are shown in Figure 3A.1. The crystal planes (100), (002), (101), (102), (110), (103), (112), (201), and (203) for CdS in the diffractogram (Figure 3A.1a) can be indexed to the formation of crystalline hexagonal CdS (hex-CdS) with cell constants a = 0.4136 nm and c = 0.6713 nm (JCPDC reference 06-0314). No diffraction peaks from the other crystalline forms are detected. Interestingly, the same diffraction peaks for CdS can also be seen in the diffractograms for hierarchical 3D CdS/Al_2O_3 and 3D CdS/ZnO photocatalysts. This reveals that the structure and crystallinity of 1D CdS NWs is retained even after it is grown onto the oxide templates to produce CdS/oxide nanourchins. The calculated crystallite size of 1D CdS NWs, by use of the Debye-Scherrer equation from full width at half-maximum (FWHM) values of the hex-CdS planes, is found to be 28 nm. Figure 3A.1b represents the diffractogram for the formation of ZnO NPs; the crystal planes (100), (002), (101), (102), (110), (103), (200), (112), and (201) for ZnO are indexed to the hexagonal phase of ZnO with cell constants a = 0.3249 nm and c = 0.5205 nm (JCPDC reference 05-0664). The unit cell parameter calculation the samples were also carried out and compared with the above mentioned referenced cards which are given in Table 3A.1.

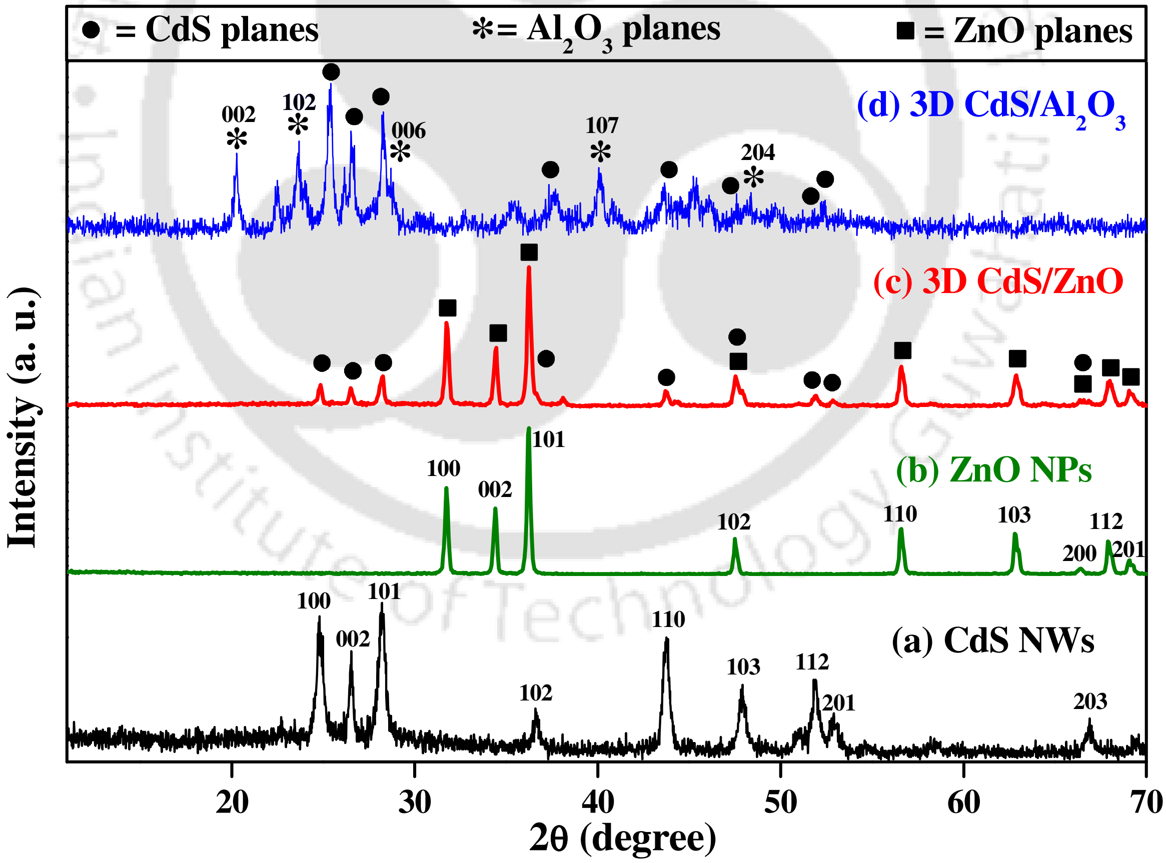

Figure 3A.1 Powder X-ray diffraction patterns for (a) CdS NWs, (b) ZnO NPs, (c) Hierarchical 3D CdS/ZnO, and (d) Hierarchical 3D CdS/Al_2O_3

The 1D CdS NWs we have synthesized are purely of hexagonal phase. Matsumura et al.[17] had reported the advantage of hex-CdS over bulk-phase c-CdS toward higher H_2 production rate and higher photocatalytic efficiency. In general, it is observed that easy and effective process to synthesize hex-CdS is calcination. Increased calcination temperature favors good crystallinity of CdS, but calcination at high temperature decreases the surface area of the photocatalyst. Moreover, high temperature increases the possibility of formation of CdO from CdS species, wherein CdO acts as a photocatalytic activity inhibitor because of its more positive CB position than the redox potential of H^+/H_2.[18] Thus, the XRD results clearly point out that CdS NWs can be easily synthesized and grown onto the metal oxide cores under the current synthetic conditions at a temperature of 140 °C without calcination.

Table 3A.1 Comparison of unit cell parameters with that of the reported referenced card (JCPDS 06-0314 and JCPDS 05-0664)

Samples	**Unit Cell Parameters (Calculated)**	**Unit Cell Parameters (Reported)**
CdS NWs	a = 0.3936 nm & c = 0.6691 nm	a = 0.4136 nm & c = 0.6713 nm
CdS in 3D CdS/Al_2O_3	a = 0.3994 nm & c = 0.67 nm	a = 0.4136 nm & c = 0.6713 nm
CdS in 3D CdS/ZnO	a = 0.4041 nm & c = 0.668 nm	a = 0.4136 nm & c = 0.6713 nm
ZnO NPs	a = 0.3194 nm & c = 0.519 nm	a = 0.3249 nm & c = 0.5205 nm
ZnO in 3D CdS/ZnO	a = 0.3189 nm & c = 0.5188 nm	a = 0.3249 nm & c = 0.5205 nm

3A.3.3. UV-Vis Diffuse Reflectance Spectra

The UV-Vis diffuse reflectance spectra of 1D CdS NWs, 3D CdS/Al_2O_3, and 3D CdS/ZnO are shown in Figure 3A.2, where normalized absorptions of the photocatalysts are plotted against wavelength. All these spectra are recorded in the wavelength range of 325-750 nm. Interestingly, all these photocatalysts show almost the same absorption profile with a steep absorption edge in 480-520 nm wavelength range, which corresponds to the band gap energy for the 1D CdS NWs. As can be seen, there are two sharp absorption steps for hierarchical 3D CdS/ZnO photocatalyst; one at *ca.* 380 nm is for ZnO and the other at *ca.* 512 nm is for CdS. The same type of absorption curve is also expected for hierarchical 3D CdS/Al_2O_3; however, only one step at *ca.* 496 nm for CdS is observed. This is because of the high band-gap energy or low wavelength value ($\lambda < 200$ nm) for the Al_2O_3 template. For all the systems, the completely diminished absorption curves after 570 nm indicate the absence of impurity energy level transitions.

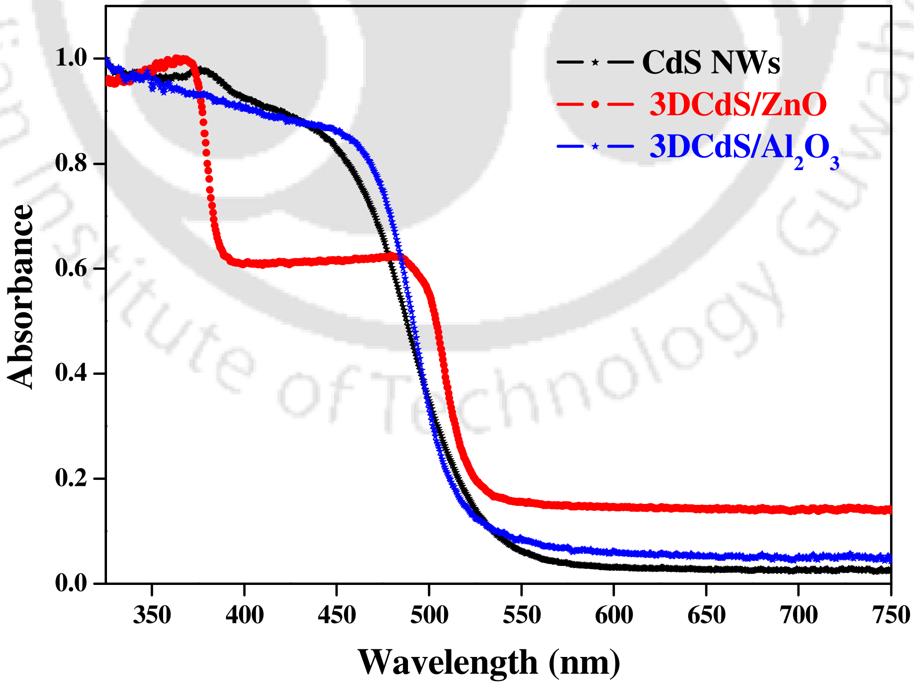

Figure 3A.2 UV-Vis diffuse reflectance spectra for 1D CdS NWs, hierarchical 3D CdS/Al_2O_3, and 3D CdS/ZnO photocatalysts

Optical band gap calculations are carried out for hierarchical 3D CdS/Al_2O_3 and 3D CdS/ZnO using Tauc's relationship. Tauc's relationship for band-gap calculations is described as

$$(\alpha h\nu)^{1/n} = \mathrm{C} \times (h\nu - E_g),$$

where α is the absorption coefficient of the semiconductor at a certain value of wavelength λ, h is Planck's constant, C is the proportionality constant, ν is the frequency of light, E_g is the band gap energy, and n = 1/2 and 2 for direct and indirect transition mode materials, respectively. The absorption coefficient is estimated from the equation

$$\alpha = -\frac{1}{t} \times \ln\left(\frac{I_t}{I_0}\right) = \frac{1}{t} \times A \times \log e,$$

where A, t, I_t, and I_0 represent the absorbance, thickness of the photocatalyst film, intensity of transmitted light, and intensity of incident light, respectively.

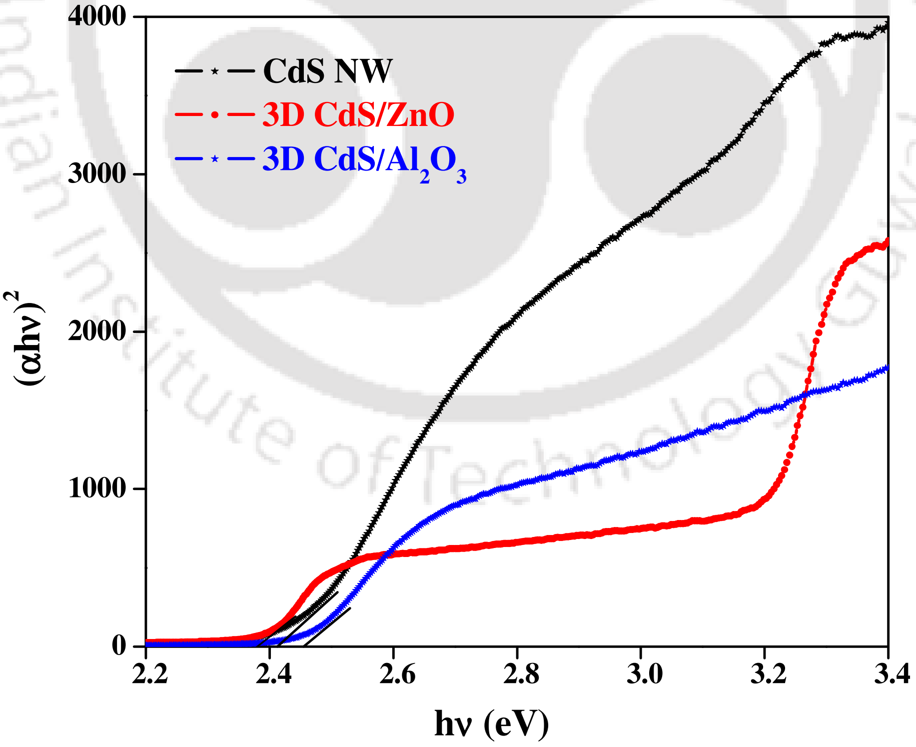

Figure 3A.3 Tauc's plot of $(\alpha h\nu)^2$ *versus* photon energy ($h\nu$) for optical band-gap calculations for CdS NWs, hierarchical 3D CdS/Al_2O_3 and 3D CdS/ZnO

The Figure 3A.3 shows Tauc's plot for the CdS systems, where $(\alpha h\nu)^2$ is plotted against the photon energy ($h\nu$) and the band gap energies are estimated from the extrapolated lines as shown in the Figure 3A.3. The band gaps obtained from Tauc's plot are found to be 2.45 eV for 1D CdS NWs, 2.48 eV for hierarchical 3D CdS/Al_2O_3, and 2.41 eV for 3D CdS/ZnO.

3A.3.4. Materials Morphology

Scanning electron microscopy (SEM) and transmission electron microscopic (TEM) images of the hydrothermally synthesized 1D CdS NWs are shown in Figure 3A.4 and Figure 3A.5. Figure 3A.4a & b shows SEM images of as-prepared CdS sample at different magnifications in which slightly aggregated and randomly oriented rods can be observed. Figure 3A.4a - d shows the TEM images of as prepared CdS NWs at different magnifications. From TEM analysis CdS NWs have an approximate diameter of 40 nm (Figure 3A.4d). The high resolution TEM image (HR-TEM) reveals the crystallized CdS NWs with lattice spacing of 0.37 nm, corresponding to the (100) plane (Figure 3A.4e). The selected area electron diffraction (SAED) pattern confirms the crystallinity of pure hex-CdS (Figure 3A.4f). Electron-dispersive X-ray spectroscopy (EDX) of the CdS NWs shown in inset to Figure 3A.4b confirms the presence of Cd and S only. More confirmation for the homogeneous impregnating growth of CdS NWs over the metal oxide templates to generate an urchin-like shape is carried out by SEM imaging of 3D CdS/Oxide.

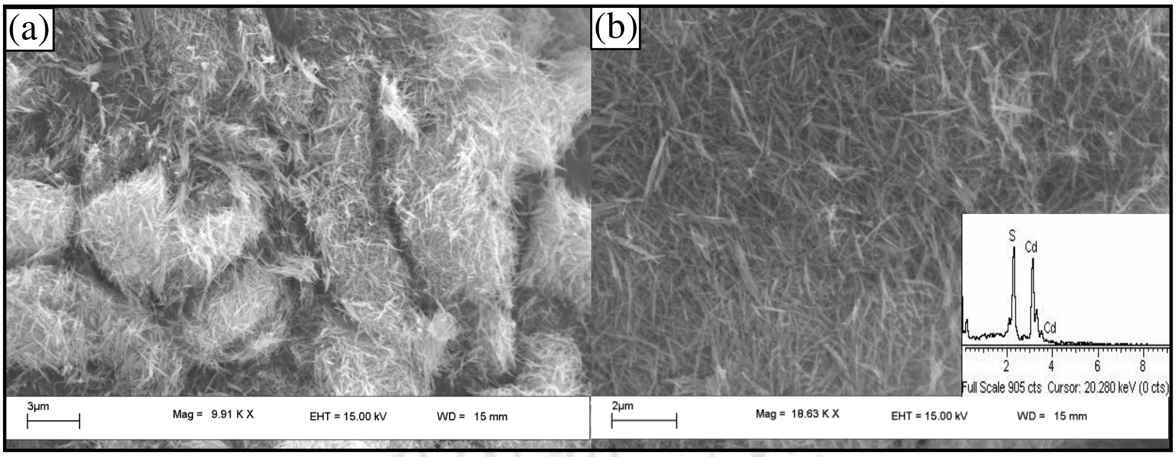

Figure 3A.4 (a and b) Scanning Electron Microscopic images at different magnifications, inset to (b) shows the EDX pattern of free standing CdS NWs

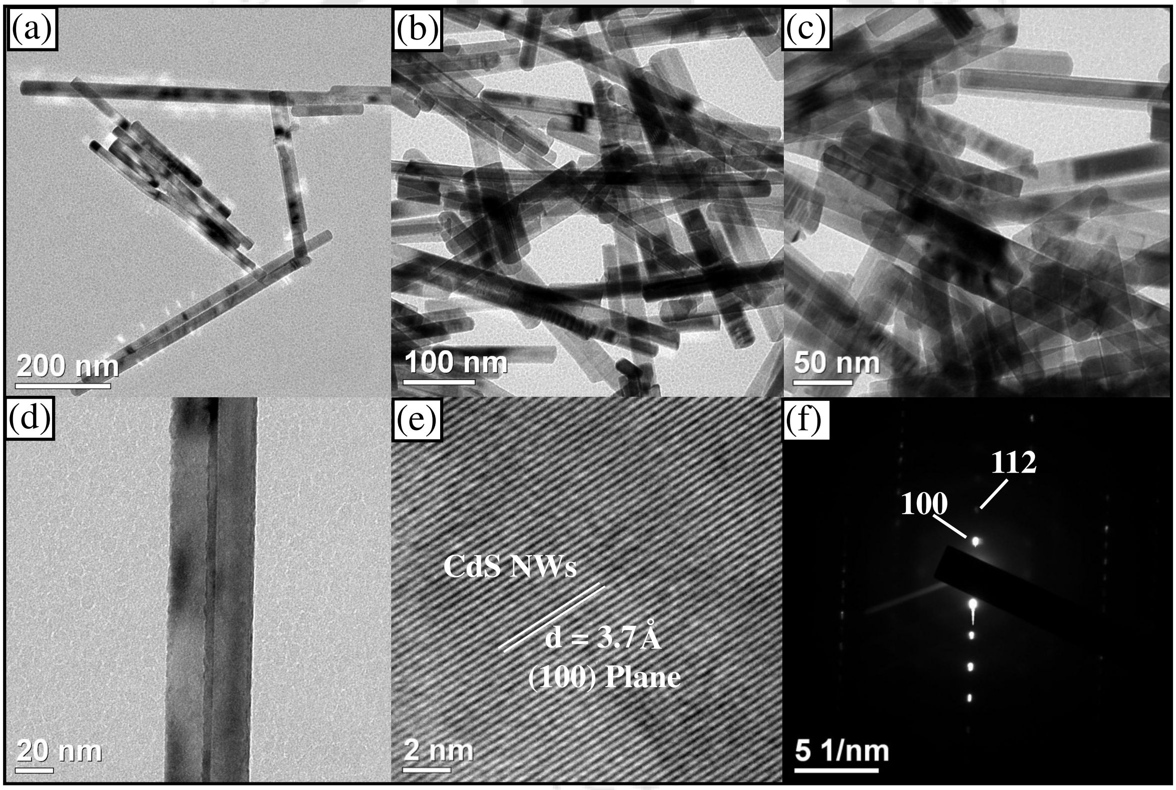

Figure 3A.5 (a-d) Transmission Electron Microscopic image at different magnifications, (e) High Resolution-TEM image represents (100) plane and (f) Selected Area Electron Diffraction pattern of hydrothermally prepared CdS NWs. Inset (b) energy dispersive X-ray spectroscopy of CdS NWs

Figure 3A.6a-f shows the morphology of 3D CdS/Al_2O_3 nano-urchins at different magnifications as observed by SEM. The SEM images of the 3D CdS/Al_2O_3 depicted the formation of three dimensional hierarchical structures of about 5-10 μm in size. SEM images confirm that the CdS NWs exhibit organized urchin-like architectures in which each nano-urchin is made up of many CdS NWs aligned in a radial way and appear to be originated from a single bunch of alumina nanoparticles (Figure 3A.6b & c).

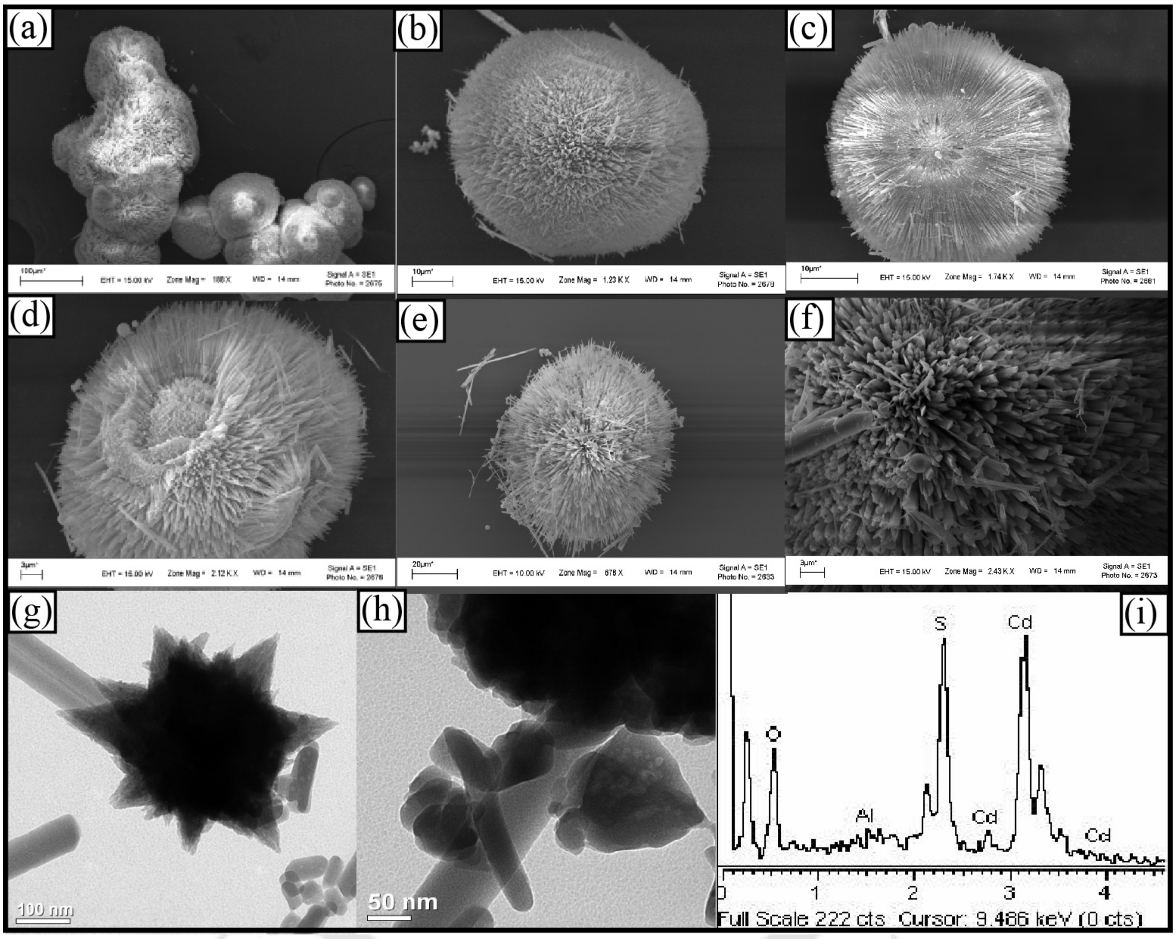

Figure 3A.6 (a-f) SEM images at different morphology exhibiting the formation of urchin-like morphology (g and h) TEM image at varied magnification (i) EDX analysis for 3D CdS/Al_2O_3

Self-seeded CdS NWs were hardly observed in the reaction mixture in the presence of alumina, although pure CdS NWs were grown in the present reaction condition without the alumina particles, indicating that the heterogeneous surface growth dominated the reaction kinetics at this stage. Figure 3A.6g & h shows TEM image of CdS/Al_2O_3 microsphere at higher magnification, reveals that 3D CdS/Al_2O_3 microsphere are assembled from 1D CdS NWs. Figure 3A.6i shows the EDX analysis of hierarchical 3D CdS/Al_2O_3 nanourchin and indicates the presence of Cd, S, Al, and O in the sample.

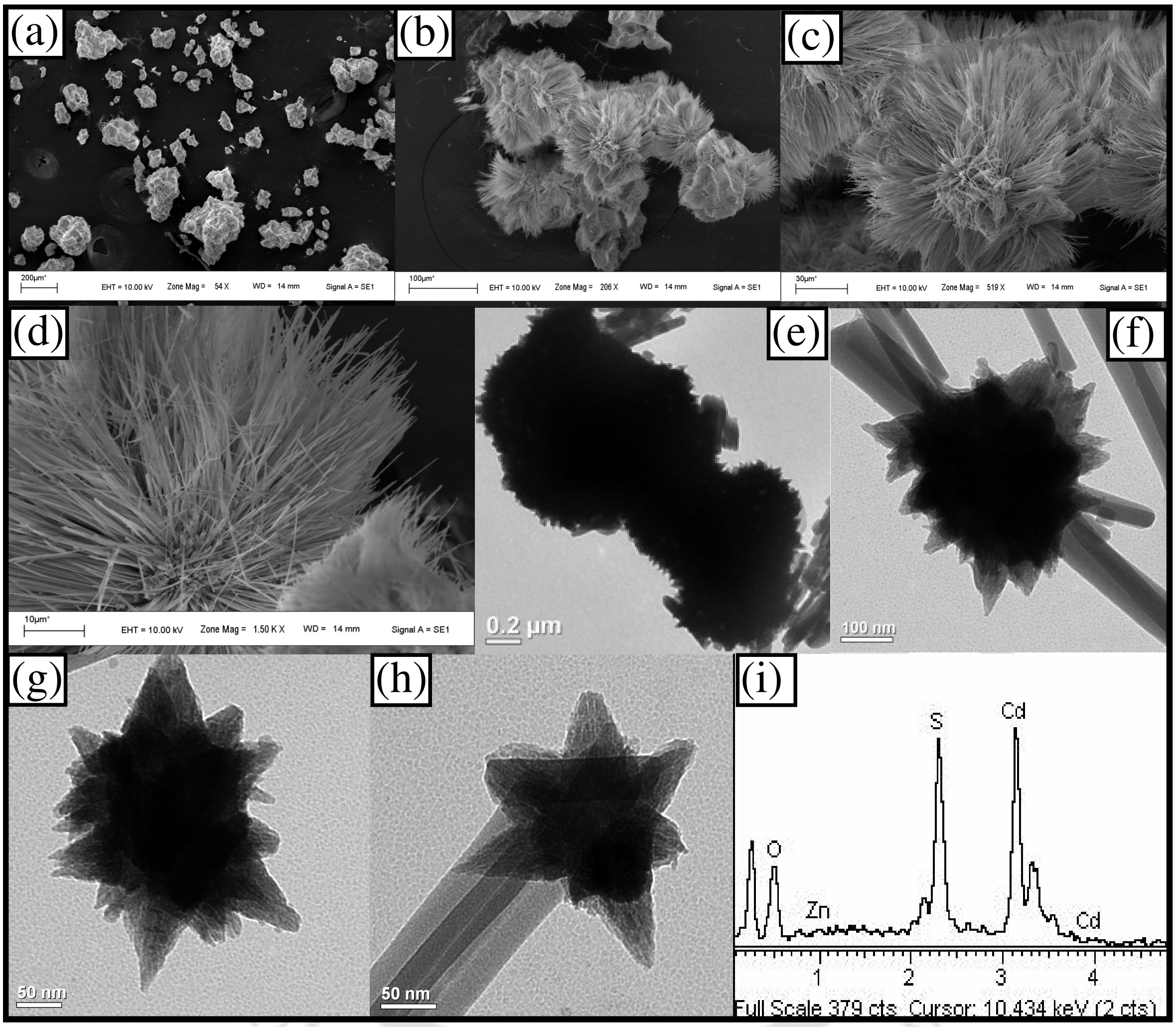

Figure 3A.7 (a-d) SEM images at different morphology shows the formation of urchin-like morphology (e) TEM image at high magnification, particles appeared as dark patches (f-h) TEM image at low magnification (i) EDX analysis for 3D CdS/ZnO

The SEM images of hierarchical 3D CdS/ZnO photocatalyst at different magnifications are shown in Figure 3A.7a-d, confirms the formation of nano urchin-like structure of 3D CdS/ZnO. The urchin-like morphology of 3D CdS/ZnO is further supported by the TEM image in Figure 3A.7e-h, where in the growth of CdS NWs over ZnO NP are observed. Figure 3A.7i shows the energy dispersive X-ray pattern of the hierarchical 3D CdS/ZnO indicating the presence of Cd, S, Zn, and O in the sample. Please note that TEM analysis the sample was prepared from the supernatant of the dispersion having smaller size in order to see the clear structure of the heteroarrays. At high magnifications, the morphology of the particles was not clear using TEM, as they appeared as dark patches (Figure 3A.7e). Thus, the SEM and TEM images of the photocatalysts demonstrate the urchin-like heteroarrays by growing CdS NWs onto a wide-band-gap semiconductor core of choice.

3A.3.5. BET Surface Area Analyses

Figure 3A.8 shows the N_2 adsorption-desorption isotherm and corresponding curves of the pore size distribution (inset) for hierarchical 3D CdS/ZnO and 3D CdS/Al_2O_3 along with CdS NWs. According to the Brunauer-Deming-Deming-Teller (BDDT) classification, the majority of physisorption isotherms can be grouped into six types.[19] All the samples in the present study follows a typical type IV isotherms and type H3 hysteresis loops, which are the characteristic feature of mesopores. As can be seen (inset, Figure 3A.8), CdS NWs, hierarchical 3D CdS/Al_2O_3, and 3D CdS/ZnO have similar isotherms with almost the same pore diameter, which indicates that the surface morphology of CdS NWs remains same even after its growth on ZnO and Al_2O_3.The BET surface areas for CdS NWs, hierarchical 3D CdS/Al_2O_3, and 3D CdS/ZnO are shown in Figure 3A.9. The BET surface areas for 3D CdS/Al_2O_3 (87 m^2g^{-1}) and 3D CdS/ZnO (56 m^2g^{-1}) nanourchins are enhanced in contrast to that of CdS NW (30 m^2g^{-1}), due to the formation of urchin-like morphology of 3D CdS/oxide.

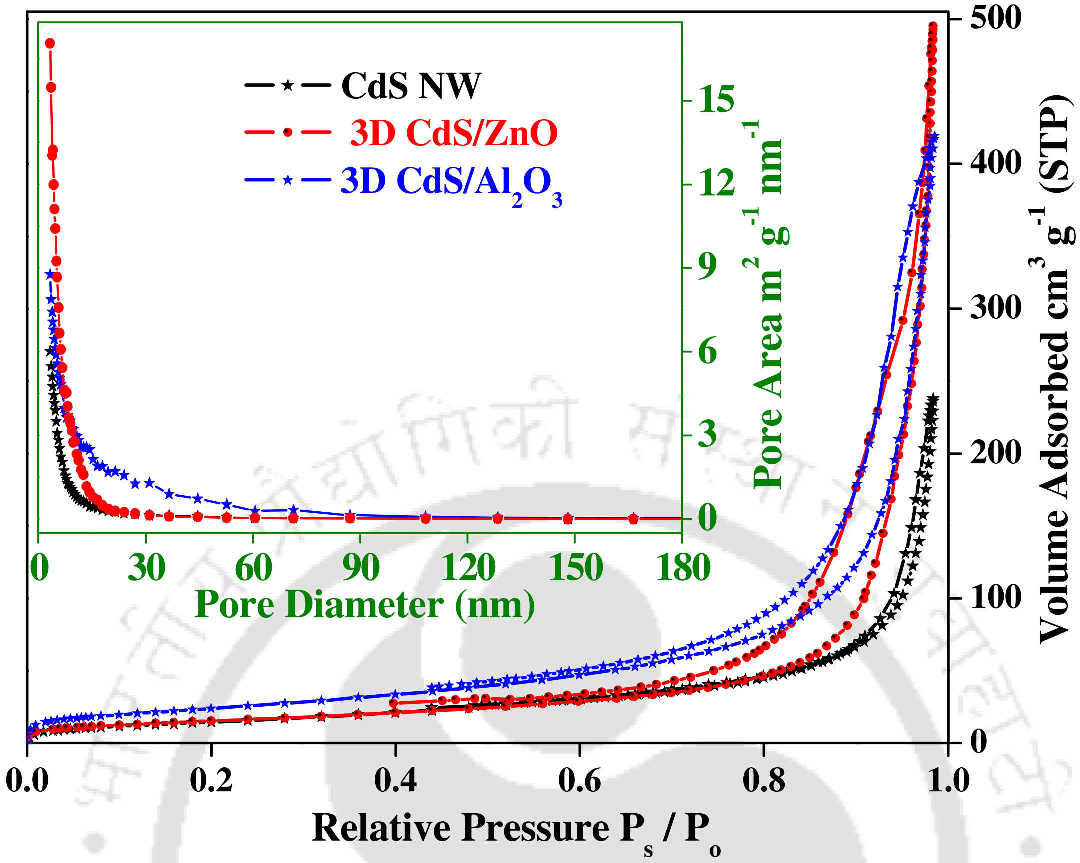

Figure 3A.8 Nitrogen adsorption-desorption isotherms and pore-size distribution plots for CdS NWs, hierarchical 3D CdS/Al_2O_3, and 3D CdS/ZnO photocatalysts. Inset represents plot of pore area versus pore diameter

3A.3.6. Photocatalytic Hydrogen Generation

Photocatalytic H_2 production rates for the designed photocatalysts CdS NWs, hierarchical 3D CdS/Al_2O_3, and 3D CdS/ZnO under visible-light irradiation in the presence of sacrificial reagents are shown in Figure 3A.9. From the Figure 3A.8, the H_2 evolution rates are determined to be 530, 724, and 1008 µmol/h for CdS NWs, 3D CdS/Al_2O_3, and 3D CdS/ZnO, respectively. The inset to Figure 3A.9 shows the percentage AQY values for the photocatalysts; AQY for CdS NWs, 3D CdS/Al_2O_3, and 3D CdS/ZnO are found to be at 8%, 11%, and 15%, respectively. As can be seen from Table 3A.2, 3D CdS/Al_2O_3 and 3D CdS/ZnO hierarchical structures show higher AQY than most of the previously reported CdS-based photocatalysts from the literature.

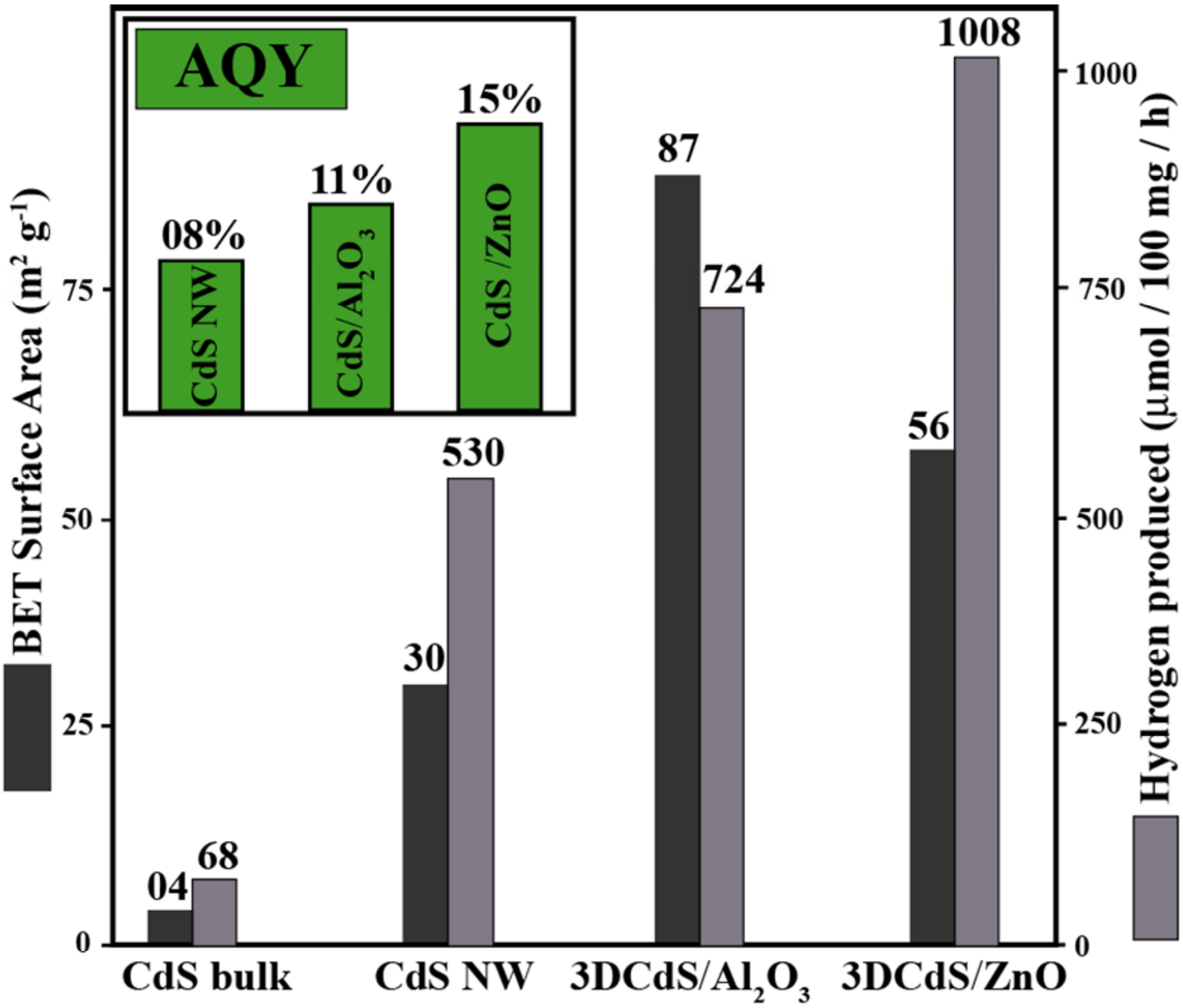

Figure 3A.9 Brunauer Emmett Teller surface area plot and amounts of H_2 generated from CdS bulk, CdS NW, 3D CdS/Al_2O_3, and 3D CdS/ZnO photocatalysts. (Inset) Percentage AQY for CdS NW, 3D CdS/Al_2O_3, and 3D CdS/ZnO photocatalysts

The enhanced H_2 production rates for hierarchical 3D CdS/Al_2O_3 and 3D CdS/ZnO in contrast to that of CdS NWs are due to the urchin-like morphology with enhanced BET surface area. It is worth noting that 3D CdS/ZnO has a high rate of H_2 production in spite of having lower BET surface area than 3D CdS/Al_2O_3. This increased hydrogen production rate is attributed to the facile intersystem charge transfer in the case of 3D CdS/ZnO.

Table 3A.2 AQY values of CdS based photocatalysts for hydrogen generation under visible light irradiation

Photocatalyst	synthetic method	co-catalyst	AQY* (%)	ref
CdS:Mn	hydrothermal	RuO	7	20
$Cd_{1-x}Zn_xS$ (x = 0.2)	thermal sulfurization	-	10.23	20
Pt/CdS NWs	chemical deposition	-	3.9	20
CdS/ZnO	two step precipitation	Pt	3.2	11
SrS/CdS	precipitation	Pt	5.83	21
CdS/ZnS	H_2S thermal sulfurization	-	10.2	20
CdS/ ZPT	-	-	5.84	22
CdS/Graphene	solvothermal	Pt	22.5	23
CdS/MWCNT	hydrothermal	-	2.16	24
$CdS/KNbO_3$	ion adsorption, precipitation	NiO	8.8	20
$Ni/NiO/KNbO_3/CdS$	-	-	4.4	25
3D CdS/Al_2O_3	hydrothermal	-	11	Present work
3D CdS/ZnO	hydrothermal	-	15	Present work

*The value of AQY varies with the evaluation method and the system of interest.

The proposed mechanism of charge transfer in the case of 3D CdS/ZnO is shown in the schematic 3A.2. The band positions of CdS and ZnO[26] clearly facilitates the feasibility of intersystem charge transfer in 3D CdS/ZnO nanourchin from CdS to ZnO due to the more negative potentials of the CB and VB edges of CdS than those of ZnO. Furthermore, the nanourchin design of 3D CdS/ZnO constructs an intimate contact between CdS and ZnO, which is crucial to promote the intersystem electron transfer between them. The visible light irradiation generates electron-hole pairs in CdS, but no charges are generated in ZnO, which increases the probability of the transferred electrons being accumulated in the CB of ZnO. These electrons are then utilized for the reduction of H^+ ions to form atomic H, generating H_2 gas. At the same time, the lower positive potential of VB of CdS with respect to ZnO restricts the photogenerated holes to remain in the VB of CdS itself. The sacrificial agents consume these holes in the VB rapidly, preventing the electron hole pair recombination.

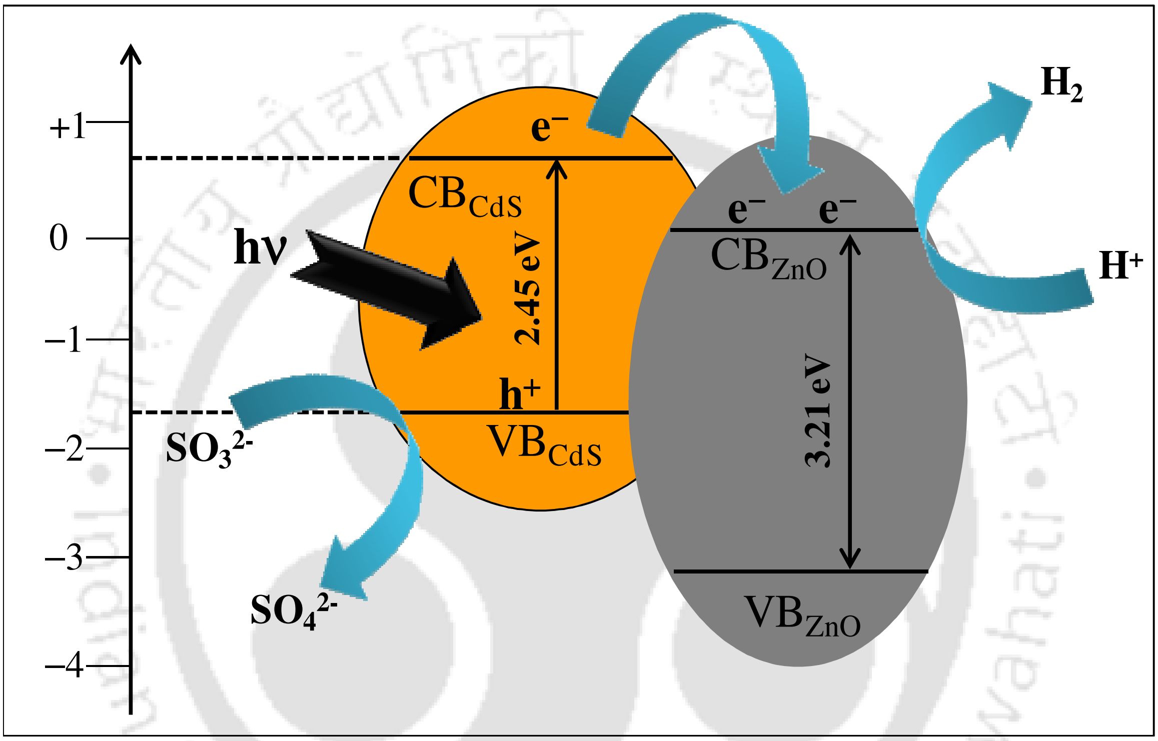

Scheme 3A.2 Schematic of the band positions and the process of efficient charge transfers between CdS and ZnO in the hierarchical 3D CdS/ZnO. Effective charge transfer makes 3D CdS/ZnO efficient photocatalyst for hydrogen generation

It is noteworthy that the design of nanourchin approach is different than the conventional core-shell structures, because in the core-shell structures the accessibility of the core surface is minimal due to its coverage by the shell. The uniqueness of the urchin-like structures lies in the sense that although CdS NWs are impregnated on the core oxide layers, still the surface of the core is accessible for the reduction of water molecules.

3A.3.7. Photocatalytic Dye Degradation

Apart from the efficient H_2 production, 3D CdS/Oxide exhibits excellent photocatalytic activity for the degradation of organic dye. In order to examine the photocatalytic activity, dye degradation experiments were performed in the presence of photocatalysts 1D CdS NWs, 3D CdS/Al_2O_3 and 3D CdS/ZnO with methyl orange (MO) as a reference dye. The photo-degradation of MO was studied by measuring the concentration of the dye after irradiation with visible light for varying time periods. The intensity of absorption peak at 464 nm of MO aqueous solution was monitored for assessing the change in concentration. The absorption spectra of MO with 1D CdS NWs, 3D CdS/Al_2O_3 and 3D CdS/ZnO at 60 min interval is shown in Figure 3A.10. The concentration of un-degraded MO relative to its initial concentration (C/C_0) after irradiation in presence of 1D CdS NWs, 3D CdS/Al_2O_3 and 3D CdS/ZnO photocatalyst at different time intervals are shown in Figure 3A.10d. From Figure 3A.10d, it is clear that, with hierarchical 3D CdS/ZnO highest degradation of MO was achieved compared to that of hierarchical 3D CdS/Al_2O_3 and 1D CdS NWs. The MO degradation was observed to follow a first order decay kinetics with all photocatalyst, as seen from the apparent first order linear transform $\ln(C/C_0) = -k_{app}t$,[27] shown in Figure 3A.10d. Where C_0 and C represent the concentration of MO before and after irradiation respectively, k_{app} is the apparent first-order reaction rate constant representing the reaction rate and could be calculated from the slope of the plot (Figure 3A.10d). The degradation efficiencies (E_{ff}) for 1D CdS NWs, 3D CdS/Al_2O_3 and 3D CdS/ZnO were estimated based on the initial and final concentration of the dye.[28] It was found that 3D CdS/ZnO and 3D CdS/Al_2O_3 were able to degrade the dye with 97% and 83% efficiency whereas, 1D CdS NWs showed efficiency of about 72%.

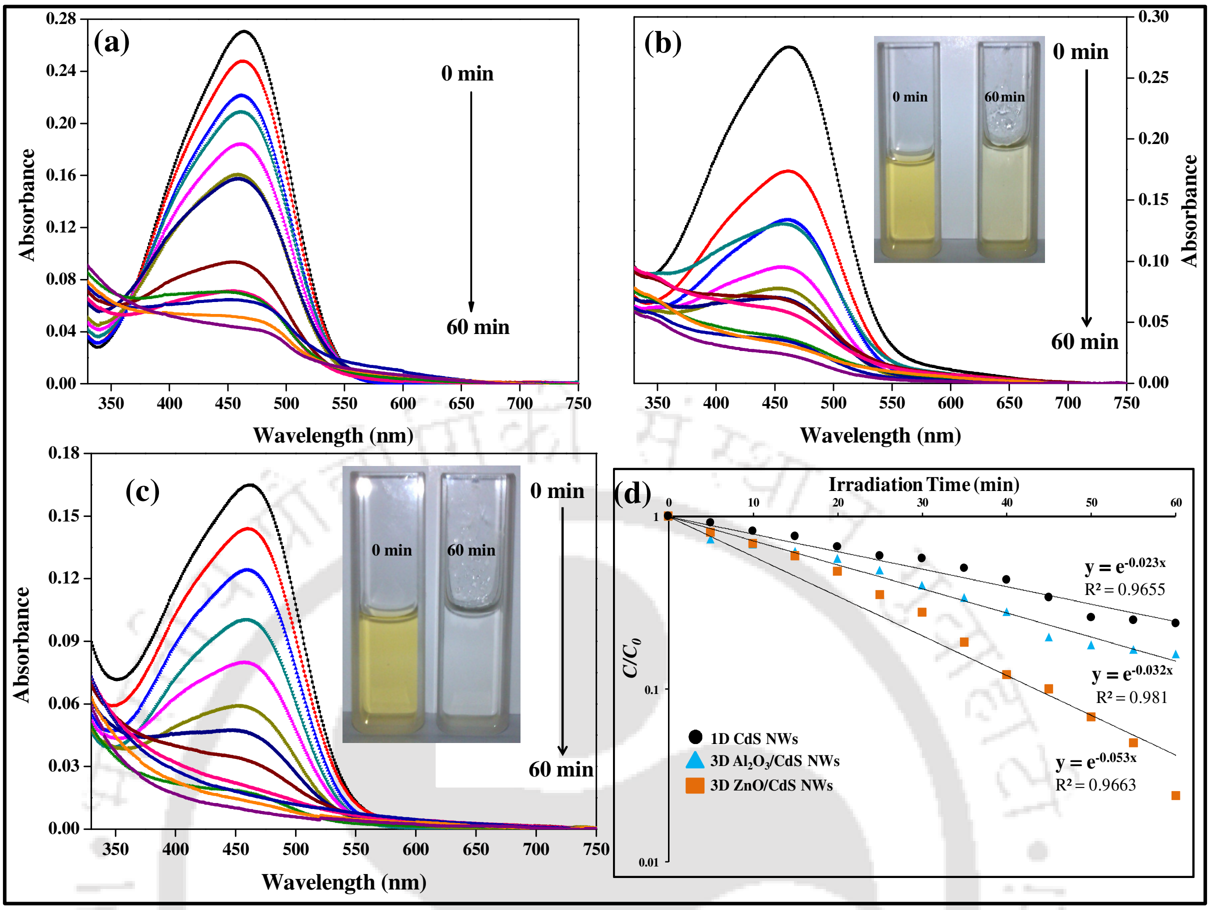

Figure 3A.10 UV-Vis absorption spectra of aqueous methyl orange with (a) 1D CdS NWs (b) hierarchical 3D CdS/Al_2O_3 (c) hierarchical 3D CdS/ZnO under visible light irradiation (d) evolution of apparent rate constant (k_{app}) versus irradiation time in the presence of CdS NWs, 3D CdS/Al_2O_3 NWs and 3D CdS/ZnO photocatalyst

The high photocatalytic degradation efficiency for hierarchical 3D CdS/Al_2O_3 is mainly attributed to the enhanced specific surface area however; for 3D CdS/ZnO high degradation efficiency is ascribed due to enhanced surface to volume ratio for improved mass transfer and effectual separation of photoinduced electron hole pairs. It should be noted that 3D CdS/Al_2O_3 has higher BET surface area value (87 m^2g^{-1}) than 3D CdS/ZnO (56 m^2g^{-1}), but it is the efficient charge separation in 3D CdS/ZnO which makes it more active photocatalyst. Based on the previous literature,[29] we propose a mechanism for the facile charge transfer between CdS and ZnO. A schematic elucidation for the efficient charge separation along with the generation of hydroxyl radical in the presence of hierarchical 3D CdS/ZnO is shown in scheme 3A.3. Irradiation of visible light onto the photocatalyst causes its activation, leading to the formation of reductive electrons in CB and oxidative holes in VB of CdS; nevertheless, no charge formation takes place in ZnO CB due to its inactivity under visible light. The CB of CdS (–0.88 eV) is in proximity with the CB of ZnO (–0.20 eV) which facilitate migration of reductive electron from CB of CdS to CB of ZnO, thereby reducing the electron hole pair recombination. The reduction in the rate of electron hole pair recombination increases the lifetime of the charge carriers and enhances the efficiency of the interfacial charge transferred to the adsorbed substrates, leading to higher photocatalytic activity of the hierarchical 3D CdS/ZnO catalyst than 3D CdS/Al_2O_3 and 1D CdS NWs catalysts.

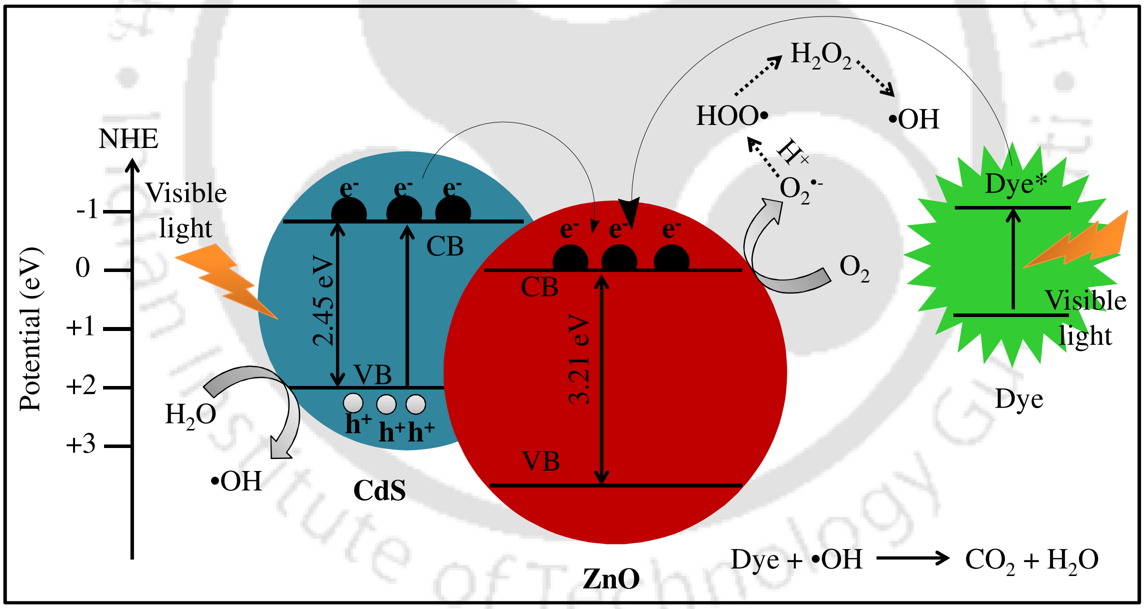

Scheme 3A.3 Schematic illustration of the efficient electron transfer and generation of hydroxyl radicals by excitation of 3D CdS/ZnO under visible light irradiation

3A.3.7.1. Mechanism for Dye Degradation

The degradation of MO involves several steps and the proposed mechanism is shown in scheme 3A.4. Irradiation of visible light leads to the formation of electrons in the CB and holes in the VB of the semiconductor. The photogenerated electrons in CB of CdS can get transferred to the CB of ZnO (step 1), inducing the reduction of the molecular oxygen O_2 to superoxide radical anion $O_2^{\bullet -}$ (step 2). In aqueous medium (dissolved oxygen), holes react with water to produce hydroxyl radical (step 3). The hydroxyl radicals can recombine to form H_2O_2 (step 4). H_2O_2 can react with superoxide radical anion to regenerate hydroxyl radical (step 5) thereby decomposing the organic dye to carbon dioxide and water (step 6).[30]

$$\mathbf{CdS/ZnO + h\nu \longrightarrow CdS(h^+)/ZnO(e^-)} \qquad \textbf{Step 1}$$

$$\mathbf{ZnO(e^-) + O_2 \longrightarrow O_2^{\bullet -}} \qquad \textbf{Step 2}$$

$$\mathbf{CdS(h^+) + H_2O \longrightarrow {\bullet}OH + H^+} \qquad \textbf{Step 3}$$

$$\mathbf{{\bullet}OH + {\bullet}OH \longrightarrow H_2O_2} \qquad \textbf{Step 4}$$

$$\mathbf{H_2O_2 + O_2^{\bullet -} \longrightarrow {\bullet}OH + {}^{-}OH + O_2} \qquad \textbf{Step 5}$$

$$\mathbf{Dye + {\bullet}OH \longrightarrow CO_2 + H_2O} \qquad \textbf{Step 6}$$

Scheme 3A.4 Proposed mechanism for organic dye degradation by hierarchical 3D CdS/ZnO

3A.3.7.2. Affirmation for the Formation of Active Species Superoxide Radical Anion ($O_2^{\bullet -}$) and Hydroxyl Radical (•OH)

From the scheme 3A.4, the degradation of MO depends on the concentration of intermediate species superoxide radical anion and hydroxyl radical. The roles of these main active species in dye degradation were investigated. The formation of superoxide radical anion takes place by the reduction of dissolved molecular oxygen in aqueous MO solution (step 2) whereas, formation of hydroxyl radical occurs by the oxidation of adsorbed water as well as through superoxide radical anion (step 3 and step 5). Therefore, it is obvious that variation in the concentration of dissolved molecular oxygen will affect the rate of dye degradation. Thus, to inspect the effect of concentration of dissolved molecular oxygen on the degradation efficiency of MO, degradation experiment was performed in deoxygenated water. The photodegradation rate of MO was studied by measuring the concentration of the MO after irradiation with visible light for varying time periods. The concentration of un-degraded MO with normal water and deoxygenated water in presence of 3D CdS/ZnO and 3D CdS/Al_2O_3 catalyst at different intervals of time are shown in Figure 3A.11c & d.

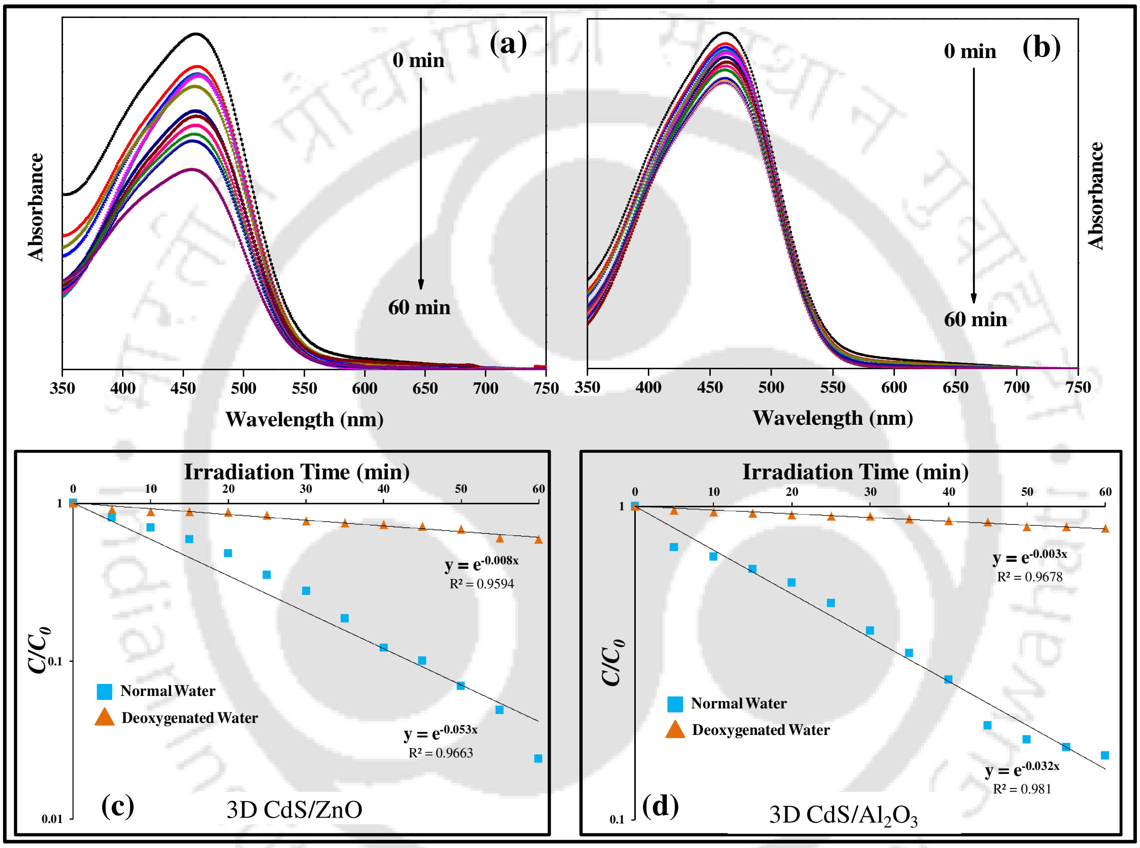

Figure 3A.11 UV-Vis absorption spectra of MO in deoxygenated water with hierarchical (a) 3D CdS/ZnO (b) 3D CdS/Al_2O_3 and the C/C_0 versus irradiation time curves of photodegradation of MO with (c) 3D CdS/ ZnO (d) 3D CdS/Al_2O_3

With the normal water, the photocatalytic degradation efficiency of MO was 97% with 3D CdS/ZnO and 83% with 3D CdS/Al_2O_3, after 60 min of visible light irradiation. However, with deoxygenated water the photocatalytic conversion ratio of main absorption peak of MO was reduced to 41% with 3D CdS/ZnO and 25% with 3D CdS/Al_2O_3 after 60 min of visible light irradiation. The decrease in the degradation efficiency is attributed to the reduction in the concentration of molecular oxygen in MO solution.

The photoinduced holes may react with adsorbed water to produce hydroxyl radical (•OH). These •OH radicals are very unstable and rapidly oxidize MO at the surface of photocatalyst. Thus, the photodegradation rate of MO depends on the concentration of •OH radical. To study the effect of concentration of •OH radical on degradation rate, the MO degradation experiment was performed in presence of additive metal ion (Fe^{2+}). Based on the literature, it is known that Fe^{2+} undergoes the oxidation reaction in the solution with •OH radicals by a simple one electron transfer mechanism.[31]

$$Fe^{2+} + {}^{\cdot}OH \longrightarrow Fe^{3+} + OH^{-}$$

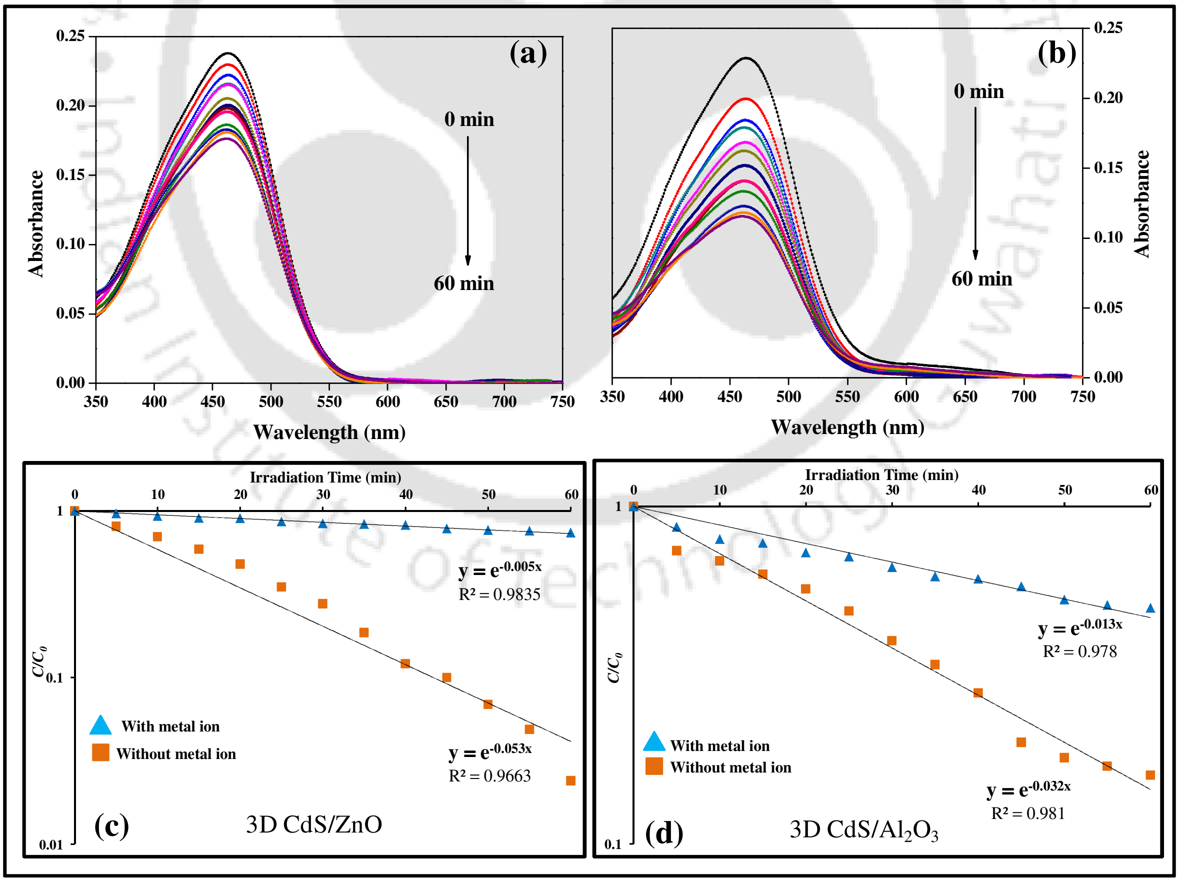

Figure 3A.12 UV-Vis absorption spectra of aqueous MO in presence of scavenger metal ion (Fe^{2+}) with (a) hierarchical 3D CdS/ZnO (b) hierarchical 3D CdS/Al_2O_3 and the C/C_0 versus irradiation time curves of photocatalytic degradation of MO with (c) 3D CdS/ZnO (d) 3D CdS/Al_2O_3

Thus, in presence of Fe^{2+}, hydroxyl radicals are effortlessly converted to OH^{-}, thereby decreasing the concentration of •OH radicals and hence suppressing MO degradation up to 26% for 3D CdS/ZnO and 45% for 3D CdS/Al_2O_3 after 60 min of visible light irradiation. From Figure 3A.12c, d it is clear that the apparent rate constant (k_{app}) for MO degradation in presence of Fe^{2+} is less than that of without metal ion.

3A.4. Conclusion

1- Single step hydrothermal synthesis of hierarchical 3D CdS/Metal Oxide was demonstrated and characterized by Powder X-ray diffractogram, SEM, TEM, UV-Vis diffused reflectance spectra and N_2 adsorption-desorption isotherm.

2- Hierarchical 3D CdS/Metal Oxide acts as highly efficient photocatalyst for hydrogen generation by water splitting without addition of any noble metal co-catalyst (AQY ~ 15% for CdS/ZnO; AQY ~ 11% for CdS/Al_2O_3).

3- Additionally, CdS/Metal Oxide displayed highly efficient photodegradation of azo dye (Methyl Orange as reference organic dye).

4- The kinetics study of Methyl Orange degradation by CdS/Metal Oxide revealed that decay follow first order kinetics with apparent rate constant (k_{app}) value 0.053 min^{-1} for CdS/ZnO and 0.032 min^{-1} for CdS/Al_2O_3.

5- The high photocatalytic activity of 3D CdS/Al_2O_3 is attributed to the enhanced surface area while for 3D CdS/ZnO; high activity is ascribed due to superior surface area and facile charge transfer from CdS conduction band to that of ZnO conduction band.

6- Detailed experiments were performed to explain the dye degradation mechanism. Formation of reactive and unstable intermediates such as superoxide radical anion and hydroxyl radical are being explained with experimental evidence.

7- Present approach offers a viable route to rationally synthesize a variety of visible light driven hetero-arrays for effective photocatalysis for hydrogen generation and degradation of organic pollutants.

References

1) Hotchandani, S.; Kamat, P. V. *J. Phys. Chem.* **1992**, *96*, 6834.
2) Zong, X.; Yan, H. J.; Wu, G. P.; Ma, G. J.; Wen, F. Y.; Wang, L.; Li, C. *J. Am. Chem. Soc.* **2008**, *130*, 7176.
3) Li, Q.; Guo, B.; Yu, J.; Ran, J.; Zhang, B.; Yan, H.; Gong, J. R. *J. Am. Chem. Soc.* **2011**, *133*, 10878.
4) Hoffman, A. J.; Yee, H.; Mills, G.; Yee, H.; Hoffmann, M. R. *J. Phys. Chem.***1992**, *96*, 5546
5) Pattabi, M.; Uchil, J. *Sol. Energy Mater. Sol. Cells* **2000**, *63*, 309.
6) Berr, M.; Vaneski, A.; Susha, A. S.; Rodríguez-Fernández, J.; Döblinger, M.; Jäckel, F.; Rogach, A. L.; Feldmann, J. *Appl. Phys. Lett.* **2010**, *97*, 093108.
7) Li, Y.; Du, J.; Peng, S.; Xie, D.; Lu, G.; Li, S. *Int. J. Hydrogen Energy* **2008**, *33*, 2007.
8) Amirav, L.; Alivisatos, A. P. *J. Phys. Chem. Lett.* **2010**, *1*, 1051.
9) Li, Y. X.; Xie, Y. Z.; Peng, S. Q.; Lu, G. X.; Li, S. B. *Chemosphere* **2006**, 63, 1312
10) Yan, H. J.; Yang, J. H.; Ma, G. J.; Wu, G. P.; Zong, X.; Lei, Z. B.; Shi, J. Y.; Li, C. *J. Catal.* **2009**, *266*, 165
11) Wang, X.; Liu, G.; Lu, G. Q.; Cheng, H. M. *Int. J. Hydrogen Energy* **2010**, *35*, 8199.
12) Shangguan, W. F.; Yoshida, A. *J. Phys. Chem. B* **2002**, *106*, 12227
13) Park, H.; Choi, W.; Hoffmann, M. R. *J. Mater. Chem.* **2008**, *18*, 2379.
14) Wang, Y. B.; Wu, J. C.; Zheng, J. W.; Xu, R. *Catal. Sci. Technol.* **2011**, *1*, 940.
15) Becheri, A.; Dürr, M.; Nostro, P. L.; Baglioni, P. *J. Nanopart. Res.* **2008**, *10*, 679.
16) Konzinger H, Ratnasamy P. *Catal Rev Sci Eng* 1978, *17*, 31.
17) Matsumura, M.; Furukawa, S.; Saho, Y.; Tsubomura, H. *J. Phys. Chem.* **1985**, *89*, 1327.
18) Fujii, M.; Kawai, T.; Kawai, S. *Chem. Phys. Lett.* **1984**, *106*, 517.
19) Sing, K. S.W.; Everett, D. H.; Haul, R.; Moscou, L.; Pierotti, R. A.; Rouquerol, J.; Siemieniewska, T. *Pure Appl. Chem.* **1985**, *57*, 603.
20) Chen, X.; Shen, S.; Guo, L.; Mao, S. S. *Chem. Rev.* **2010**, *110*, 6503.

21) Liu, H.; Zhang, K.; Jing, D.; Liu, G.; Guo, L. *Int. J. Hydrogen Energy* **2010**, *35*, 7080.

22) Parida, K. M.; Biswal, N.; Das, D. P.; Martha, S. *Int. J. Hydrogen Energy* **2010**, *35*, 5262.

23) Li, Q.; Guo, B.; Yu, J.; Ran, J.; Zhang, B.; Yan, H.; Gong, J. R. *J. Am. Chem. Soc.* **2011**, *133*, 10878.

24) Chen, Y.; Wang, L.; Lu, G. (Max); Yao, X.; Guo, L. *J. Mater. Chem.* **2011**, *21*, 5134.

25) Choi, J.; Ryu, S. Y.; Balcerski, W.; Lee, T. K.; Hoffmann, M. R. *J. Mater. Chem.* **2008**, *18*, 2371.

26) Wang, X.; Liu, G.; Chen, Z.-G.; Li, F.; Wang, L.; Lu, G. Q.; Cheng, H.-M. *Chem. Commun.* **2009**, 3452.

27) Li, X.; Wang, D.; Cheng, G.; Luo, Q.; An, J.; Wang, Y. *Appl. Catal. B: Enviorn.* **2008**, *81*, 267.

28) Zhang, H.; Wu, P.; Li, Y.; Liao, L.; Fang, Z.; Zhong, X. *ChemCatChem* **2010**, 2, 1115.

29) Tak, Y.; Kim, H.; Lee, D.; Yong, K. *Chem. Commun.* **2008**, 4585.

30) Konstantinou, I. K.; Albanis, T. A. *Appl. Catal.,B: Enviorn.* **2004**, *49*, 1.

31) Rauf, M. A.; Ashraf, S. S. *Chemical Engineering Journal* **2009**, *151*, 10.

Chapter 3

Part B

Hierarchical 3D NiO/CdS Heteroarchitecture for Efficient Visible Light Photocatalytic Hydrogen Generation

This chapter describes the effect of enhanced specific surface area and facile charge transfer on the photocatalytic activity. As prepared 3D NiO/CdS show high efficiency for photocatalytic hydrogen generation with an apparent quantum yield (AQY) of 6% in comparison to that of 1D CdS nanowires and bulk CdS under visible light irradiation. The superior hydrogen production rate in 3D NiO/CdS is attributed to the enhanced specific surface area and facile charge transfer from the conduction band of CdS to conduction band of NiO due to the favorable band alignments.

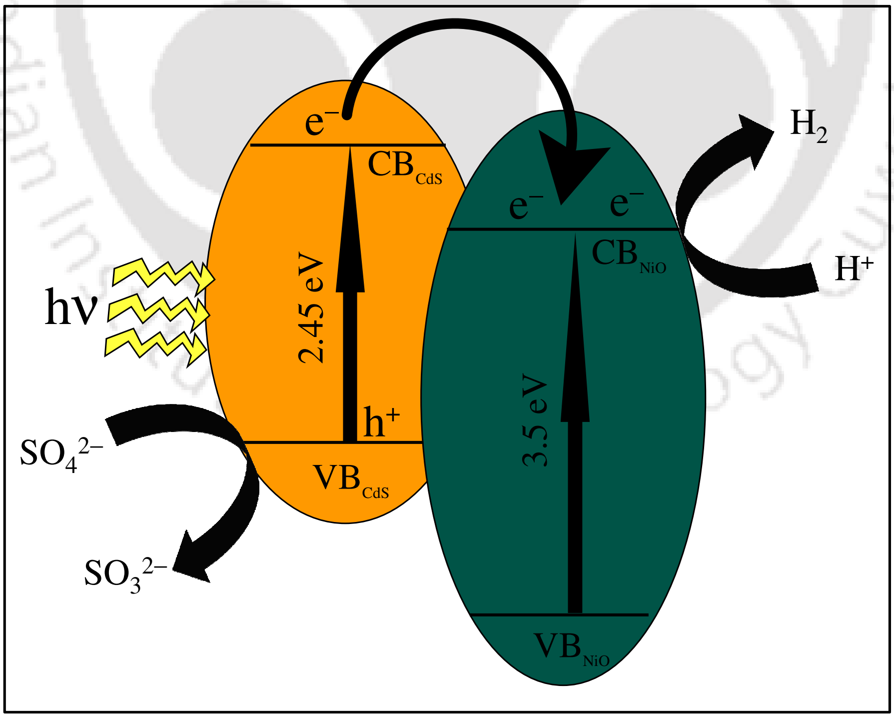

J. Mater. Chem. **2012**, *DOI: 10.1039/c2jm31148h*

3B.1. Introduction

Cadmium Sulfide (CdS) is the most extensively used photocatalyst for hydrogen generation by water splitting due to its robust activity under visible light (2.48 eV) and sufficiently negative flat-band potential.[1,2] However, for the practical applications, the photocatalytic activity of CdS is low, due to its photocorrosion property, relatively less specific surface area and a high recombination rate of photogenerated electrons and holes. One of the alternates chosen were CdS based one dimensional (1D) semiconductor nanostructure materials such as nanorods, nanowires (NWs), nanotubes and nanobelts[3-6] which showed the capability to enhance the photocatalytic efficiency via promoting the electron transfer.[7] It was also known that the efficient transfers of photo-induced electrons and holes from CdS to the reactants can reduce the photocorrosion of CdS to a greater extent, by improving the stability of CdS for long term applications.[8,9] For example, Hotchandani and Kamat demonstrated that colloidal CdS-ZnO showed extended photo-response into the visible region and facilitate better charge separation, enhancing the stability of CdS thereby enabling its application in photoelectrochemical cells.[9] Wang *et al.* also demonstrated that ZnO/CdS catalyst showed good stability and excellent efficiency for photocatalytic H_2 generation.[10]

In this chapter we have demonstrated the photocatalytic hydrogen generation by water splitting from novel hierarchical 3D NiO/CdS binary heteroarchitecture synthesized by a simple hydrothermal route. The selection of NiO (wide band gap semiconductor) is based on its band alignment with CdS; wherein, the conduction band (CB) of CdS (–0.88 eV, pH 0)[8] is in the proximity to the CB of NiO (0.0 eV, pH 0)[11] which can facilitate efficient charge transfer from the CB of CdS to the CB of NiO, thereby reducing the recombination rate of photo-induced electron and hole pair, making it more active photocatalyst without use of any co-catalyst.

3B.2. Experimental Section

3B.2.1. Synthesis of Novel Hierarchical 3D NiO/CdS Binary Heteroarchitecture

Hierarchical 3D NiO/CdS binary heteroarchitecture was synthesized by single-pot hydrothermal route similar to the method as discussed in the experimental section of Chapter 2 section 2.3.6. In a typical synthesis, $NiCl_2.6H_2O$ (3.9 mmol) was dissolved in 15 mL distilled water followed by the addition of aq. NH_3 under vigorous stirring. After the addition of $Cd(CH_3COO)_2.2H_2O$ (9.0 mmol) and thioglycolic acid (9.0 mmol), reaction mixture was stirred at room temperature for 30 min. The resultant suspension was transferred to a Teflon-lined stainless steel autoclave, and kept in an electronic oven at different condition shown in Table 3B.1. After cooling down to room temperature, the solution obtained was centrifuged and the solid product was washed with water and ethanol to remove the excess of metal ions and thioglycolic acid, if any. After drying at 70 °C for 5 h in an oven under atmospheric condition, the samples were ready for further characterizations and photocatalytic experiments.

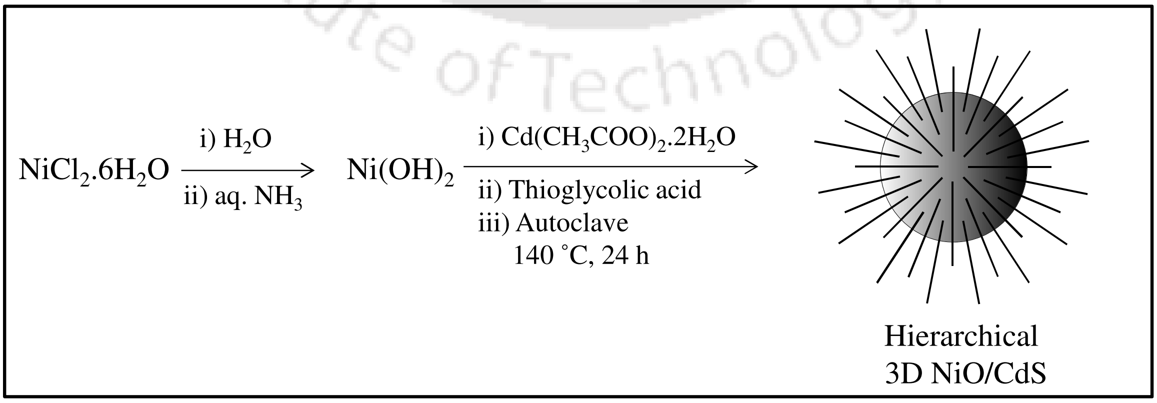

Table 3B.1 Products at different reaction condition for the synthesis of hierarchical 3D NiO/CdS

Temperature and Time	pH	Morphology of NiO/CdS	Remarks
140 ˚C, 48 h	7	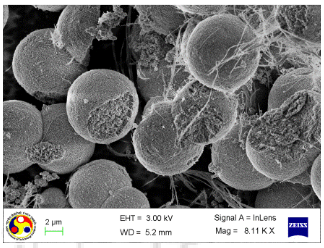	Porous Structured Material
140 ˚C, 48 h	10	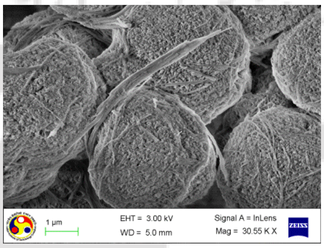	Porous Structured Material
140 ˚C, 48 h	12	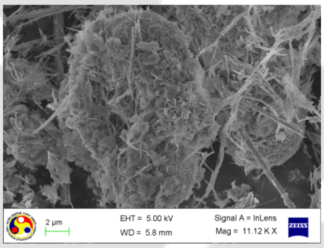	Flower like Structure
140 ˚C, 24 h	7	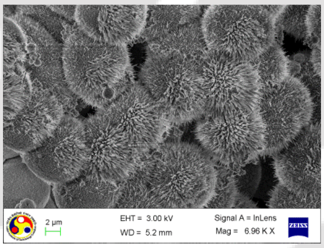	Heirarchical Structure

3B.3. Results and Discussion

3B.3.1. Materials Morphology

The morphologies of as-prepared NiO/CdS at different reaction conditions were examined by Field Emission - Scanning Electron Microscopy (FE-SEM). Figure 3B.1a-c reveals the formation of porous spherical particle of NiO/CdS prepared at pH 7 for 48 h. Figure 3B.1d-f depicts the formation of spherical particle of NiO/CdS prepared at pH 10 for 48 h.

NiO/CdS were also prepared at pH 12 for 48 h which are not hierarchical in nature, as confirmed by FE-SEM (Figure 3B.1g-i).

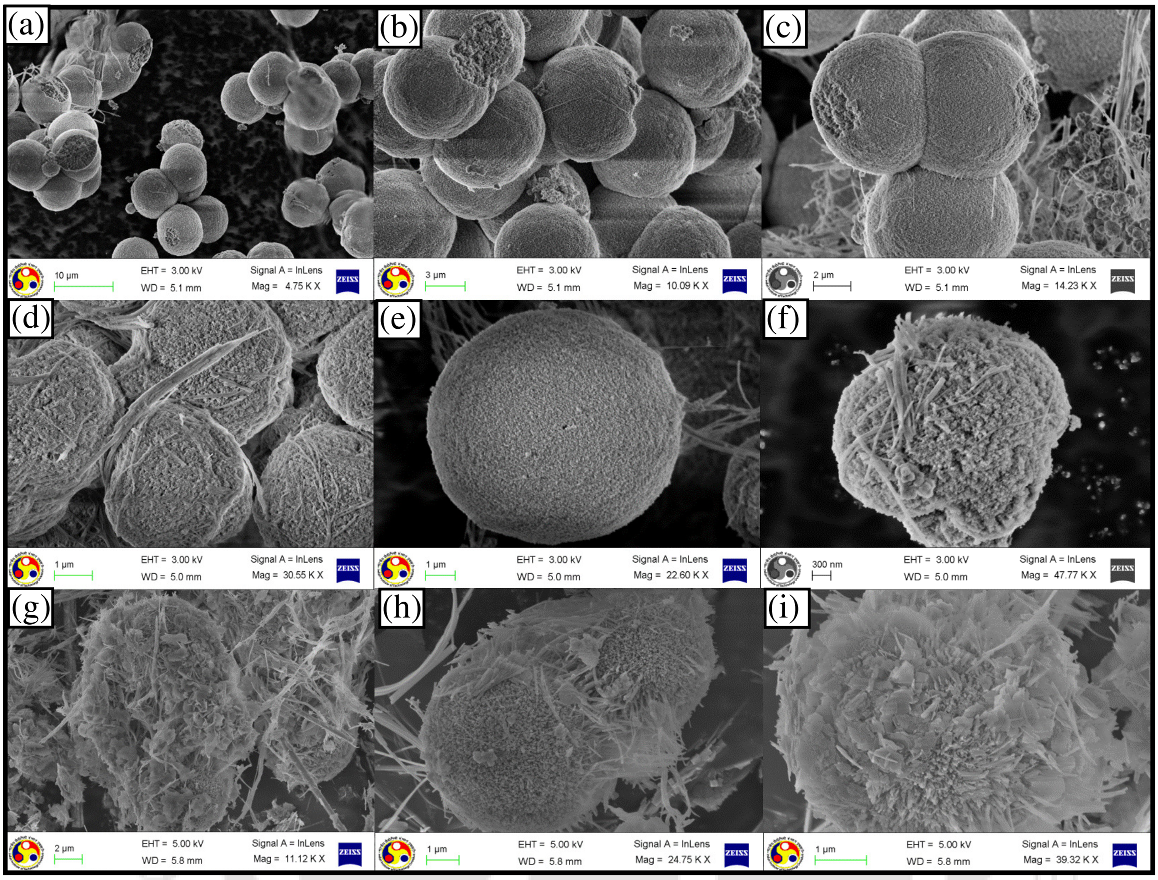

Figure 3B.1 Field Emission-Scanning Electron Microscopic images of the as-prepared NiO/CdS (a-c) at pH 7, (d-f) at pH 10 and (g-i) at pH 12 at 140 ˚C for 48 h. FE-SEM reveals the formation of porous structure not the hierarchical structure of NiO/CdS

The morphology of the as-prepared NiO/CdS (at pH 7 for 24 h) was examined by FE-SEM and TEM images shown in Figure 3B.2 and Figure 3B.3. Figure 3B.2a–c represents the FE-SEM images of as-prepared NiO/CdS structure in which Figure 3B.2a is low magnification image while Figure 3B.2b & c are the relatively high magnification image. FE-SEM images (Figure 3B.2) of the obtained material showed the formation of three dimensional (3D) hierarchical heteroarchitecture. Figure 3B.2b shows FE-SEM image of sample in which slightly aggregated microsphere with the size around *ca.* 1 µm can be observed. The hierarchical 3D heteroarchitecture (Figure 3B.2b-c) demonstrate that the microsphere is assembled from many 1D CdS NWs (~50 nm diameter and 200 nm of length) which are orderly aligned and radially oriented on NiO NPs, thereby giving flower like morphology. Figure 3B.2d shows energy dispersive X-ray (EDX) pattern for hierarchical 3D NiO/CdS which confirmed the presence of Cd, Ni, O and S elements. The quantitative analysis of the EDX reveals that the atomic ratio of Cd^{2+}: Ni^{2+} is about 1: 0.32 which is in fair agreement with the atomic ratio of the same taken during the synthesis of hierarchical 3D NiO/CdS.

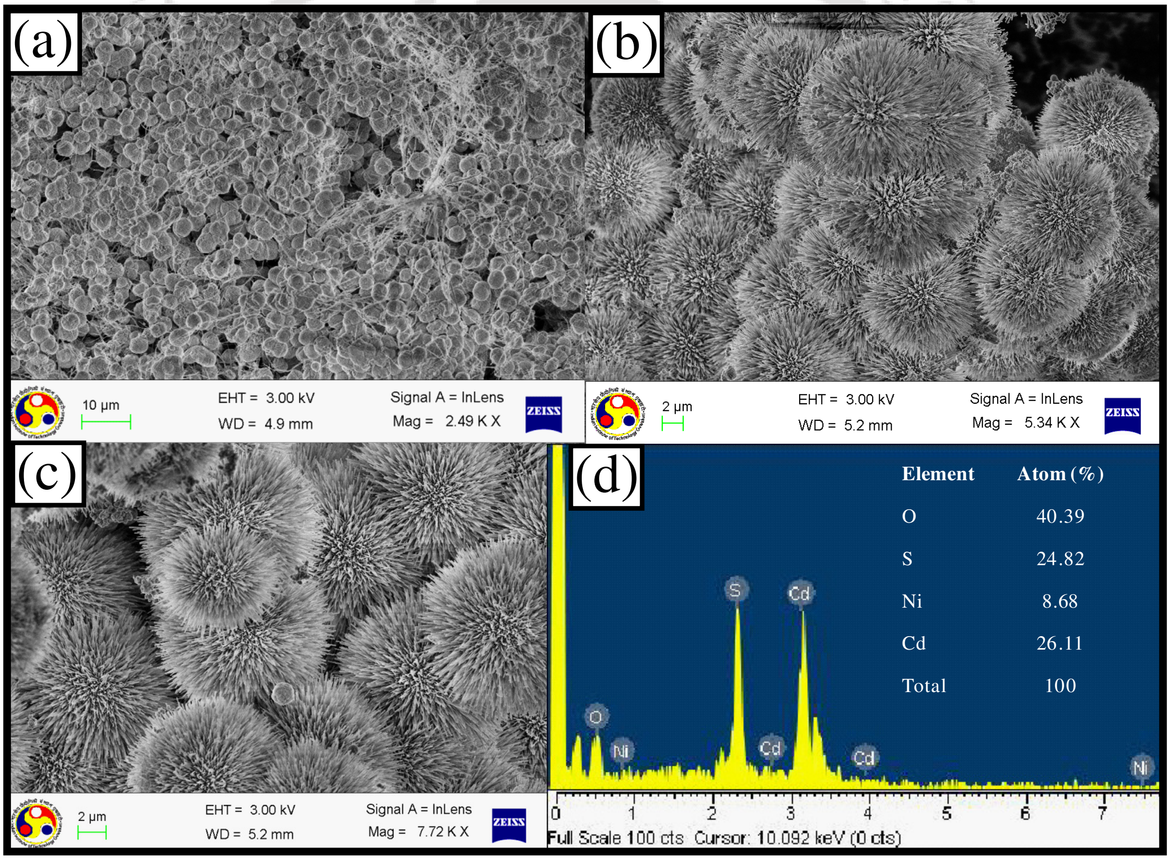

Element	Atom (%)
O	40.39
S	24.82
Ni	8.68
Cd	26.11
Total	100

Figure 3B.2 (a-c) FE-SEM images of the as-prepared NiO/CdS at pH 7 for 24 h. FE-SEM images confirms the formation of hierarchical 3D NiO/CdS, (d) EDX pattern with quantitative atomic ratio of hierarchical 3D NiO/CdS

Figure 3B.3a-b show TEM images of single NiO/CdS microsphere, which further reveals that these 3D NiO/CdS microsphere are assembled from 1D CdS NWs. It should be noted that there is a contradiction in the size of hierarchical 3D NiO/CdS between FE-SEM and TEM images because at low magnification the TEM images appeared as dark patches which are not useful. Hence, in order to obtain informative image of sample, TEM image was taken for the particle having smaller size (the sample was prepared from the supernatant of the NiO/CdS dispersion).

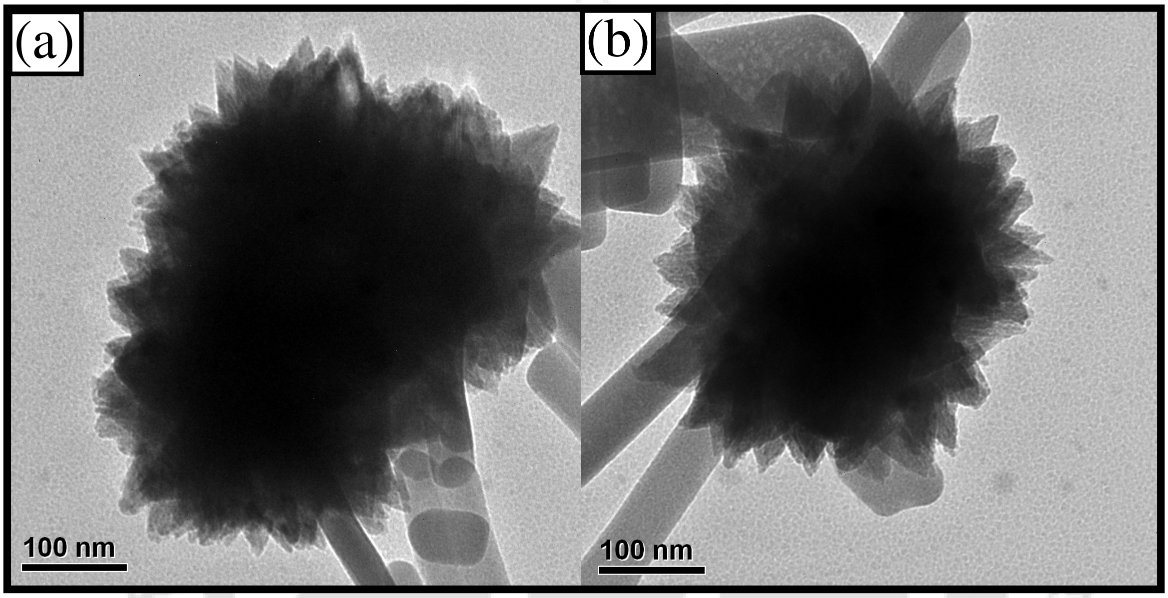

Figure 3B.3 Transmission Electron Microscopic images depicts the formation of hierarchical 3D structure of NiO/CdS

3B.3.2. Mechanism for the Formation of Hierarchical 3D NiO/CdS Binary Heteroarchitecture

In chapter 3A, we have demonstrated the directed growth of 1D CdS NWs on Al_2O_3 and ZnO nanoparticles. Based on that discussion we proposed a mechanism for the formation of hierarchical 3D NiO/CdS heteroarchitecture. The graphic presentation for the formation of 3D NiO/CdS is shown in scheme 3B.1. The growth mechanism of CdS on

NiO can be explained on the basis of Lewis acidic character of Ni^{2+}. The growth mechanism may follow these steps:

i) Formation of NiO NPs in hydrothermal condition.

ii) Attachment of S^{2-} to NiO nanoparticles because of the Lewis acidic nature of Ni^{2+} in the solution.

iii) Cd^{2+} ion is also present in the solution which encourages the formation of CdS nanoparticles at high temperature and pressure.

iv) Saturated CdS may act as seed for the formation and growth of CdS NWs onto NiO NPs in hydrothermal condition, thereby leading the formation of hierarchical 3D NiO/CdS heteroarchitecture.

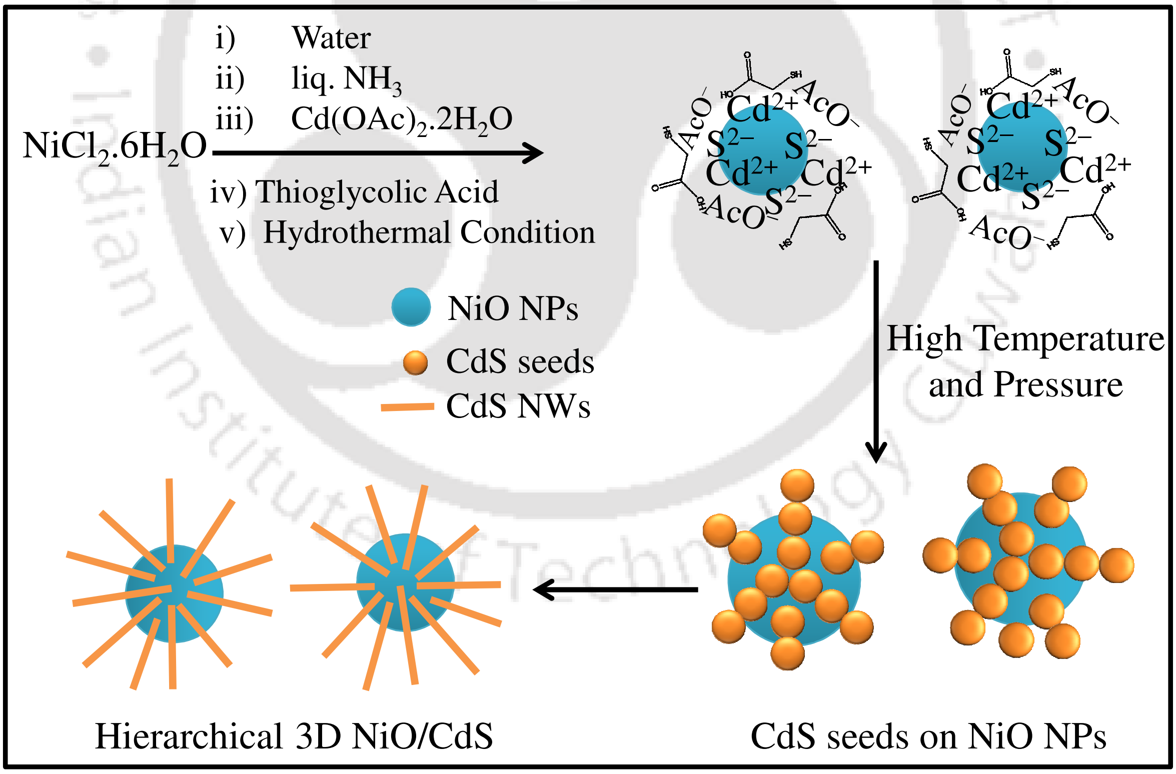

Scheme 3B.1 Schematic representation for the formation of hierarchical 3D NiO/CdS heteroarchitecture

Formation of hierarchical 3D NiO/CdS heteroarchitecture was further confirmed by scanning electron microscope (SEM) images as shown in Figure 3B.4.

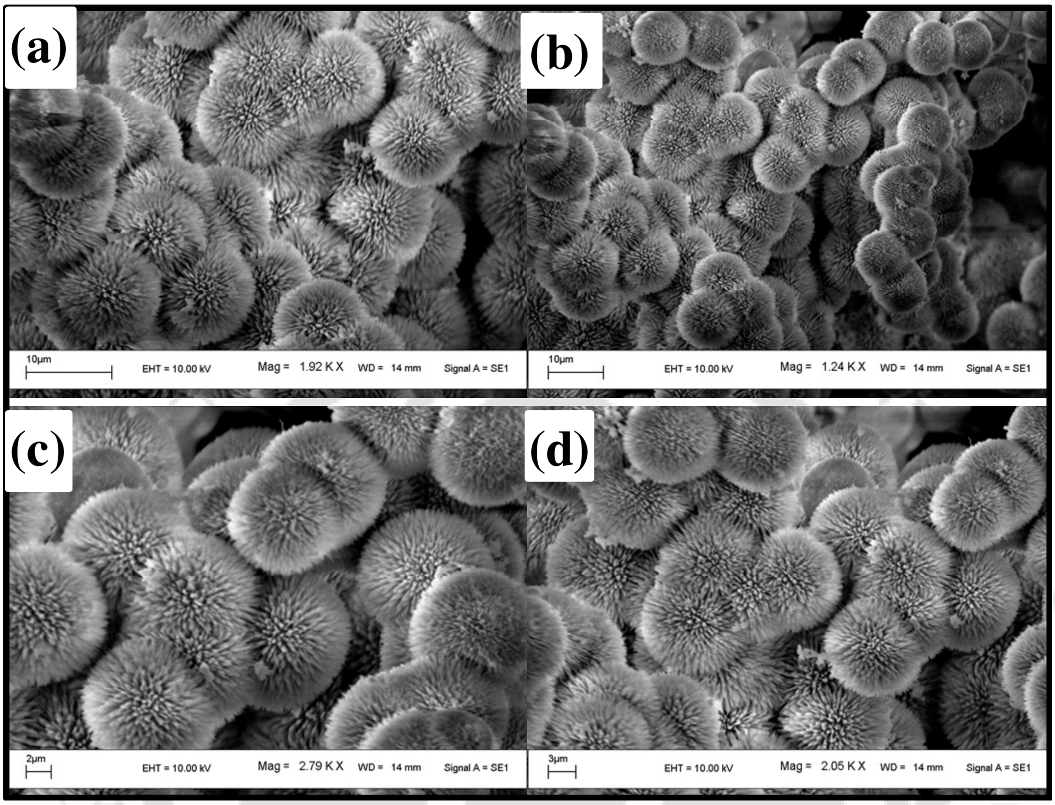

Figure 3B.4 Scanning Electron Microscopic images of hierarchical 3D NiO/CdS heteroarchitecture at different magnifications

3B.3.3. Powder X-ray Diffractogram

The purity and crystalline phase of the hydrothermally synthesized 1D CdS NWs and the hierarchical 3D NiO/CdS binary heteroarchitecture were analyzed by powder X-ray diffractogram. PXRD patterns for 1D CdS NWs, NiO NPs and hierarchical 3D NiO/CdS is shown in Figure 3B.5. From XRD it is clear that the hydrothermally synthesized 1D CdS NWs were crystallized into a standard hexagonal structure (JCPDS 06-0314) while NiO NPs were crystallized into cubic structure (JCPDS 47-1049) with all planes indexed. No diffraction peaks from the other crystalline forms of CdS or NiO were detected in both the diffractograms. In 3D NiO/CdS diffractogram, distinct lattice planes corresponding to the NiO NPs and 1D CdS NWs were revealed the presence of individual components of NiO and CdS. It is interesting to note that the crystalline phase of 1D CdS NWs is retained even after it is grown onto the NiO NPs. The unit cell parameter calculation for these samples were also carried out and compared with the above mentioned referenced cards which are given in Table 3B.2.

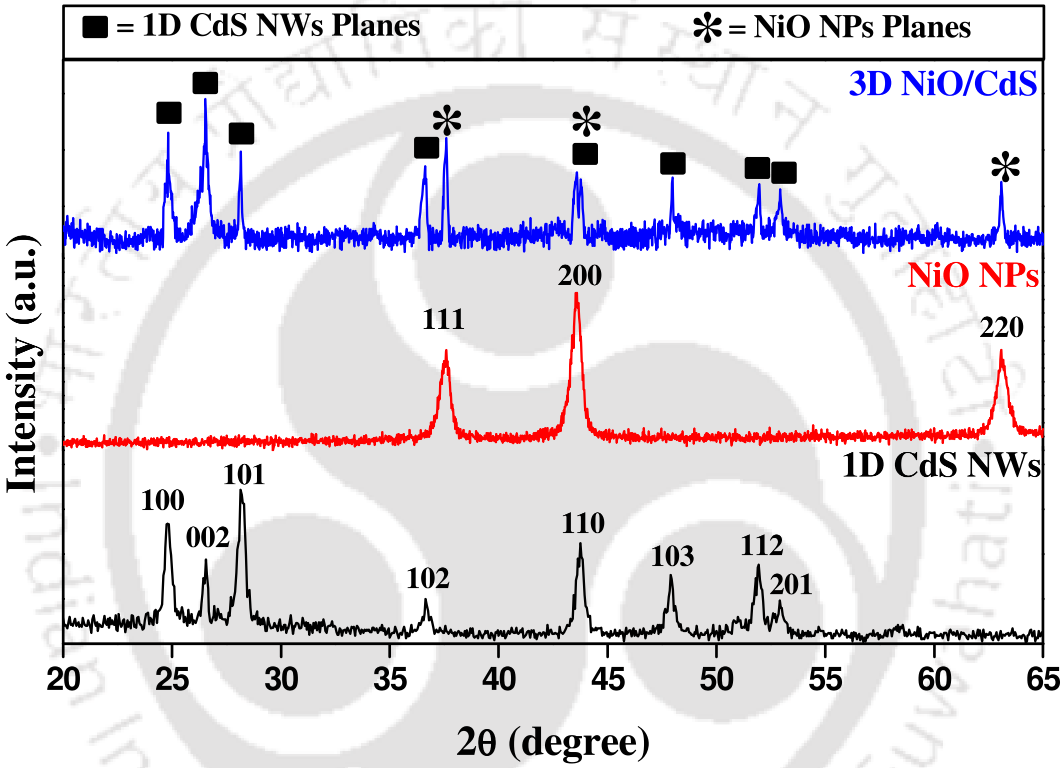

Figure 3B.5 Powder X-ray diffraction patterns for 1D CdS NWs, NiO NPs and hierarchical 3D NiO/CdS heteroarchitecture. The crystalline phase of 1D CdS NWs is retained even after grown onto NiO NPs

Table 3B.2 Comparison of unit cell parameters with the reported referenced card (JCPDS 06-0314 and JCPDS 47-1049)

Samples	Unit Cell Parameters (Calculated)	Unit Cell Parameters (Reported)
CdS NWs	a = 0.3925 nm & c = 0.6710 nm	a = 0.4136 nm & c = 0.6713 nm
NiO NPs	a = 0.4149 nm	a = 0.4177 nm
CdS in 3D NiO/CdS	a = 0.3984 nm & c = 0.6708	a = 0.4136 nm & c = 0.6713 nm
NiO in 3D NiO/CdS	a = 0.4157 nm	a = 0.4177 nm

3B.3.4. UV-Vis Diffuse Reflectance Spectra

UV-Vis diffuse reflectance spectra of 1D CdS NWs, NiO NPs and 3D NiO/CdS are shown in Figure 3B.6. The absorption spectra were recorded in the wavelength range of 250–650 nm. Interestingly, all these materials show almost the same absorption profile with a steep absorption edge in UV and visible range, which corresponds to the band gap energy for the individual components.

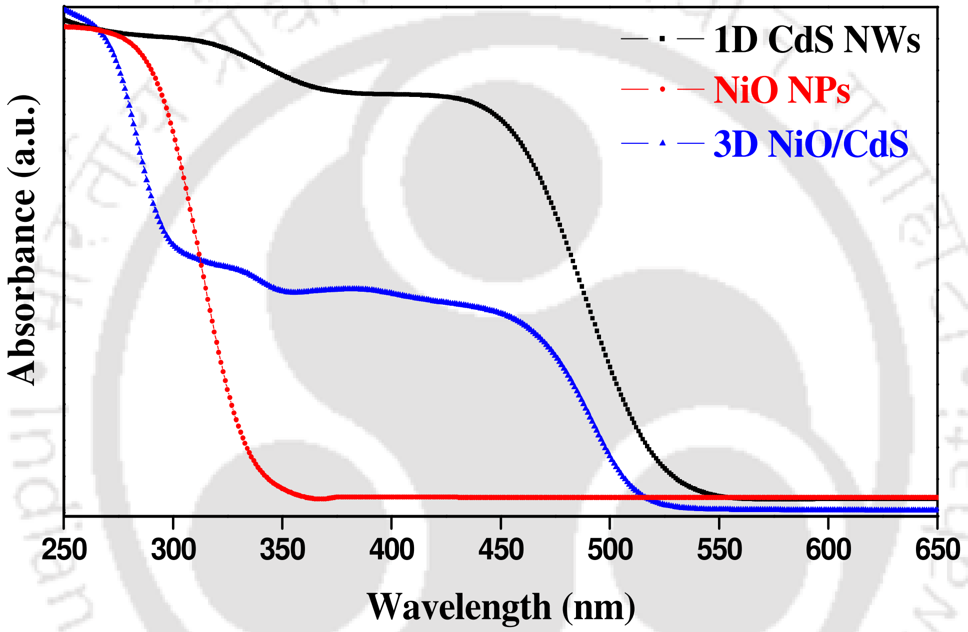

Figure 3B.6 UV-Vis diffuse reflectance spectra for 1D CdS NWs, NiO NPs, and hierarchical 3D NiO/CdS heteroarchitecture

From absorption spectra one can clearly observe that hierarchical 3D NiO/CdS shows two absorption steeps at *ca.* 3.6 eV and *ca.* 2.4 eV corresponding to the NiO and CdS respectively. No additional peak was observed in the absorption profile of 3D NiO/CdS photocatalyst. The optical band gap for all these photocatalyst can be calculated by Tauc's plot which is described as

$$(\alpha h\nu)^{1/n} = \mathrm{C}\times(h\nu - E_g),$$

where α is the absorption coefficient, λ is wavelength, h is Planck's constant, C is the proportionality constant, ν is the frequency of light, E_g is the band gap energy and n = ½ and 2 for direct and indirect band gap materials, respectively. The absorption coefficient is defined by the following equation

$$\alpha = -\frac{1}{t} \times \ln\left(\frac{I_t}{I_0}\right) = \frac{1}{t} \times A \times \log e,$$

where, A and t represent the absorbance and thickness of the photocatalyst film; I_t, and I_0 signify intensity of transmitted and incident light, respectively.

From Figure 3B.7, where $(\alpha h\nu)^2$ is plotted against the photon energy $(h\nu)$, the band gap energies for 1D CdS NWs, NiO NPs and hierarchical 3D NiO/CdS are predicted from extrapolated lines. From the Tauc's plot the calculated band gaps are found to be 2.45 eV for 1D CdS NWs, 3.35 eV for NiO NPs and 2.5 eV for 3D NiO/CdS.

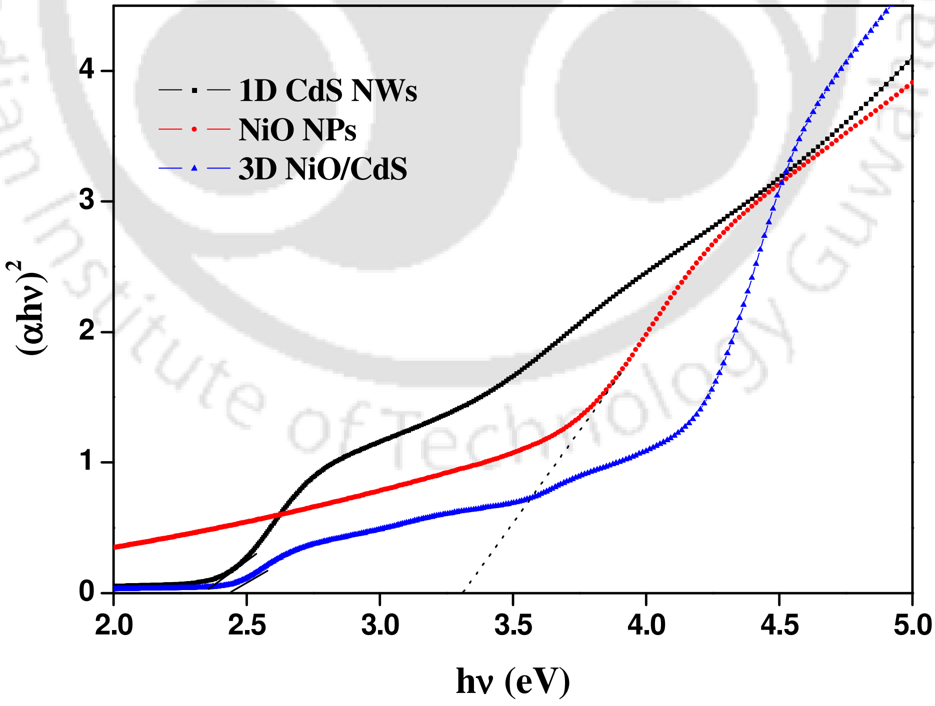

Figure 3B.7 Tauc's plot of $(\alpha h\nu)^2$ versus photon energy $(h\nu)$ for the optical band gap calculation for 1D CdS NWs, NiO NPs, and 3D NiO/CdS heteroarchitecture

3B.3.5. BET Surface Area Analyses

The N_2 adsorption-desorption isotherms of the hierarchical 3D NiO/CdS heteroarchitecture along with 1D CdS NWs were measured as shown in Figure 3B.8. According to the Brunauer-Deming-Deming-Teller (BDDT) classification, the majority of physisorption isotherms can be grouped into six types.[12]

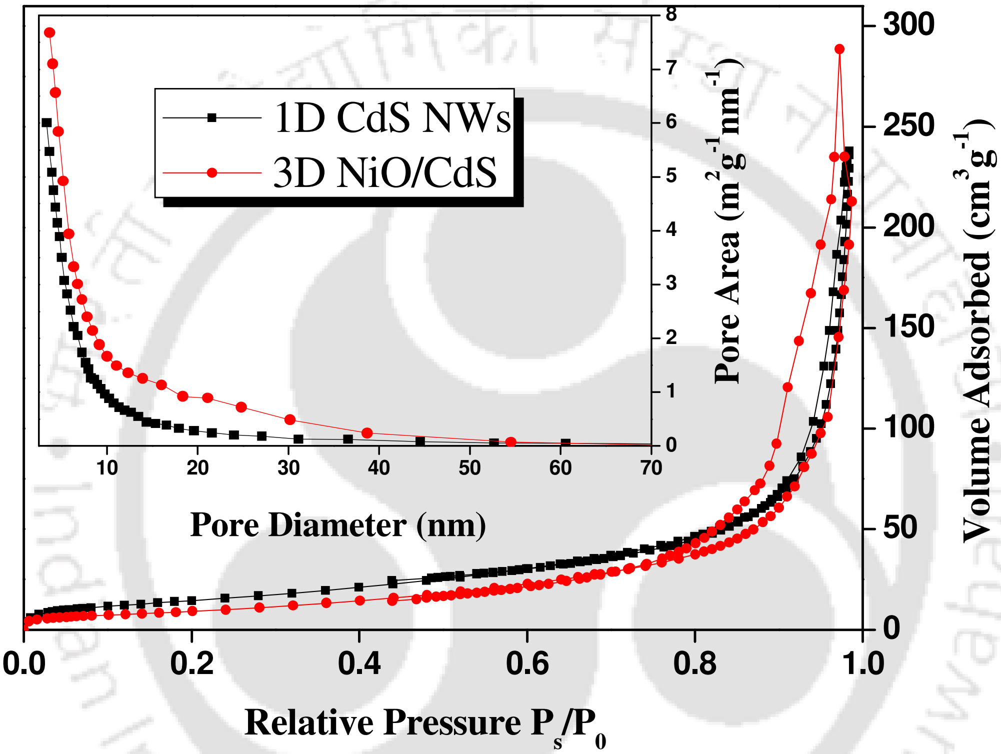

Figure 3B.8 Nitrogen adsorption-desorption isotherms and the pore size distribution plots for 1D CdS NWs and hierarchical 3D NiO/CdS heteroarchitecture. Inset shows the plot of pore area versus pore diameter (BJH plot for pore size distribution)

Both the samples in the present study follow typical type-IV isotherms and type H3 hysteresis loops, which are the characteristic feature of mesopores. Therefore, hierarchical 3D NiO/CdS is a porous material favourable for mass transfer. As being measured, the hierarchical 3D NiO/CdS flower like heteroarchitecture enhances the BET surface area (44 m^2/g) greatly in contrast to that of CdS NWs (15 m^2/g) and the CdS bulk (3 m^2/g). The Barret-Joyner-Halenda (BJH) pore size distribution was similar in character (inset Figure

3B.8) for 1D CdS NWs and hierarchical 3D NiO/CdS. Therefore, we can say that the surface morphology of CdS NWs remains same even after its growth on NiO NPs.

3B.3.6. Photocatalytic Hydrogen Evaluation

In order to evaluate the H_2 generation ability of the synthesized hierarchical 3D NiO/CdS, photocatalytic water splitting experiments were carried out. Water splitting experiment were also conducted using bulk CdS and 1D CdS NWs to have a relative study of H_2 production efficacy with that of 3D NiO/CdS. The H_2 evolution rates under visible irradiation and specific surface area of bulk CdS, 1D CdS NWs and hierarchical 3D NiO/CdS are shown below in Figure 3B.9.

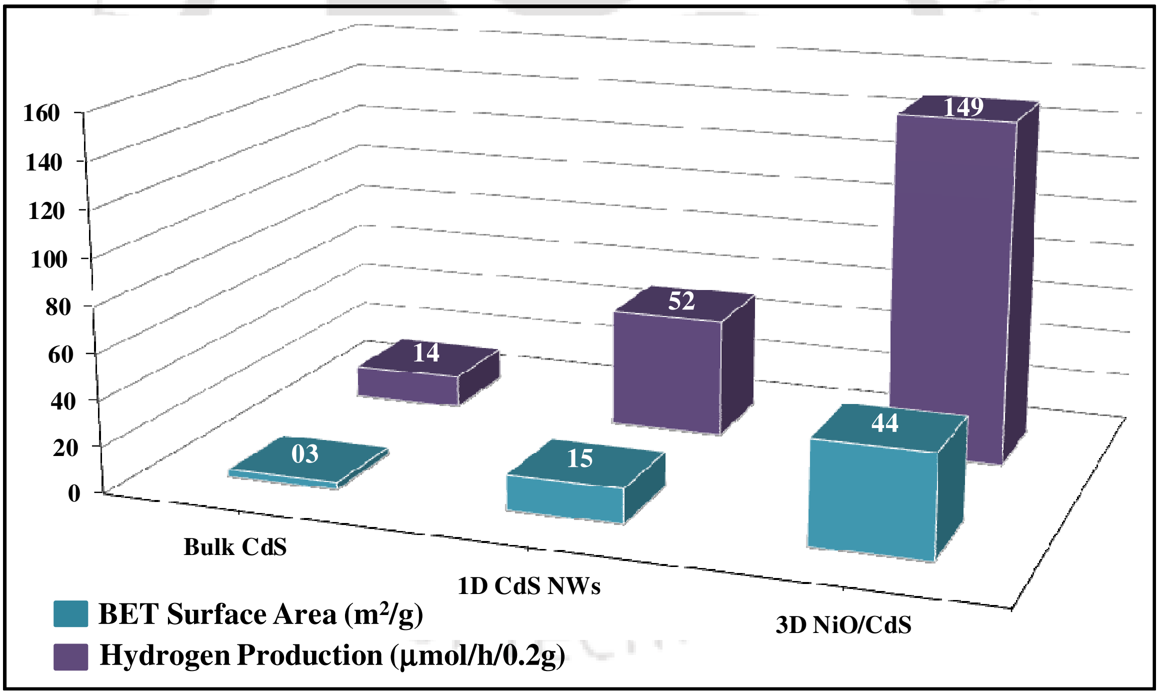

Figure 3B.9 Specific surface area and amount of H_2 generation from CdS bulk, 1D CdS NWs, and 3D NiO/CdS photocatalysts under visible light irradiation

From Figure 3B.9, it can be clearly seen that 3D NiO/CdS is having greater photocatalytic activity with highest H_2 production rate of 149 µmol/h; in comparison to bulk CdS (14 µmol/h) and 1D CdS NWs (52 µmol/h). The superior photocatalytic activity could be attributed to the enhanced specific surface area, improved charge separation and crystalline phase of CdS in the as-synthesized 3D NiO/CdS. Based on the reports present in the literature,[9,13-15] we proposed a mechanism for efficient charge transfer between CdS and NiO. To explain the mechanism of photocatalytic H_2 generation by the hierarchical 3D NiO/CdS, a schematic illustration of the efficient electron transfer along with the band positions of CdS and NiO in the flower like heteroarchitecture, is shown in Scheme 3B.2.

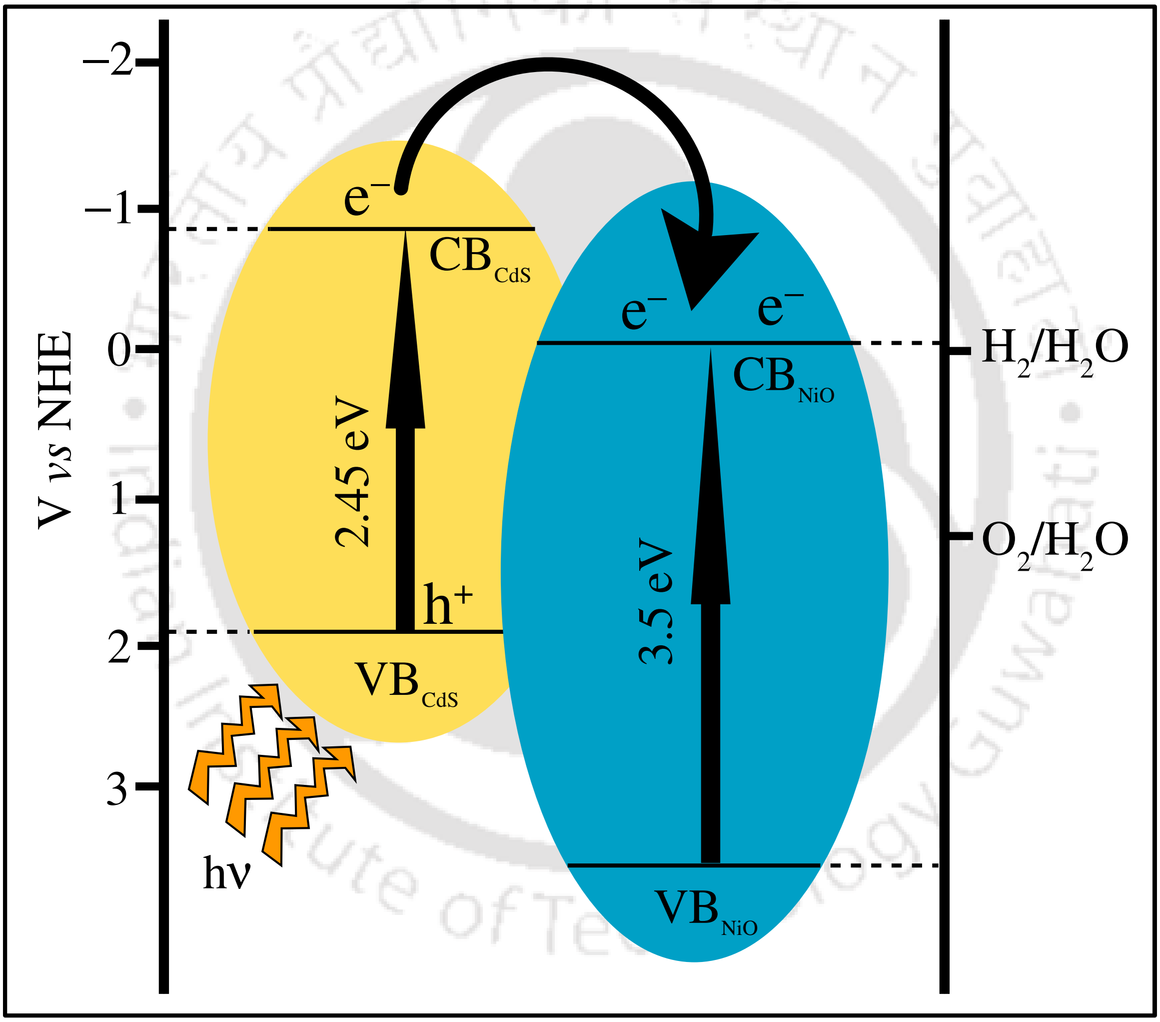

Scheme 3B.2 Schematic illustration of the efficient electron transfer and the band energy positions of NiO and CdS in the hierarchical 3D NiO/CdS binary heteroarchitecture. The effective transfer of reductive electron from CdS CB to NiO CB makes 3D NiO/CdS efficient photocatalyst for hydrogen generation under visible light irradiation

Irradiation of visible light on 3D NiO/CdS, CdS itself goes into the photo-excited state by creating reductive electrons and oxidative holes in the CB and VB respectively. No charges are generated in NiO because it is a wide band gap semiconductor. The sacrificial electron donor (Na_2SO_3) rapidly consumes oxidative holes in the VB of CdS leaving reductive electrons in the CB. Reductive electrons were also separated by transferring from CB of CdS to CB of NiO because of the close alignment of conduction band thereby leading reduction in the recombination rate of photoinduced electron hole pairs. The pool of reductive electrons thus generated in the CB of NiO causes the reduction of H^+ ions and thereby producing H_2 gas. The other reason for superior hydrogen production is that enhanced surface area for 3D NiO/CdS which is convenient for mass transfer, along with that the factor which could possibly be another reason for the efficient H_2 production is the hexagonal phase of CdS in the 3D NiO/CdS as reported by Matsumura *et al.*[1] The apparent quantum yield for the photocatalyst 3D NiO/CdS was also calculated and found to be 6% which was three fold higher than that of the 1D CdS NWs whose AQY was around 2%.

The advantage of hierarchical 3D NiO/CdS photocatalyst is the enhanced hydrogen production rate without addition of any noble metal co-catalyst such as Pt, Pd, Ru, Rh etc, which makes photocatalytic process inexpensive. Co-catalyst has low band positions due to which the addition of any co-catalyst assists effectual charge separation of electron and holes thereby making the photocatalytic process more efficient. Based on this idea, hierarchical 3D NiO/CdS binary heteroarchitecture has been synthesized which has been proven as an efficient photocatalyst. From Table 3B.3, it can be clearly observed that hierarchical 3D NiO/CdS heteroarchitecture shows higher efficiency than most of the previously reported CdS based photocatalysts from the literature.

Table 3B.3 Apparent quantum yield values of CdS based photocatalysts for hydrogen generation under the irradiation of visible light

Photocatalyst	Synthetic method	co-catalyst	AQY* (%)	ref
Pt/CdS NWs	chemical deposition	-	3.9	16
$Mn_{1-x}Cd_xS$	hydrothermal	RuO	7	17
SrS/CdS	precipitation	Pt	5.83	18
CdS/ ZTP	-	-	5.84	19
CdS/Graphene	solvothermal	Pt	22.5	20
CdS/MWCNT	hydrothermal	-	2.16	6
CdS/Ti-MCM-41	ion exchange, sulfurization	Pt	2.6	21
Ni/NiO/$KNbO_3$/CdS	-	-	4.4	22
CdS-ZnS	-	-	0.60	23
CdS	impregnation method	0.2 wt% MoS_2	7.3	24, 25
NiO/TiO_2	-	-	0.32	26
TiO_2/NiO	sol-gel	-	-	27
3D NiO/CdS	hydrothermal	-	6.02	Present work

* The value of AQY varies with the evaluation method and the system of interest.

3B.4. Conclusion

1- We have demonstrated a simple one pot synthesis of NiO/CdS, which are hierarchical 3D in nature with an average diameter of 300 nm characterized by TEM, FE-SEM and SEM.

2- Hierarchical 3D NiO/CdS heteroarchitecture act as an efficient visible light driven photocatalyst for hydrogen generation by water reduction having apparent quantum yield up to 6%.

3- The high hydrogen production rate of hierarchical 3D NiO/CdS is mainly attributed to the enhanced specific surface area, facile charge transfer form CdS conduction band to NiO conduction band and crystalline phase of CdS NWs.

4- Present approach offers a viable route to synthesize a variety of visible light driven heteroarchitecture for photocatalytic hydrogen production in future.

References

1) Matsumura, M.; Furukawa, S.; Saho, Y.; Tsubomura, H. *J. Phys. Chem.* **1985**, *89*, 1327.

2) Reber, J. F.; Meier, K. *J. Phys. Chem.* **1986**, *90*, 824.

3) Berr, M.; Vaneski, A.; Susha, A. S.; Rodríguez-Fernández, J.; Döblinger, M.; Jäckel, F. ; Rogach, A. L.; Feldmann, J. *Appl. Phys. Lett.* **2010**, *97*, 093108.

4) Li, Y.; Du, J.; Peng, S.; Xie, D.; Lu, G; Li, S. *Int. J. Hydrogen Energy* **2008**, *33*, 2007.

5) Amirav, L.; Alivisatos, A. P. *J. Phys. Chem. Lett.* **2010**, *1*, 1051.

6) Chen, Y.; Wang, L.; Lu, G. (Max); Yao, X.; Guo, L. *J. Mater. Chem.* **2011**, *21*, 5134.

7) Liu, Z.; Sun, D. D.; Guo, P.; Leckie, J. O. *Nano Lett.* **2007**, *7*, 1081.

8) Kudo, A.; Miseki, Y. *Chem. Soc. Rev.* **2009**, *38*, 253.

9) Hotchandani, S.; Kamat, P. V. *J. Phys. Chem.* **1992**, *96*, 6834.

10) Wang, X.; Liu, G.; Lu, G. Q.; Cheng, H. M. *Int. J. Hydrogen Energy* **2010**, *35*, 8199.

11) Xu, Y.; Schoonen, M. A. A. *Amer. Mineral.* **2000**, *85*, 543.

12) Sing, K. S. W.; Everett, D. H.; Haul, R.; Moscou, L.; Pierotti, R. A.; Rouquerol, J.; Siemieniewska, T. *Pure Appl. Chem.* **1985**, *57*, 603.

13) Zou, Z.; Ye, J.; Arakawa, H. *Chem. Mater.* **2001**, *13*, 1765.

14) Liu, Z.; Bai, H.; Xu, S.; Sun, D. D. *Int. J. Hydrogen Energy* **2011**, *36*, 13473.

15) Bandara, J.; Udawatta, C. P. K.; Rajapakse, C. S. K. *Photochem. Photobiol. Sci* **2005**, *4*, 857.

16) Chen, X.; Shen, S.; Guo, L.; Mao, S. S. *Chem. Rev.* **2010**, *110*, 6503.

17) Ikeue, K.; Shiiba, S.; Machida, M. *Chem. Mater.* **2010**, *22*, 743.

18) Liu, H.; Zhang, K.; Jing, D.; Liu, G.; Guo, L. *Int. J. Hydrogen Energy* **2010**, *35*, 7080.

19) Parida, K. M.; Biswal, N.; Das, D. P.; Martha, S. *Int. J. Hydrogen Energy* **2010**, *35*, 5262.

20) Li, Q.; Guo, B.; Yu, J.; Ran, J.; Zhang, B.; Yan, H.; Gong, J. R. *J. Am. Chem. Soc.* **2011**, *133*, 10878.

21) Shen, S.; Guo, L. *Mater. Res. Bull.* **2008**, *43*, 437.

22) Choi, J.; Ryu, S. Y.; Balcerski, W.; Lee, T. K.; Hoffmann, M. R. *J. Mater. Chem.* **2008**, *18*, 2371.

23) Xing, C.; Zhang, Y.; Yan, W.; Guo, L. *Int. J. Hydrogen Energy* **2006**, *31*, 2018.

24) Zong, X.; Yan, H.; Wu, G.; Ma, G.; Wen, F.; Wang, L.; Li, C. *J. Am. Chem. Soc.* **2008**, *130*, 7176.

25) Zong, X.; Wu, G.; Yan, H.; Ma, G.; Shi, J.; Wen, F.; Wang, L.; Li, C. *J. Phys. Chem. C* **2010**, *114*, 1963.

26) Lee, S. G.; Lee, S.; Lee, H. I. *Appl. Catal. A* **2001**, *207*, 173.

27) Sreethawong, T.; Suzuki, Y.; Yoshikawa, S. *Int. J. Hydrogen Energy* **2005**, *30*, 1053.

Chapter 4

Rational Design of Hierarchical 3D Heteroarrays of SrS/CdS: Synthesis, Characterization and Evaluation of photocatalytic Properties for Efficient Hydrogen Generation and Organic Dye Degradation

This chapter describes the effect of enhanced specific surface area and facile charge transfer on photocatalytic activity under UV-Vis irradiation. As synthesized hierarchical 3D SrS/CdS show high efficiency for hydrogen generation with an apparent quantum yield (AQY) of 10% and ~ 100% methyl orange dye degradation in comparison with 1D CdS NWs, SrS nanoparticles and bulk CdS under UV-Visible light irradiation. The enhance photocatalytic activity of 3D SrS/CdS is attributed to high specific surface area and facile charge transfer from CB of SrS to CB of CdS due to the favorable energy alignments of CB of SrS and CB of CdS. Mechanistic study of dye degradation involving the intermediates such as superoxide radical anion ($O_2^{\cdot -}$) and hydroxyl radical (•OH) were explained.

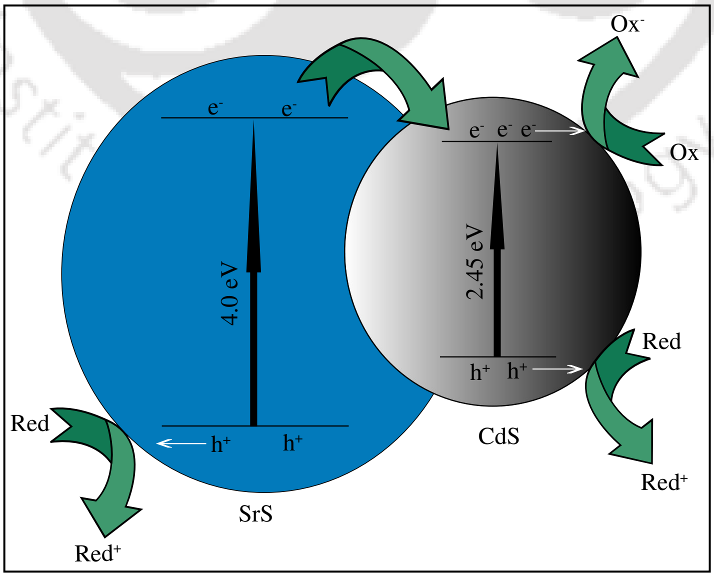

Nanoscale, **2012**, *4*, 3543

4.1. Introduction

The photocatalytic ability of binary 3D semiconducting heterostructures appears to be more promising due to the better charge separation or declined electron-hole recombination as an effect of electron migration. Therefore, nanoscale 3D semiconductor heterostructures can suitably be exploited for effective photocatalysis. In the present chapter, we have synthesized hierarchical 3D SrS/CdS binary nanostructures following a one-step hydrothermal method discussed in chapter 2. The selection of SrS is based on its band alignment with CdS; the conduction band (CB) of SrS (−1.1 eV)[1] is in close proximity to the CB of CdS (−0.88 eV)[2] which can facilitate efficient charge migration from the CB of SrS to the CB of CdS, thereby improving photocatalytic efficiency.[3,4] The obtained structure showed hierarchical growth of CdS NWs onto SrS NPs and exhibited excellent photocatalytic ability for hydrogen generation and degradation of the organic dye methyl orange.

4.2. Experimental Section

4.2.1. Synthesis of SrS NPs

SrS NPs were prepared by modified precipitation method.[5] $SrCl_2.6H_2O$ (1 g) was dissolved in 50 mL distilled water followed by the drop wise addition of excess amount of Na_2S solution (~4-fold) under vigorous stirring condition in presence of thioglycolic acid. The reaction mixture was then stirred at room temperature for 24 h. The resulting white precipitate was filtered and washed with water-ethanol mixture. The product was dried at 70 °C for 12 h in an electronic oven.

4.2.2. Synthesis of hierarchical 3D SrS/CdS

Hierarchical 3D SrS/CdS binary nanostructure was synthesized by hydrothermal method. In a typical synthesis, $SrCl_2.6H_2O$ (3.9 mmol) was dissolved in 15 mL distilled water followed by the addition of thioglycolic acid (12.9 mmol) under vigorous stirring. After the addition of $Cd(OOCCH_3)_2.2H_2O$ (9.0 mmol) and aquous NH_3 (to maintain pH 7), reaction mixture was stirred at room temperature for 30 min. It is worth noting that keeping the ratio of strontium chloride to cadmium acetate to 0.43:1 (Sr^{2+}:Cd^{2+}) resulted in better hierarchical growth of CdS NWs onto the SrS nanoparticles. The resultant suspension was transferred to a Teflon-lined stainless steel autoclave, in an oven at 140 °C for 24 h. After cooling down to room temperature, the solution obtained was centrifuged and the solid product was washed with water and ethanol to remove excess metal ions and thioglycolic acid, if any. Finally, the product was dried in oven at 70 °C for 4-5 h yielding pure SrS/CdS.

4.3. Results and Discussion

4.3.1. Mechanism of the Formation of Hierarchical 3D SrS/CdS Heteroarrays

In the literature, it was reported that organic molecules played an important role for the formation of inorganic 3D architecture. For example, 3D CdS nanocrystals with flower-like structure were prepared using hexamethylenetetramine as the capping agent,[6] 3D dendritic CdS nanoarchitectures were prepared using cetylpyridinium chloride as the capping agent etc.[7] However, previous studies showed that the hydroxyl groups could also involve in stabilizing, order, and controlling the spatial arrangement of the inorganic nanoparticles by spreading over the surface of these nanoparticles.[8-11] Interestingly, in the current study thioglycolic acid is involved in the preparation of hierarchical 3D SrS/CdS heteroarrays as a sulfur precursor having hydroxyl group. Therefore, it is proposed that the hydroxyl group of thioglycolic acid might spread over the synthesized SrS and CdS nanoparticles. Amount of SrS NPs are less in the solution which leads to the ordered growth of CdS NWs on SrS NPs at hydrothermal condition, and further results in the formation of hierarchical 3D SrS/CdS architecture. The detailed schematic of proposed mechanism for the formation of 3D SrS/CdS is discussed in scheme 4.1.

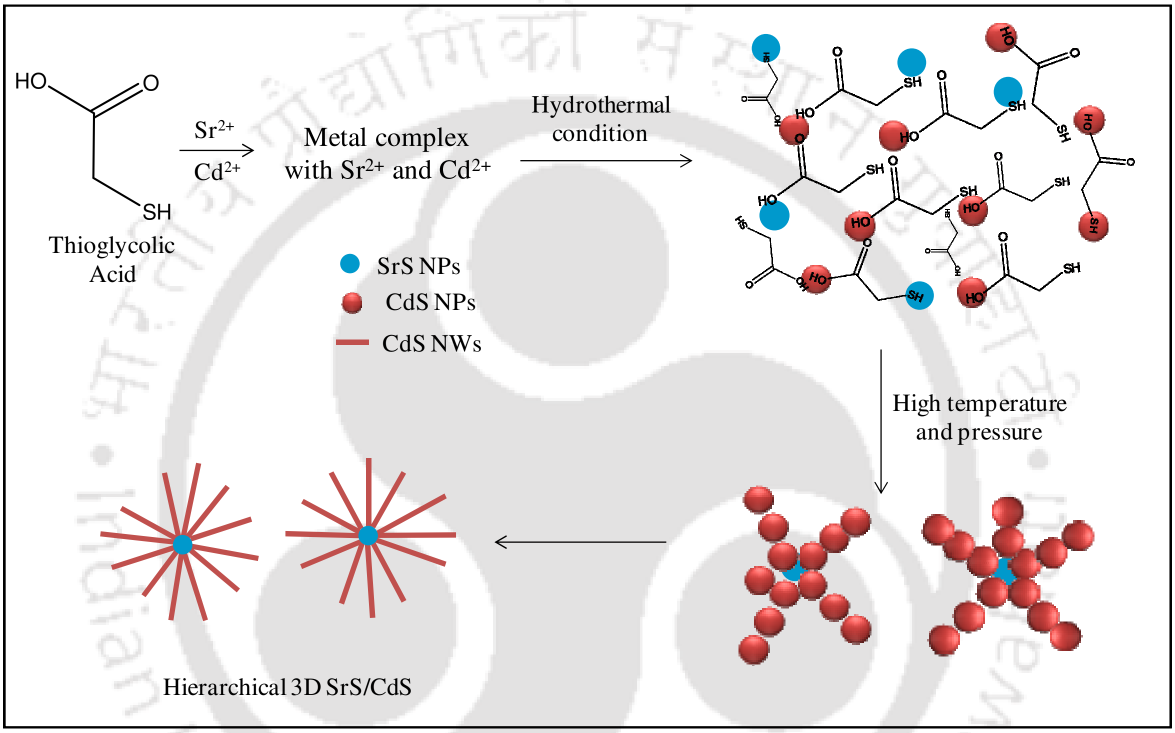

Scheme 4.1 Schematic illustration for the formation of the hierarchical 3D SrS/CdS heteroarrays

4.3.2. Materials Morphology

The morphology of the sample was analyzed by FE-SEM. Figure 4.1a-e shows FE-SEM images of as-prepared SrS/CdS at different magnifications. FE-SEM images of the obtained material shows the formation of three dimensional (3D) hierarchical structures of about ~3 μm in size. Magnified view of these hetero-structures (Figure 4.1e) showed that the 3D nanostructures were assembly of CdS NWs with an average diameter of 50 nm and length of 500 nm on to the SrS nanoparticles. The Energy Dispersive X-ray (EDX) pattern indicated the presence of Cd, Sr and S elements in the 3D SrS/CdS hierarchical structures (Figure 4.1f).

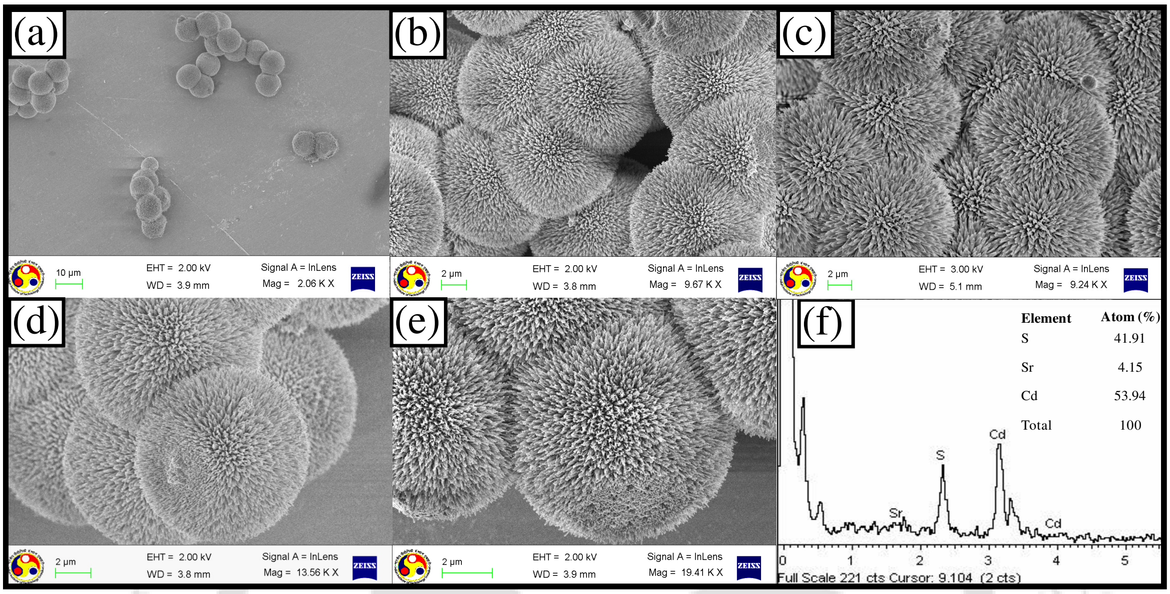

Figure 4.1 (a-e) FE-SEM images at different magnifications (f) EDX pattern along with quantitative elemental analysis of hierarchical 3D SrS/CdS

TEM analysis also shows that the CdS NWs were aligned radially and appears to be originating from a single bunch of SrS NPs giving it a flower like morphology (Figure 4.2a). It should be noted that there is a contradiction in the size of hierarchical 3D SrS/CdS between FE-SEM and TEM image because at low magnification the TEM images of the larger particles were not clear; they appeared as dark patches. Therefore, in order to obtain the clear structure of the particle TEM image was taken for the particle having smaller size (the sample was prepared from the supernatant of the SrS/CdS dispersion). Several rod like shapes were seen in the TEM image along with flower like structure, are bare CdS NWs. In order to obtain the high resolution TEM (HR-TEM) image for hierarchical 3D SrS/CdS, the sample was treated ultrasonically for 1 h. After ultrasonic treatment of sample, the flower like structure broke into the fragments (Figure 4.2c) which was used for HR-TEM. The HR-TEM of 3D SrS/CdS (Figure 4.2d) reveals that crystallized CdS

NWs with lattice spacing of 0.337 nm, corresponding to the (002) plane (JCPDS 06-0314) of hexagonal CdS, is directly connected with (220) plane (JCPDS 08-0489) of cubic SrS NPs with lattice spacing of 0.204 nm. TEM analysis of the as-prepared SrS NPs were also performed and shown in Figure 4.2e-h. TEM analysis reveals that prepared SrS nanoparticles are spherical in nature with 30-40 nm of diameter.

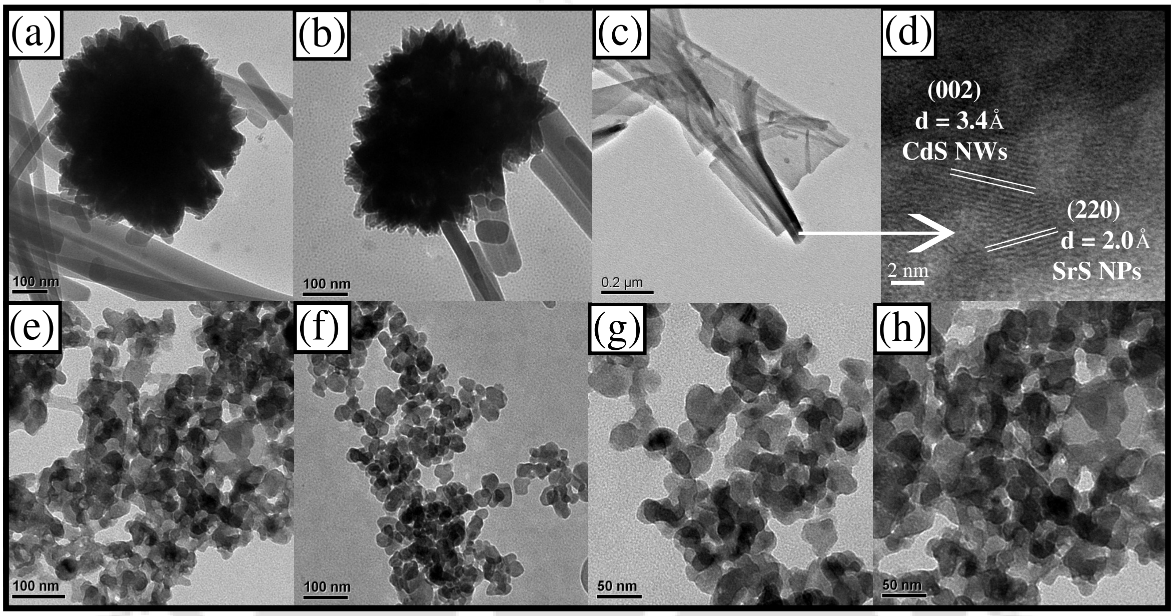

Figure 4.2 (a and b) TEM images, of hierarchical 3D SrS/CdS (c) TEM image of SrS/CdS after ultra-sonication and (d) High Resolution-TEM (HR-TEM) image of hierarchical 3D SrS/CdS (e-h) TEM images of prepared SrS NPs at different magnifications

4.3.3. Powder X-ray Diffractogram

The purity of the as-prepared 3D SrS/CdS and its crystalline phase were confirmed from the powder X-ray diffraction (PXRD) pattern. PXRD pattern for SrS NPs, 1D CdS NWs and 3D SrS/CdS are shown in Figure 4.3. Distinct lattice planes corresponding to the cubic phase of SrS (JCPDS 08-0489) and hexagonal phase of CdS (JCPDS 06-0314) were revealed in the diffraction pattern, corroborating the presence of individual components of SrS and CdS in the 3D SrS/CdS hetero structure. No diffraction peaks form the other crystalline forms were detected. The unit cell parameter calculations for these samples were carried out and compared with the above reference cards which are given in Table 4.1. PXRD suggests that the structure and crystallinity of 1D CdS NWs is retained even after it is grown onto the SrS nanoparticle to produce hierarchical 3D SrS/CdS.

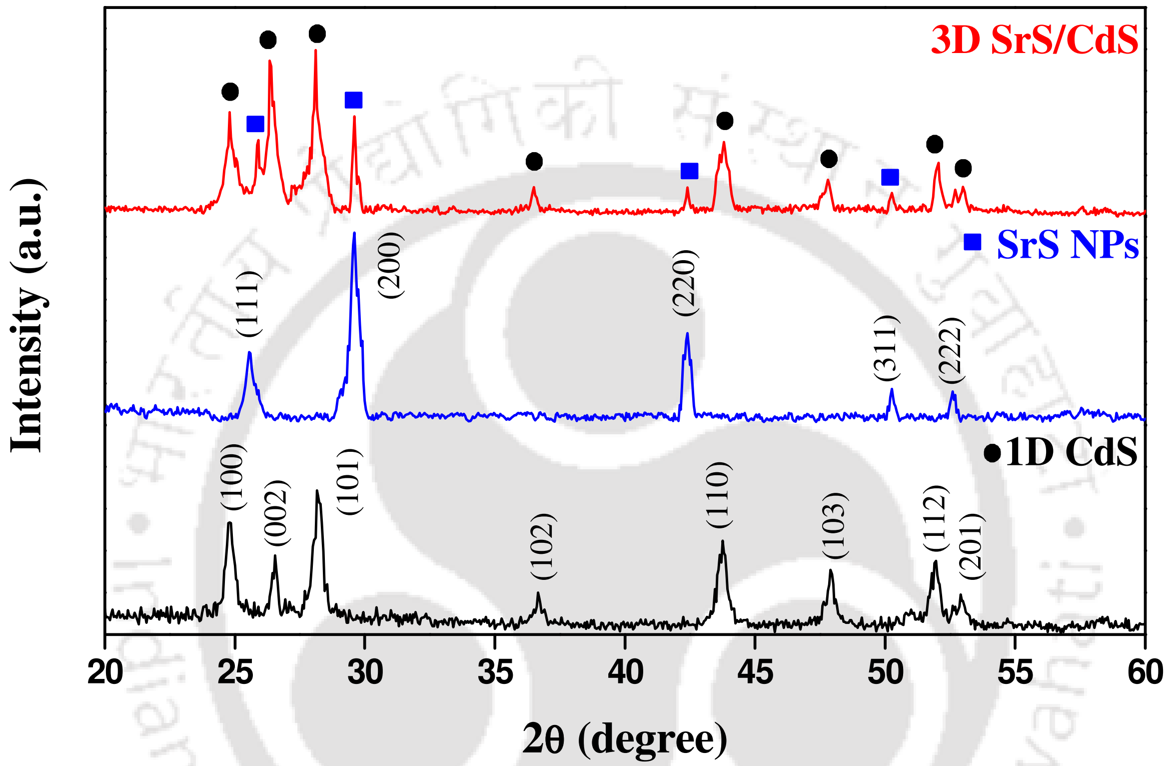

Figure 4.3 Powder X-ray diffraction patterns for 1D CdS NWs, SrS NPs and 3D SrS/CdS

Table 4.1 Comparison of unit cell parameters with the reported referenced card (JCPDS 06-0314and JCPDS 08-0489)

Samples	Unit Cell Parameters (Calculated)	Unit Cell Parameters (Reported)
CdS NWs	a = 0.391 nm & c = 0.6710 nm	a = 0.4136 nm & c = 0.6713 nm
SrS NPs	a = 0.593 nm	a = 0.6020 nm
CdS in 3D SrS/CdS	a = 0.397 nm & c = 0.6756 nm	a = 0.4136 nm & c = 0.6713 nm
SrS in 3D SrS/CdS	a = 0.595 nm	a = 0.6020 nm

4.3.4. UV-Vis Diffuse Reflectance Spectra

UV-Vis diffuse reflectance spectra of the as-prepared SrS NPs, 1D CdS NWs and 3D SrS/CdS is shown in Figure 4.4. The absorption spectra were recorded in the wavelength range of 250–750 nm. Interestingly, all these photocatalysts show almost the same absorption profile with a steep absorption edge in ultraviolet and visible range, which corresponds to the band gap energy for the individual components. From UV-Vis spectra we can see that 3D SrS/CdS shows two sharp absorption steeps at *ca.* 4.0 eV and *ca.* 2.3 eV corresponding to the SrS and CdS respectively. No contamination peak was observed in the absorption profile of photocatalysts.

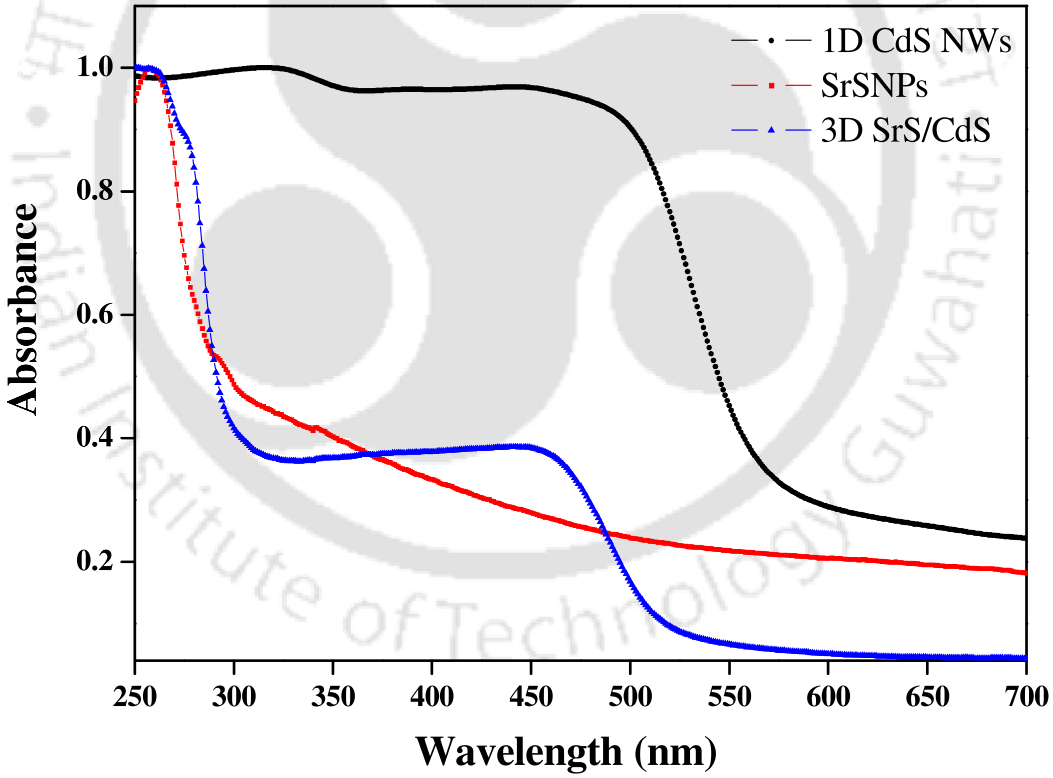

Figure 4.4 UV-Vis diffuse reflectance spectra for 1D CdS NWs, SrS NPs, and 3D SrS/CdS photocatalyst

4.3.5. BET Surface Area Analyses

The N_2 adsorption-desorption isotherms of hierarchical 3D SrS/CdS heteroarrays and 1D CdS NWs were measured as shown in Figure 4.5. According to the Brunauer-Deming-Deming-Teller (BDDT) classification, the physisorption isotherms can be grouped into six types.[12] Both 3D SrS/CdS and 1D CdS NWs display typical type-IV isotherms and type H3 hysteresis loops, which are the characteristic feature of mesopores.

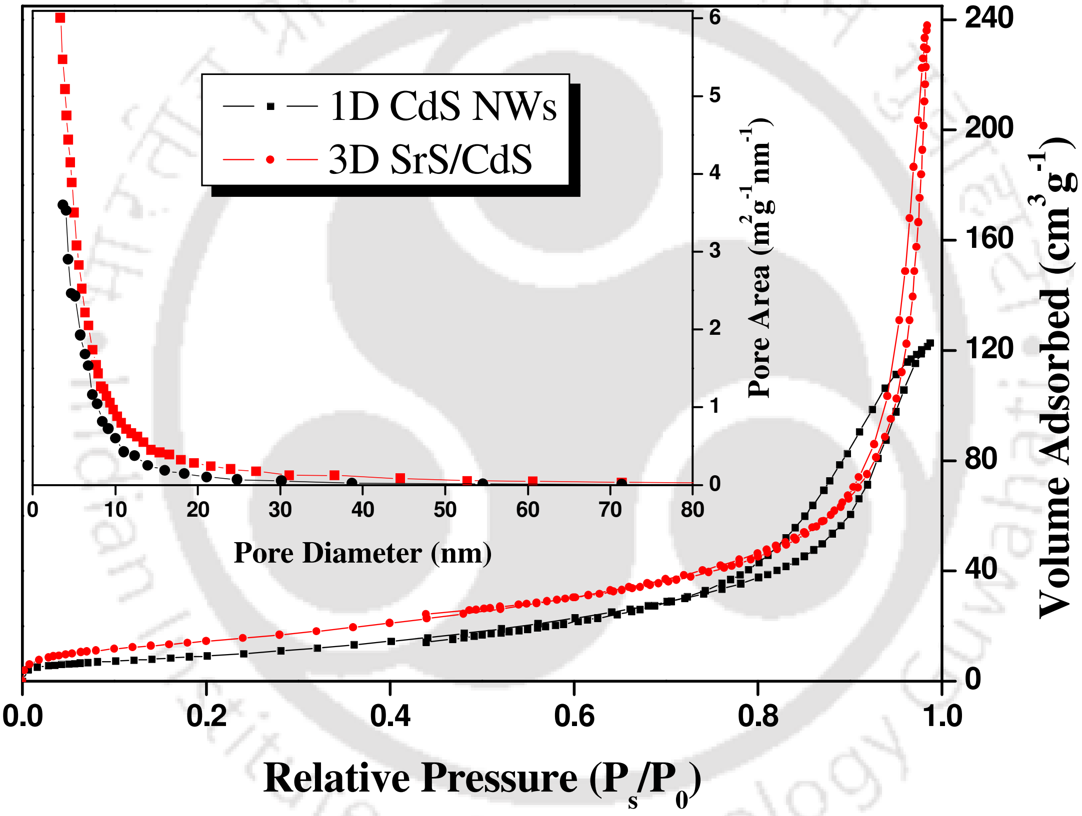

Figure 4.5 Nitrogen adsorption-desorption isotherm and in inset BJH plot for pore size distribution for hierarchical 3D SrS/CdS heteroarrays and 1D CdS NWs. N_2 adsorption-desorption isotherm confirms the formation of porous photocatalyst material

The adsorption isotherm clearly indicates that hierarchical 3D SrS/CdS is a porous material. The hierarchical 3D SrS/CdS flower like heteroarrays showed enhanced BET surface area (52 m^2/g) in comparison with 1D CdS NWs (30 m^2/g) and the CdS bulk (1 m^2/g). The Barret-Joyner-Halenda (BJH) pore size distribution was similar in character (inset Figure 4.5) for 1D CdS NWs and hierarchical 3D SrS/CdS. Therefore, it is obvious that the surface morphology of 1D CdS NWs remains identical even after its growth on SrS NPs.

4.3.6. Photocatalytic Hydrogen Generation

In order to examine the H_2 production ability of as-synthesized 3D SrS/CdS, photocatalytic water splitting experiment was carried out. Water splitting experiment were also conducted using bulk CdS, 1D CdS NWs and SrS NPs for the sake of comparison of H_2 production efficiency with that of 3D SrS/CdS. The H_2 evolution rates under UV-Vis irradiation and specific surface area of bulk CdS, 1D CdS NWs and 3D SrS/CdS are shown in Figure 4.6. It can be observed from Figure 4.6 that hierarchical 3D SrS/CdS is having higher photocatalytic activity with highest H_2 production rate of 246 µmol/h; in comparison to 1D CdS NWs. The increased photocatalytic activity is attributed to the enhanced specific surface area, facile charge migration and crystalline phase of CdS in 3D SrS/CdS. The hydrogen generation experiment for SrS NPs was also carried out under UV irradiation. The hydrogen evolution for SrS is found to be 9.22 µmol/h/0.2g with an AQY of only 0.40%.

Based on the previous reports,[3,4] we have proposed a mechanism for the facile intersystem charge transfer between SrS and CdS in 3D SrS/CdS. A schematic elucidation for efficient charge separation with the details of electron transfer process and energy band positions of SrS and CdS in 3D SrS/CdS is shown in scheme 4.2. Irradiation of light onto the photocatalyst causes its activation, leading to the formation of reductive electrons and oxidative holes in the conduction band (CB) and valence band (VB), respectively, of SrS and CdS. The proximity of the CB of SrS (−1.1 eV) and CdS (–0.88 eV) facilitates the migration of electrons from the CB of SrS to the CB of CdS, further reducing the electron-hole pair recombination. The pool of electrons thus generated in the CB of CdS causes the reduction of H^+ ions and thereby producing H_2 gas. Meanwhile, the generated oxidative holes are consumed in the reduction process of Na_2SO_3 which acts as sacrificial reagent leaving behind the CB electrons. In addition to the above mentioned factors the hexagonal phase of CdS in the 3D SrS/CdS could possibly be another reason for the efficient H_2 production as reported by Matsumura *et al.*[23] The apparent quantum yield (AQY) for hydrogen generation using 3D SrS/CdS was calculated to be 10% which was about three fold higher than that of 1D CdS NWs whose AQY was around 3.5 %. The AQY for 3D SrS/CdS was almost two times more than the reported SrS/CdS nanocomposite.[5]

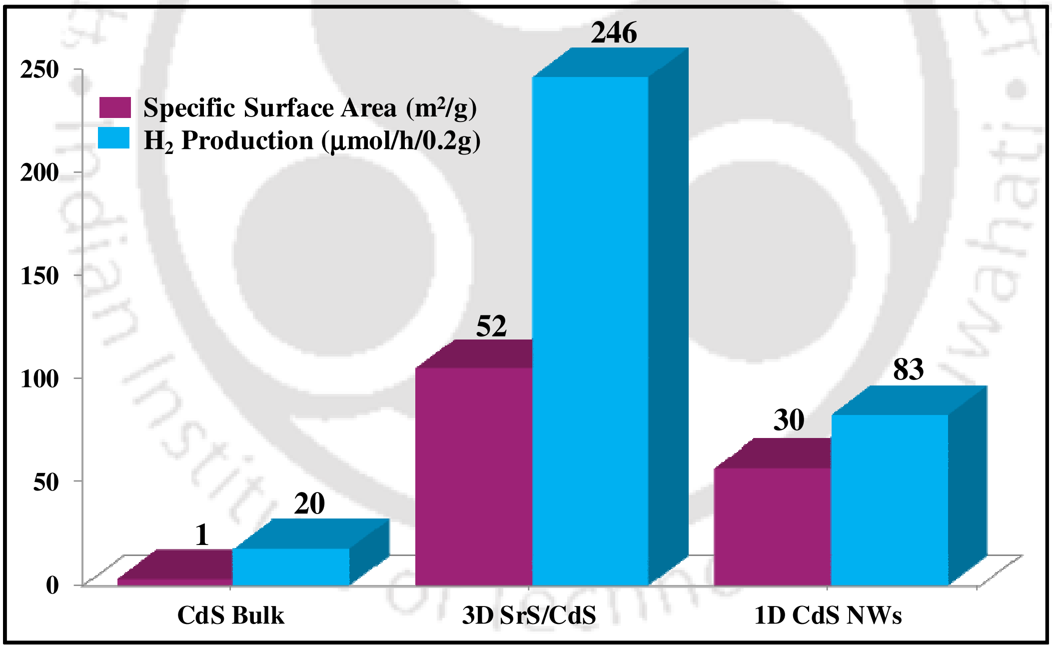

Figure 4.6 Specific surface area and amount of H_2 generation from CdS bulk, CdS NWs, and 3D SrS/CdS photocatalysts

The supremacy of the present 3D SrS/CdS photocatalyst also lies in the fact that enhanced hydrogen production is achieved without the aid of any noble metal co-catalyst such as Pt, Pd, Rh, Ru etc, which greatly reduces the cost of photocatalysis. In general, co-catalyst works by facilitating better charge separation of photoinduced electrons and holes due of their lower band position. Based on this idea hierarchical 3D SrS/CdS has been synthesized which resulted in an efficient photocatalysis. 3D SrS/CdS catalyst provides better conduction pathway for photogenerated electrons due to (i) the CB alignment of SrS and CdS (ii) increased specific surface area and (iii) high crystallinity rendering the production of H_2 more efficient. Therefore, the need of noble metal co-catalyst can be eliminated by making 3D hierarchical structures of SrS/CdS.

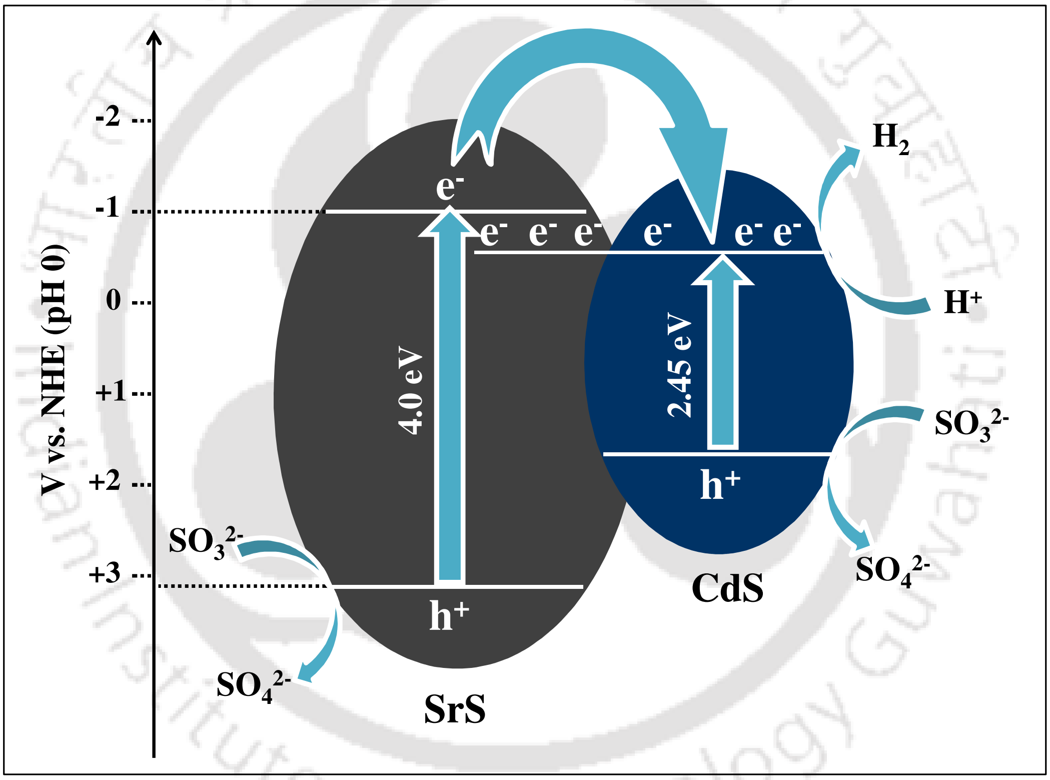

Scheme 4.2 Schematic of the electron transfer and the energy band positions of SrS and CdS in the hierarchical 3D SrS/CdS

4.3.7. Photocatalytic Dye Degradation

Along with efficient H_2 production, 3D SrS/CdS exhibits excellent photocatalytic activity for the degradation of organic dye, methyl orange (MO). The photodegradation of

MO (absorbance spectra shown in Figure 4.7) was studied by measuring the concentration of the dye after irradiation with UV-Vis light for varying time periods. The concentration of un-degraded MO relative to its initial concentration (C/C_0) after irradiation in the presence of 3D SrS/CdS and 1D CdS NWs along with SrS NPs catalyst at different intervals of time are shown in Figure 4.8. Within 25 min of irradiation 97% of MO degradation was achieved whereas, nearly complete degradation (~100%) of MO occurred within 40 minutes in presence of 3D SrS/CdS photocatalyst.

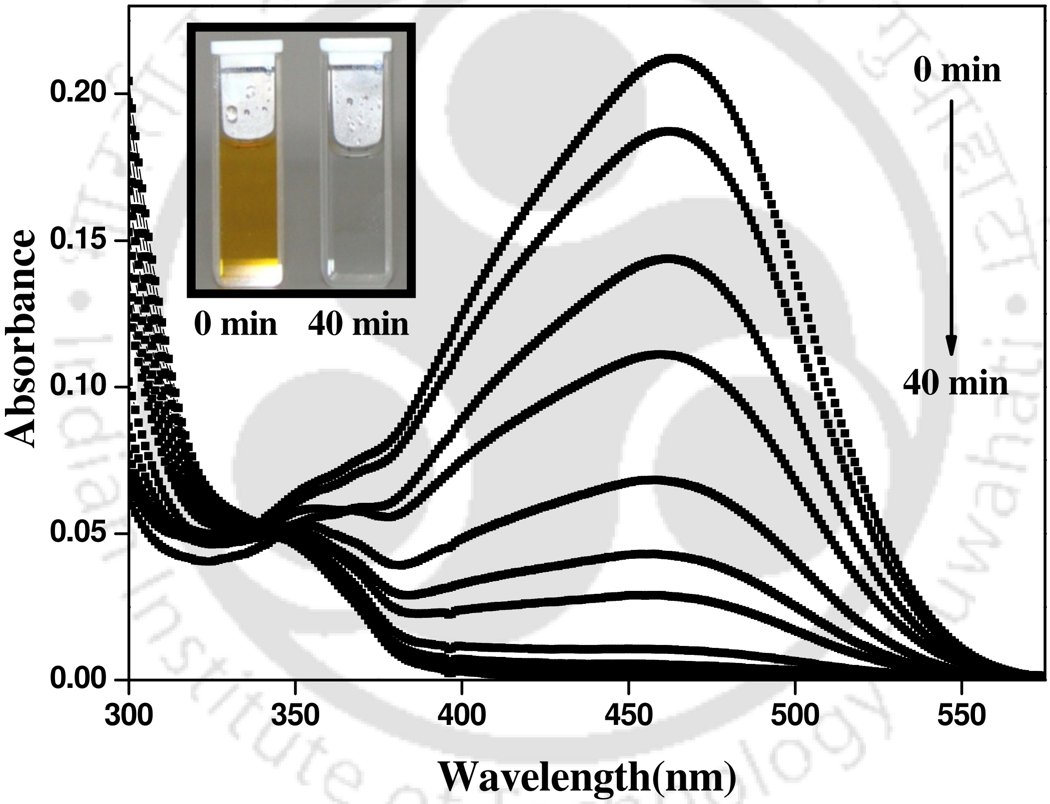

Figure 4.7 UV-Vis absorption spectra of MO with 3D SrS/CdS, inset cuvette image of MO before and after irradiation

The photodegradation of MO was observed to follow first order decay kinetics, as seen from the apparent first order linear transform $\ln(C/C_0) = -k_{app}t$,[13] shown in Figure 4.8. Where C_0 and C represent the concentration of MO before and after irradiation respectively, k_{app} is the apparent first-order reaction rate constant representing the reaction rate and could be calculated from the slope of the plot (Figure 4.8). The comparative account of photocatalytic degradation rate constant (k_{app}) of SrS NPs, CdS NWs and 3D SrS/CdS is given in Table 4.2.

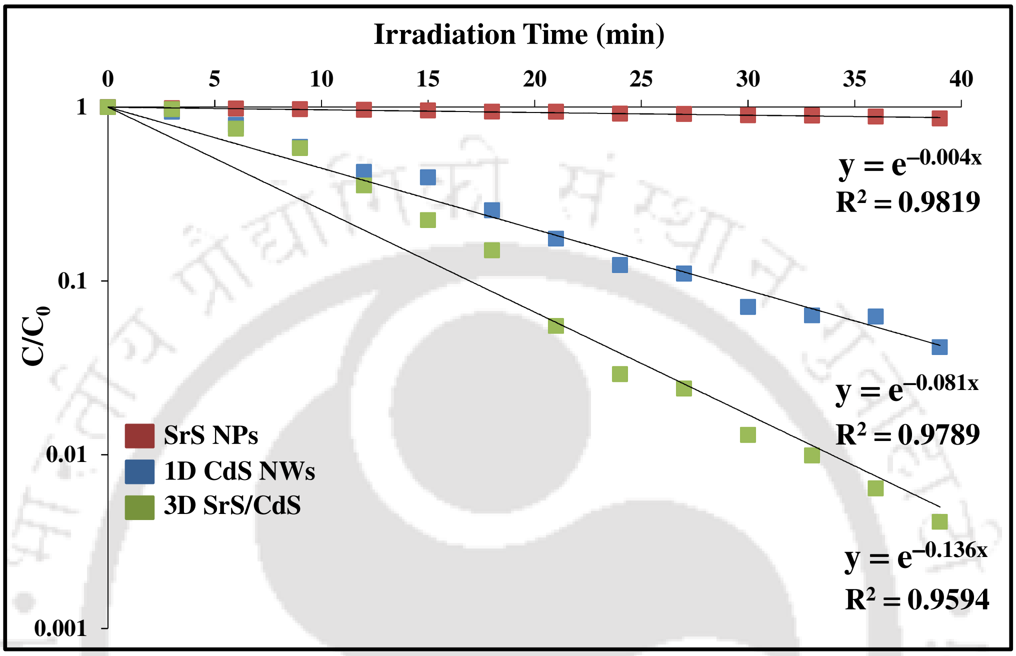

Figure 4.8 Evolution of apparent rate constant versus irradiation time in the presence of SrS NPs, CdS NWs and 3D SrS/CdS catalyst

Table 4.2 Apparent rate constant (k_{app}) of MO photodegradation and linear regression coefficients from the plot $\ln(C/C_0) = -k_{aap}t$

Photocatalysts	**R^2**	**k_{app} (min^{-1})**
SrS NPs	0.982	0.004
CdS NWs	0.979	0.081
3D SrS/CdS	0.959	0.136

The degradation efficiencies (E_{ff}) for SrS NPs, 1D CdS NWs and 3D SrS/CdS were evaluated based on the initial and final concentration of the dye.[14] It was found that 3D SrS/CdS were able to degrade the dye with 99.6% efficiency whereas, SrS NPs and CdS

NWs showed efficiencies of about 14% and 94% respectively. The surge in the rate of degradation with enhanced efficiency of 3D SrS/CdS could be attributed to the increased specific surface area and combined effect of SrS and CdS due to their band alignment, which is also responsible for the increased H_2 production rate. The proposed schematic of the mechanism for the degradation of MO by 3D SrS/CdS is shown in scheme 4.3.

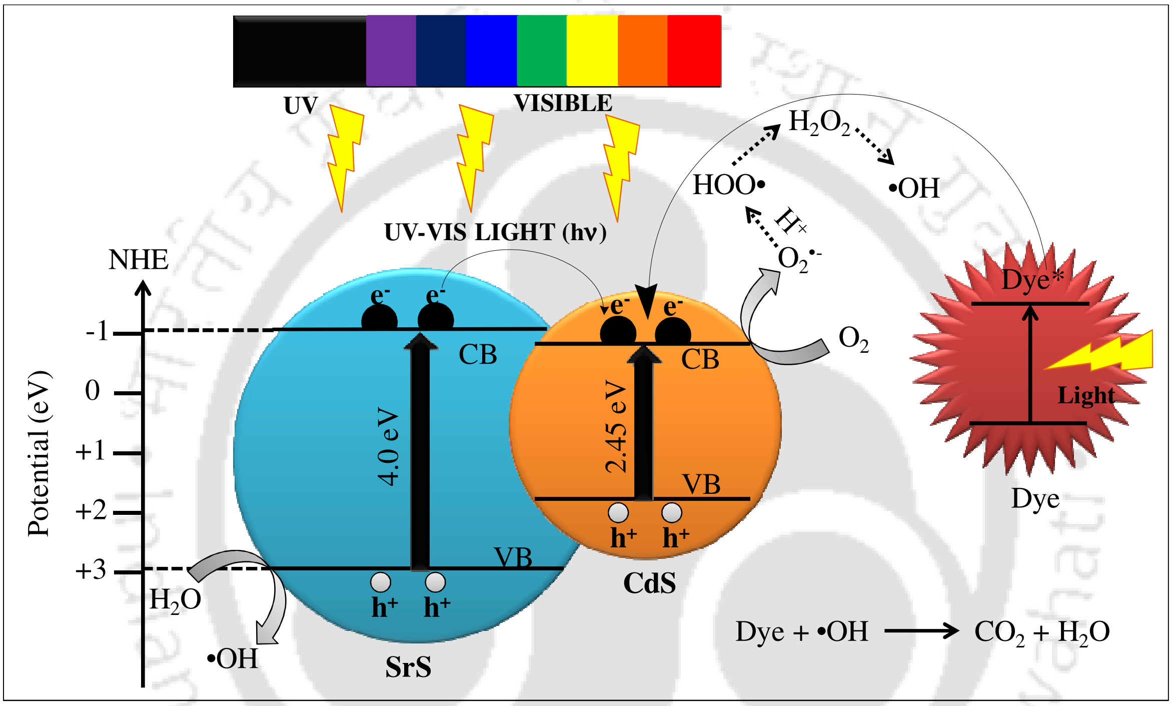

Scheme 4.3 Schematic presentation of generation of hydroxyl radicals by excitation of SrS/CdS using UV-Vis irradiation

4.3.7.1. Mechanism for Photodegradation of Dye

The degradation of MO involves several steps and the proposed mechanism is shown in scheme 4.4. Irradiation of light leads the formation of electrons in the CB and holes in the VB of hybrid photocatalyst material. The photogenerated electrons in the CB of SrS can get transferred to the CB of CdS (step 1), inducing the reduction of the molecular oxygen O_2 to superoxide radical anion $O_2^{\bullet -}$ (step 2). In aqueous medium, the holes in the VB react with water to produce hydroxyl radical (step 3). Hydroxyl radicals can recombine to form H_2O_2 (step 4). This H_2O_2 can react with superoxide radical anion to regenerate hydroxyl radical (step 5) which leads the decomposition of organic dye (step 6).[15]

$$\begin{array}{rcll}
\textbf{Photocatalyst} + h\nu & \longrightarrow & e^-_{cb} + h^+_{vb} & \textbf{Step 1} \\
e^-_{cb} + O_2 & \longrightarrow & O_2^{\bullet -} & \textbf{Step 2} \\
h^+_{vb} + H_2O & \longrightarrow & \bullet OH + H^+ & \textbf{Step 3} \\
\bullet OH + \bullet OH & \longrightarrow & H_2O_2 & \textbf{Step 4} \\
H_2O_2 + O_2^{\bullet -} & \longrightarrow & \bullet OH + {}^-OH + O_2 & \textbf{Step 5} \\
\text{Dye} + \bullet OH & \longrightarrow & CO_2 + H_2O & \textbf{Step 6}
\end{array}$$

Scheme 4.4 Proposed mechanism for the degradation of organic dye

4.3.7.2. Evidence for the Formation of Superoxide Radical Anion ($O_2^{\bullet -}$) and Hydroxide Radical (•OH)

From scheme 4.4, it is clear that the degradation rate of organic dye mostly depends on the concentration of superoxide radical anion ($O_2^{\bullet -}$) and hydroxyl radical (•OH). Superoxide radical anion forms by the reduction of dissolved molecular oxygen in water (step 2) which is responsible for the formation of hydroxyl radical. Therefore, it is obvious that concentration of molecular oxygen is a critical factor for dye degradation. Hence, in order to examine our claim, MO degradation experiment was performed with deoxygenated water (prepared by freeze-thaw cycle) in presence of hierarchical 3D SrS/CdS photocatalyst. The photodegradation rate of MO was studied by measuring the concentration of the dye after irradiation with UV-Vis light for varying time periods. The photodegradation of MO was observed to follow a first order decay kinetics (Figure 4.9) with apparent rate constant (k_{app}) of 0.011min^{-1}.

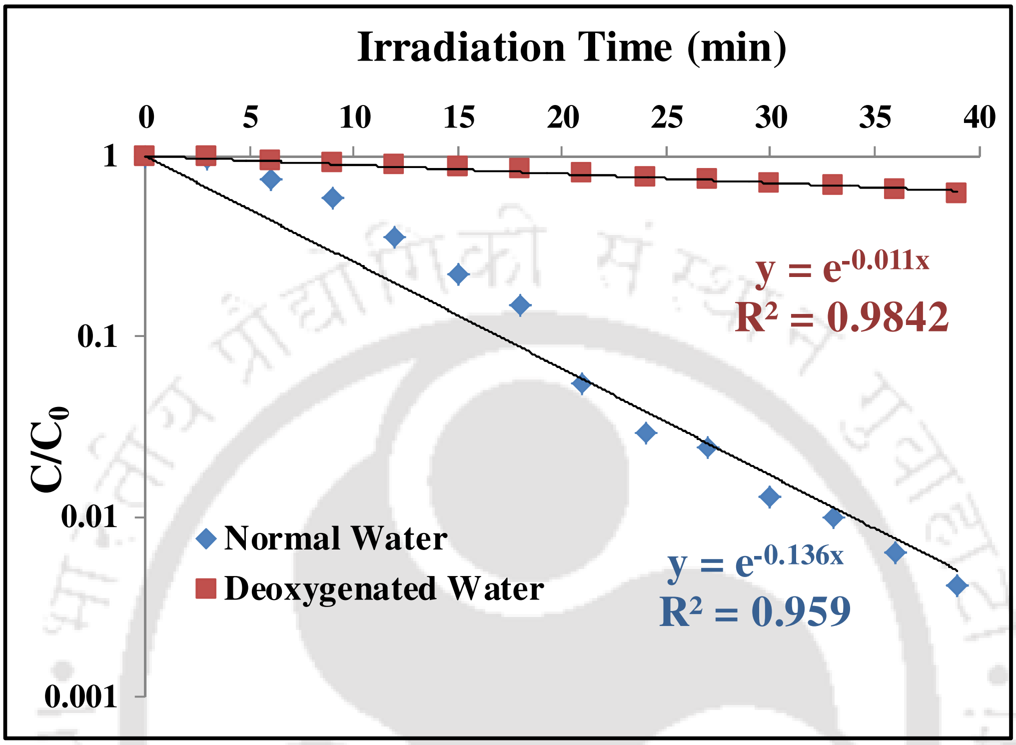

Figure 4.9 The C/C_0 versus irradiation time curves of photodegradation of MO. The apparent rate constant of MO photodegradation for 3D SrS/CdS in deoxygenated water (0.011 min^{-1}) is less than that in normal water

The degradation rate of MO is also affected by the concentration of hydroxyl radical (•OH). To study the effect of •OH radical on degradation rate, the MO degradation experiment was performed in presence of additive metal ion (Fe^{2+}). Fe^{2+} probably undergoes the oxidation reaction in solution with •OH radicals present in the solution.[16]

$$Fe^{2+} + {}^{\cdot}OH \longrightarrow Fe^{3+} + OH^{-}$$

Thus, in presence of Fe^{2+}, hydroxyl radicals are easily converted to OH^{-}, thereby decreasing the concentration of •OH radicals and hence less degradation of MO solution was achieved (shown in Figure 4.10). The apparent rate constant (k_{app}) for MO degradation in presence of Fe^{2+} (0.007 min^{-1}) is less than that of without metal ion (0.136 min^{-1}).

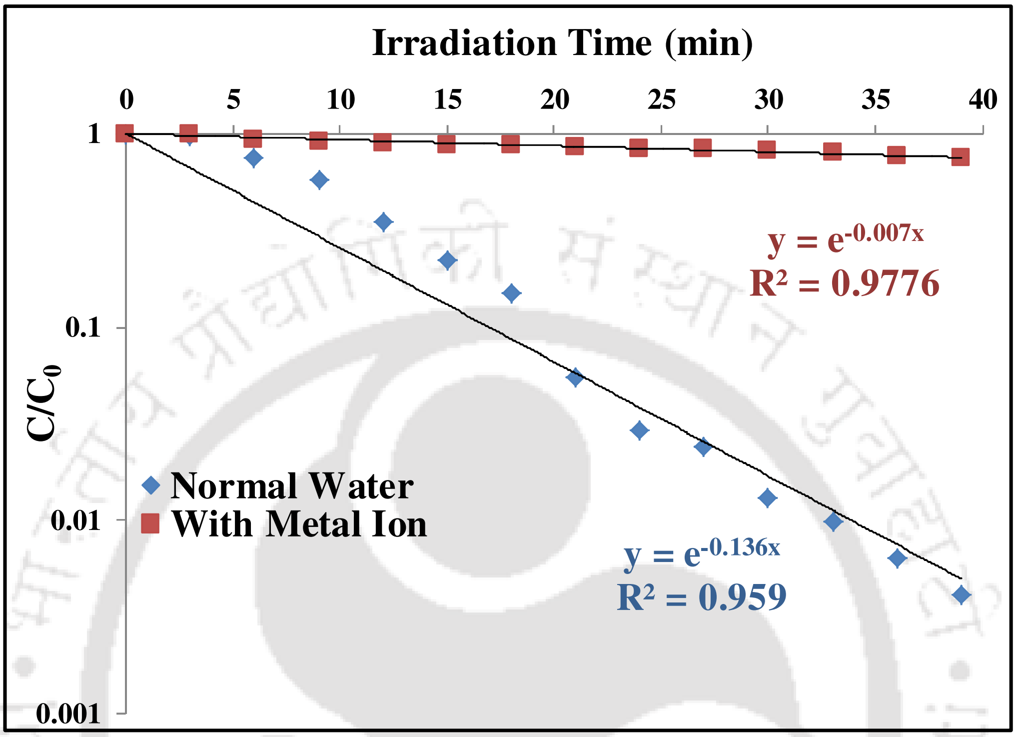

Figure 4.10 The *C/C₀* versus irradiation time curves of photodegradation of MO. The apparent rate constant of MO photodegradation for 3D SrS/CdS in presence of Fe^{2+} (0.007 min^{-1}) is less than that in normal water

4.4. Conclusion

1. We have demonstrated a simple one pot synthesis of hetero structures of SrS/CdS, which are hierarchical in nature with an average diameter of 500 nm characterized by TEM and SEM.
2. Hierarchical 3D SrS/CdS structures which act as an efficient photocatalyst for hydrogen generation by water splitting with apparent quantum yield up to 10% are reported.

3. Additionally, we also observed that 3D SrS/CdS acts as efficient photocatalyst in degrading organic dye (Methyl Orange) with an efficacy of ~100% in a short span of time.
4. Detailed dye degradation mechanism also carried out and formation of intermediates like superoxide radical anion, hydroxyl radical is confirmed.
5. The kinetics study of dye degradation by 3D SrS/CdS revealed that decay follow first order kinetics with apparent rate constant (k_{app}) value 0.136 min^{-1}.
6. Present approach offers a viable route to synthesize a variety of hetero-structures for hydrogen production and organic pollutant degradations in future.

References

1) Sosa, V.; Rack, P. D.; Holloway, P. H. *J. Vac. Sci. Tech. A* **1998**, *16*, 393.

2) Kudo, A.; Miseki, Y. *Chem. Soc. Rev.* **2009**, *38*, 253.

3) Liu, Z.; Bai, H.; Xu, S.; Sun, D. D. *Int. J. Hydrogen Energy* **2011**, *36*, 13473.

4) Bandara, J.; Udawatta, C. P. K.; Rajapakse, C. S. K. *Photochem. Photobiol. Sci* **2005**, *4*, 857.

5) Liu, H.; Zhang, K.; Jing, D.; Liu, G.; Guo, L. *Int. J. of Hydrogen Energy* **2010**, *35*, 7080.

6) Chen, F.; Zhou, R.; Yang, L.; Liu, N.; Wang, M.; Chen, H. *J. Phys. Chem. C* **2008**, *112*, 1001.

7) Wang, D.; Li, D.; Guo, L.; Fu, F.; Zhang, Z.; Wei, Q. *J. Phys. Chem. C* **2009**, *113*, 5984.

8) Bozanic, D. K.; Djokovic, V.; Blanusa, J.; Nair, P. S.; Georges, M. K.; Radhakrishnan, T. *Eur. Phys. J. E* **2007**, *22*, 5.

9) Carrot, G.; Rutot-Houze, D.; Pottier, A.; Degee, P.; Hilborn, J.; Dubois, P. *Macromolecules* **2002**, *35*, 8400.

10) Rodriguez, P.; Munoz-Aguirre, N.; Martinez, E. S.; Cruz, G. G. de la; Tomas, S. A.; Angel, O. Z. *J. Cryst. Growth* **2008**, *310*, 160.

11) Yeh, S.-W.; Wu, T.-L.; Wei, K.-H. *Nanotechnology* **2005**, *16*, 683.

12) Sing, K. S.W.; Everett, D. H.; Haul, R.; Moscou, L.; Pierotti, R. A.; Rouquerol, J.; Siemieniewska, T. *Pure Appl. Chem.* **1985**, *57*, 603.

13) Li, X.; Wang, D.; Cheng, G.; Luo, Q.; An, J.; Wang, Y. *Appl. Catal. B: Enviorn.* **2008**, *81*, 267.

14) Zhang, H.; Wu, P.; Li, Y.; Liao, L.; Fang, Z.; Zhong, X. *ChemCatChem* **2010**, *2*, 1115.

15) Konstantinou, I. K.; Albanis, T. A. *Appl. Catal.,B: Enviorn.* **2004**, *49*, 1.

16) Rauf, M. A.; Ashraf, S. S. *Chemical Engineering Journal* **2009**, *151*, 10.

Chapter 5

CdS/Metal Oxide Hybrids as Visible Light Driven Photocatalyst for Efficient Hydrogen Generation and Organic Dye Degradation Coupled with Graphene Oxide Nano-sheets

CdS/Metal Oxide (Metal Oxide = ZnO, Al_2O_3) hybrids exhibited improved photocatalytic activity in the presence of graphene oxide. Superior photocatalytic properties are attributed to the enhanced surface area and effective separation of photoinduced charge carriers due to the presence of graphene oxide.

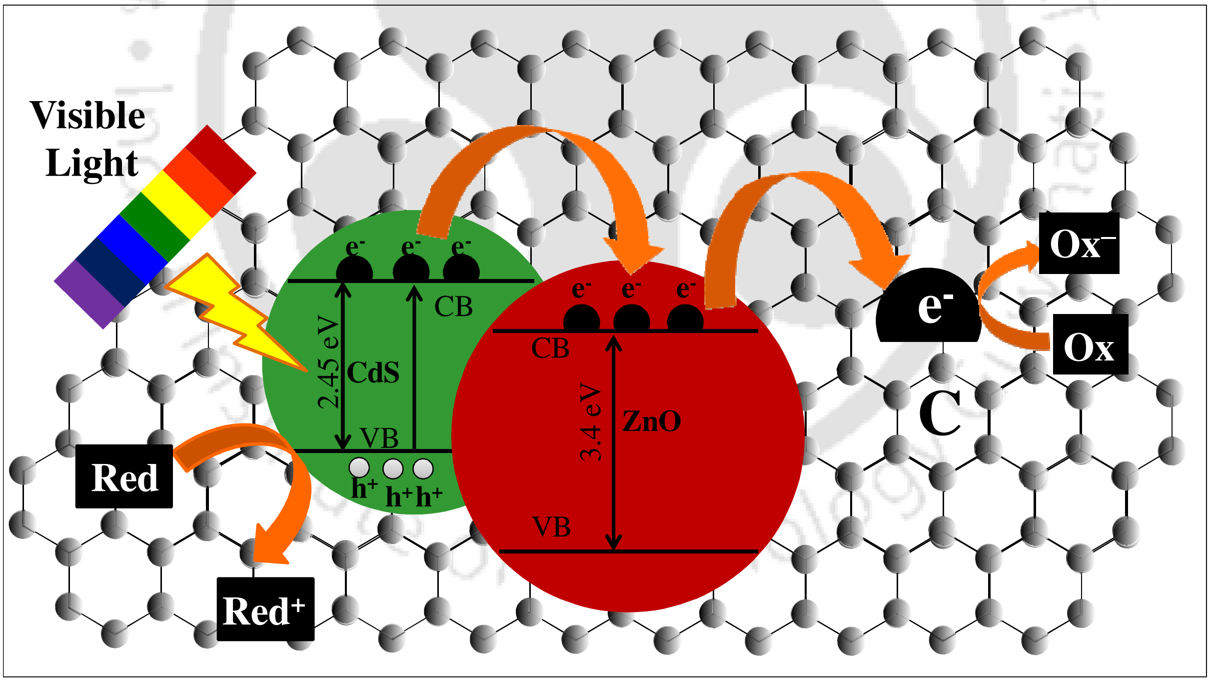

5.1. Introduction

Most of the studies concerning CdS are focused on the improvement of photocatalytic activities by synthesizing various CdS based nanostructured materials, *via* coupling with the wide band gap semiconductors (TiO_2, ZnO) and by deposition of noble metal.[1-6] However, latest studies have revealed that carbon nanomaterials; specifically carbon nanotubes (CNTs) are promising cost effective co-catalyst.[7-9] It is anticipated that CNTs are capable of accepting, transporting and storing electrons, and thus reducing the recombination of the photoinduced electrons and holes.[7,9] For example, Peng *et al.* has demonstrated the effect of multi-walled carbon nanotubes (MWCNTs) on the photocatalytic activity of CdS.[10] Analogous to CNTs, graphene can also act as an outstanding material for acceptor and transport of electron because of its conductivity, high electron mobility and large theoretical specific surface area.[11] Due to the electron-acceptor/transport property, graphene has drawn increasing attention as a co-catalyst in photocatalytic processes.[12] Therefore, lots of efforts have been made to synthesize graphene and semiconductor based hybrid materials with superior photocatalytic activity.

In this chapter we have demonstrated the synthesis of CdS, metal oxides (Al_2O_3, ZnO) and graphene oxide (GO) hybrids and their application to photocatalytic hydrogen generation by water reduction and degradation of organic dye under visible light irradiation. Selection of GO is based on the fact that its work function has a close match with that of the conduction band (CB) position of CdS which can facilitate efficient separation of photoinduced electrons and holes thereby, making photocatalysis process more efficient and cost effective.

5.2. Experimental Section

5.2.1. Synthesis of Graphene Oxide

Graphene oxide was prepared through oxidation of graphite reported by Hummers *et al.*[13] Graphite powder (0.5 g) and $NaNO_3$ (0.5g) were mixed in 30 mL of H_2SO_4 (95%) at temperature (0-5 °C). The reaction mixture was stirred for 30 min at this temperature followed by the slow addition of $KMnO_4$ (1.5g) to the suspension. The addition rate of $KMnO_4$ was controlled cautiously to keep the reaction temperature lower than 15 °C. There after ice bath was removed, and reaction mixture was stirred at 35 °C for 7 h until it became pasty brownish and then diluted with 50 ml of water. The reaction temperature was rapidly increased to 98 °C, stirred it for 6 h, and then color changed to brown color. Further this solution was diluted by adding 50 ml water and finally treated with 1 ml H_2O_2 (30 wt %) to remove excess $KMnO_4$, if any. For purification, the mixture was washed by rinsing and centrifugation with 10% HCl and then deionized (DI) water several times. After filtration and drying under vacuum at room temperature, the graphene oxide (GO) was obtained as a powder.

5.2.2. Synthesis of CdS/Metal Oxide/GO photocatalyst

CdS/Metal Oxide/GO was synthesized by solid state route. Briefly, 0.2 g of as prepared CdS/Metal Oxide was thoroughly grounded with 1 wt% of as-prepared GO by using mortar pestle for 30 min. The rationale behind the grounding of CdS/Metal Oxide and GO is to make uniform contact between them. The obtained powder of CdS/Metal Oxide/GO was used to examine the effect of graphene oxide on photocatalytic hydrogen generation and for dye degradation under visible light irradiation.

5.3. Result and Discussion

5.3.1. Powder X-ray Diffractogram

Powder X-ray analysis was performed for graphite and GO, in order to confirm the formation of GO (Figure 5.1). Raw graphite showed the very strong peak at $2\theta = 26.8^{\circ}$ (d = 0.33 nm). However, after oxidation this peak of graphite become diminished and a new broad peak appeared at $2\theta = 11.5^{\circ}$ (d = 0.76 nm), which confirm the formation of GO.

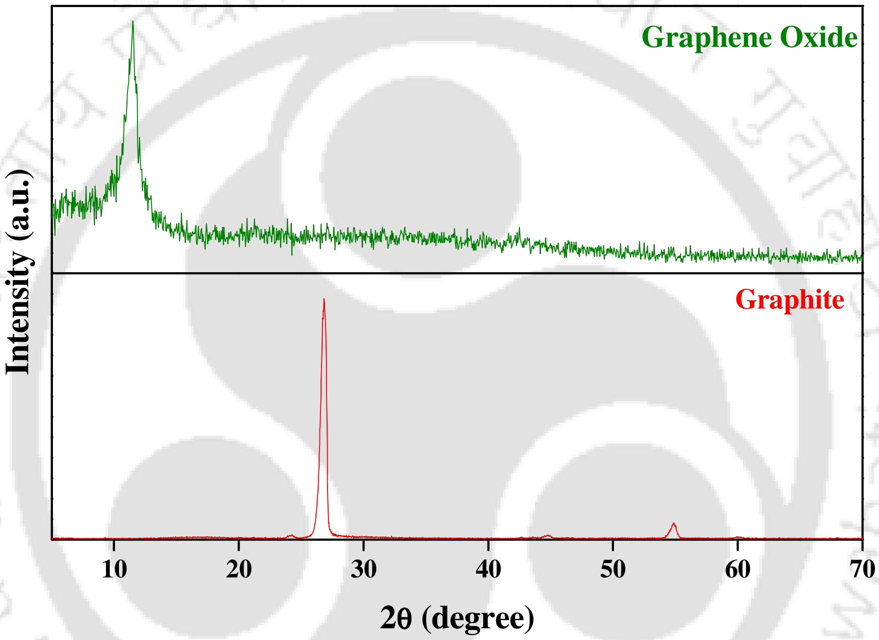

Figure 5.1 Powder X-ray diffraction pattern for graphite and graphene oxide

The purity and crystalline phase of as-synthesized CdS nanoparticles (NPs), ZnO NPs, CdS/ZnO and CdS/Al_2O_3 were analyzed by powder X-ray diffractogram (PXRD). PXRD pattern for all these samples are shown in Figure 5.2. It is evident from PXRD that as-prepared CdS NPs crystallized in the hexagonal structure (JCPDS 06-0314) and ZnO NPs crystallizes in the hexagonal wurtzite phase (JCPDS 05-0664). Interestingly, the same diffraction peaks for CdS can also be seen in the diffractograms for CdS/ZnO and

CdS/Al_2O_3, reveals that crystalline phase of CdS is retained. After the introduction of metal oxide, the PXRD peaks of the sample become narrower due to the improved crystallinity of CdS particles.

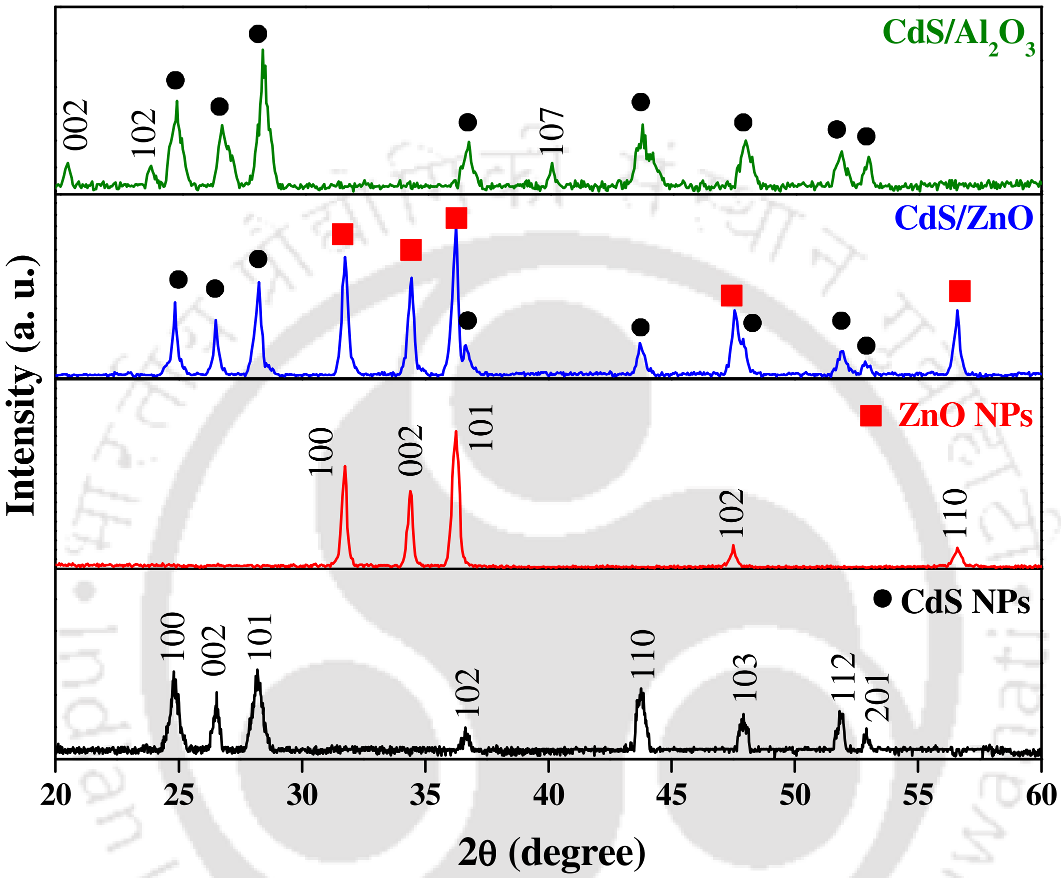

Figure 5.2 Powder X-ray diffraction pattern for CdS NPs, ZnO NPs, CdS/ZnO and CdS/Al_2O_3 heterostructure hybrid materials. PXRD confirms the formation of hexagonal phase of CdS in CdS/ZnO and CdS/Al_2O_3

5.3.2. UV-Vis Diffuse Reflectance Spectra

UV-Vis diffuse reflectance spectra (DRS) of the as-prepared CdS NPs, CdS/Metal Oxide and CdS/Metal Oxide/GO are shown in Figure 5.3**.** Interestingly, all these materials show almost the same absorption profile with a steep absorption edge in ultraviolet and visible range, which corresponds to the band energy components for the individual systems. CdS/ZnO shows two absorption steeps at *ca.* 375 nm and *ca.* 540 nm while CdS/ZnO/GO also have two steeps at *ca.* 350 nm and *ca.* 545 nm corresponding to the ZnO and CdS respectively. On comparative study of UV-Vis diffused reflectance spectra with and without GO for CdS/Metal Oxide, an enhanced photo-response in the visible region is achieved by CdS/Metal Oxide in presence of GO. Thus, CdS/Metal Oxide hybrid with GO is more effective under visible light irradiation.

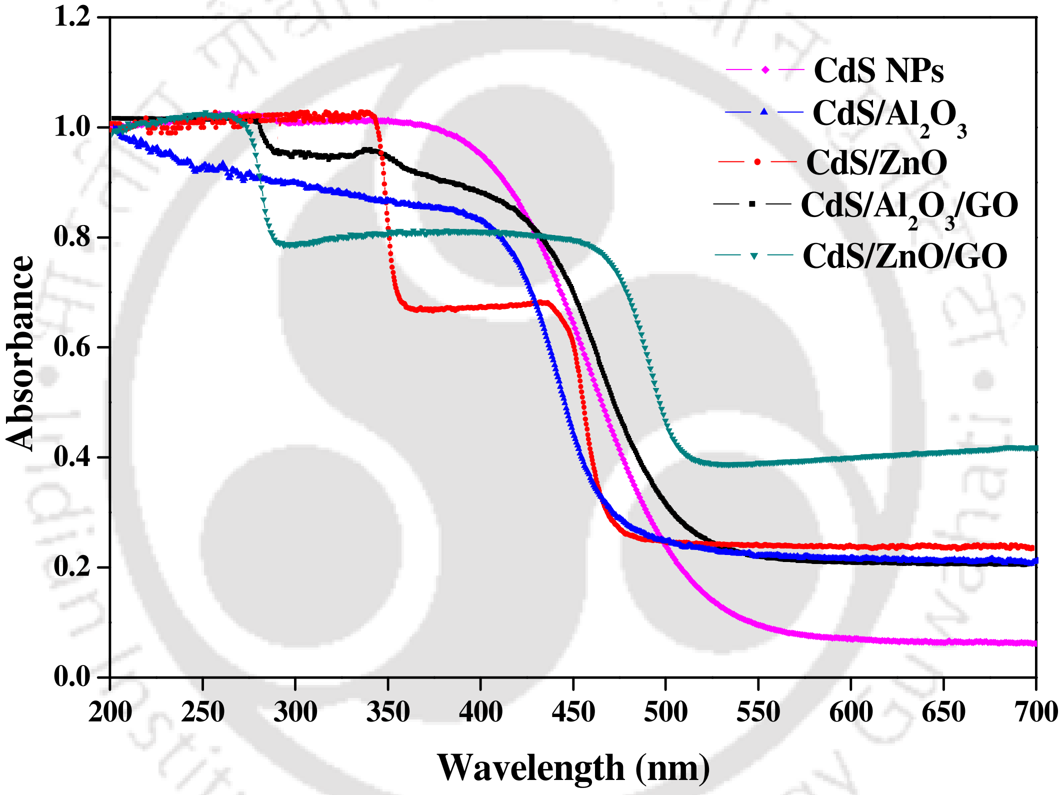

Figure 5.3 UV-Vis diffuse reflectance spectra for CdS NPs, CdS/Metal Oxide and CdS/Metal Oxide/GO

5.3.3. Materials Morphology

In order to investigate the influence of graphene oxide on the morphology of CdS/Metal Oxide nanoparticles, Scanning Electron Microscopy (SEM) experiments were performed for all the samples. SEM images of CdS/Metal Oxide and CdS/Metal Oxide/GO are shown Figure 5.4 and Figure 5.5.

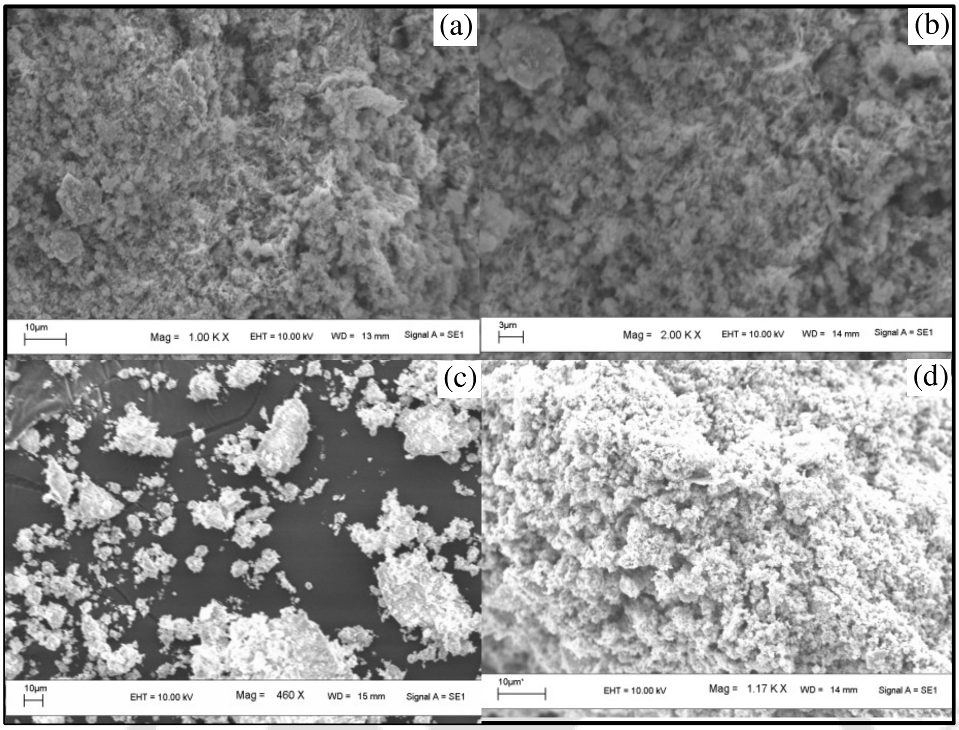

Figure 5.4 Scanning Electron Microscopic images of (a & b) CdS/Al_2O_3 whereas (c & d) $CdS/Al_2O_3/GO$ at different magnification

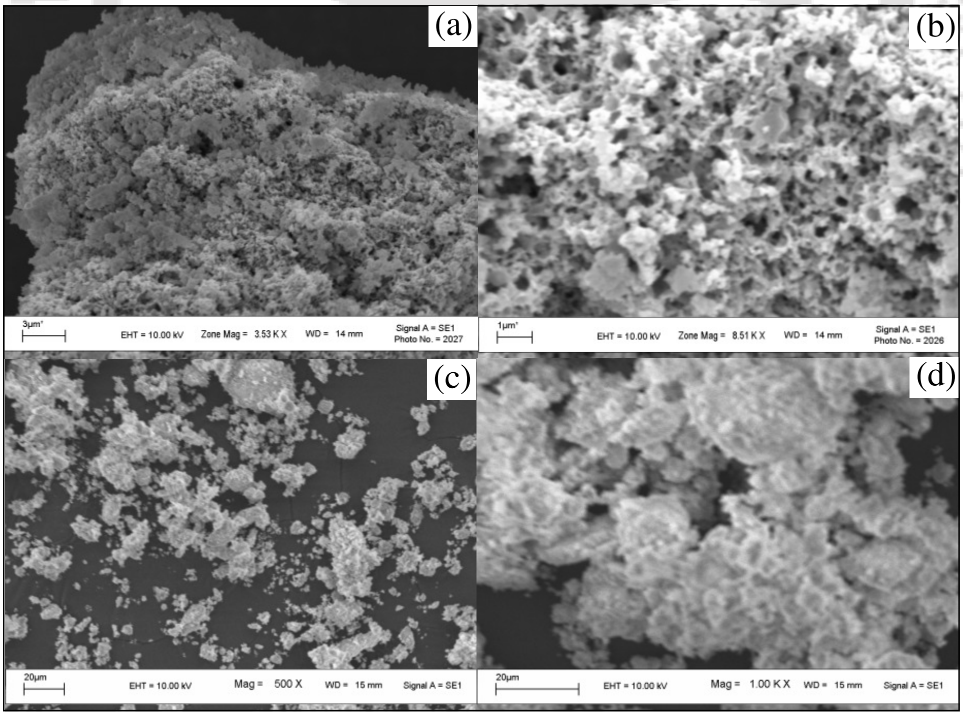

Figure 5.5 Scanning Electron Microscopic images of (a & b) CdS/ZnO whereas (c & d) CdS/ZnO/GO at different magnification

Figure 5.4 a-b and Figure 5.5 a-b SEM images at different magnifications reveal significant aggregation of the CdS/Metal Oxide nanoparticles. Figure 5.4c and Figure 5.5c depicts much less aggregation of particles when GO was introduced in the sample. This indicates that GO might be interacting with the CdS/ZnO and CdS/Al_2O_3 particles to inhibit their aggregation. It has been reported previously that nanoparticles may interact with graphene sheets through physisorption, electrostatic binding or charge transfer interaction.[14]

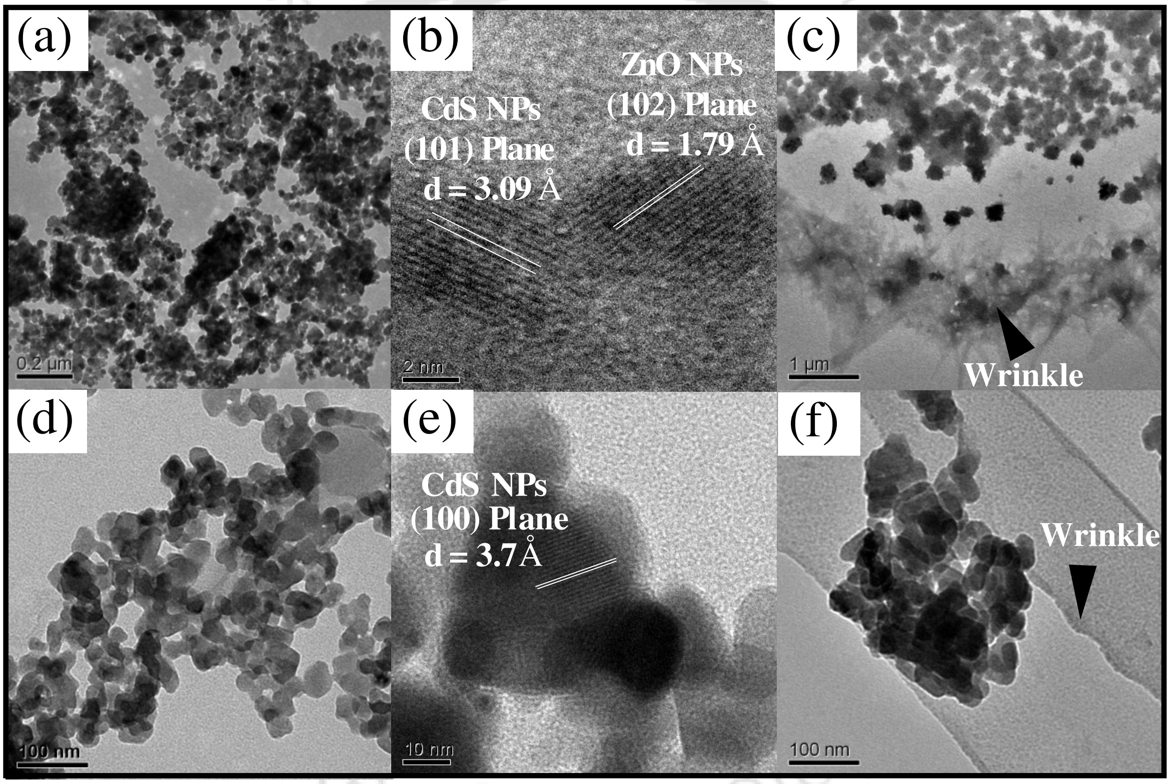

Figure 5.6 TEM images of (a) CdS/ZnO, (b) HR-TEM of CdS/ZnO, (c) CdS/ZnO/GO, (d) CdS/Al_2O_3, (e) HR-TEM of CdS/Al_2O_3 and (f) CdS/Al_2O_3/GO

Transmission Electron Microscope (TEM) images of CdS/ZnO and CdS/Al_2O_3 particles are shown in Figure 5.6a and 5.6d, respectively, which suggest that the nanoparticles are mostly spherical in shape and the size of particles, are in the range of 100 nm for both the samples. The high resolution TEM (HR-TEM) images of CdS/ZnO

(Figure 5.6b) reveals that the crystallized CdS NPS with the lattice spacing of 0.309 nm corresponding to the (101) plane of hexagonal CdS (JCPDS 06-0314), is directly connected with (102) plane of hexagonal ZnO (JCPDS 05-0664) which confirms the formation of nano-composite. The TEM image of CdS/Metal Oxide/GO (Figure 5.6c and 5.6f) shows that CdS/ZnO nanoparticles are present on the GO sheet which has a characteristic wrinkle on the edge (Figure 5.6f).

TEM analysis for CdS nanoparticles and graphene oxide nano-sheet were also performed (Figure 5.7). The TEM images of as-prepared CdS nanoparticles have the particle size of *ca.* 30 nm (Figure 5.7c). TEM analysis of graphene oxide confirms the formation of two dimensional sheet like structure (Figure 5.7e) which are wrinkle on the edge.

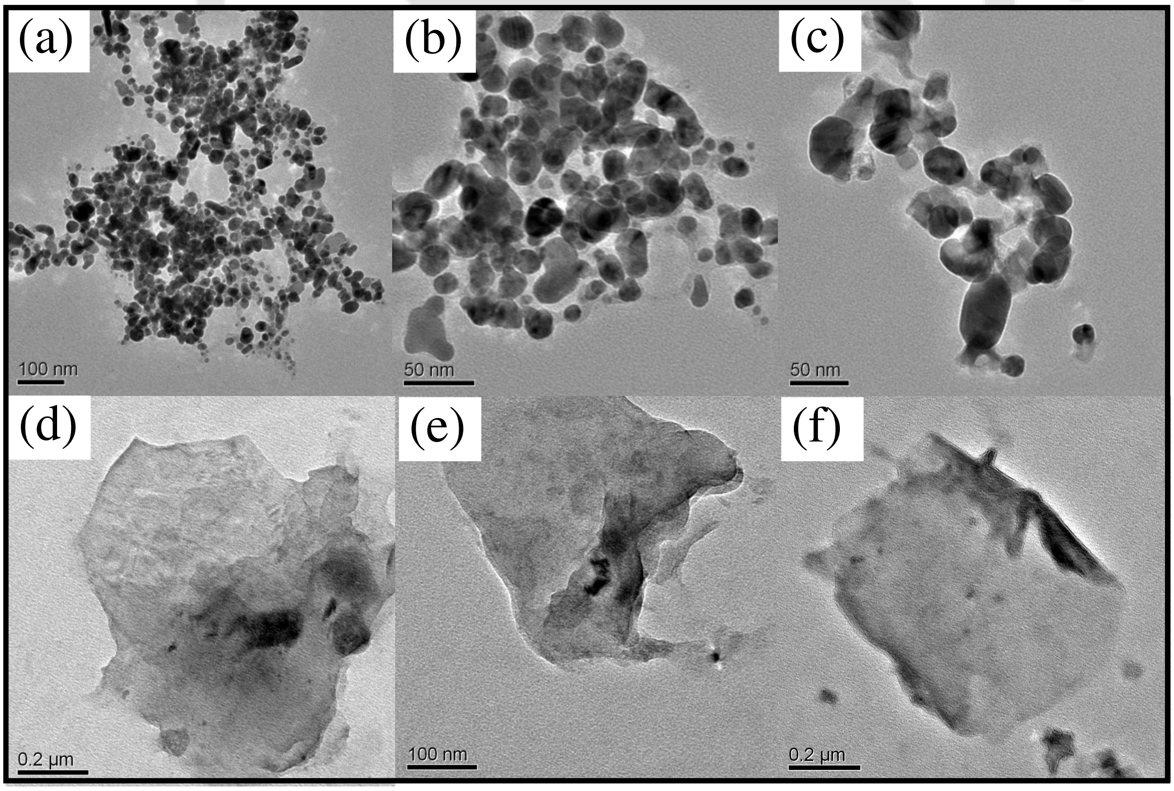

Figure 5.7 TEM images of (a-c) as-prepared CdS nanoparticles (d-f) as-prepared graphene oxide

5.3.4. Photocatalytic Water Splitting for Hydrogen Production

The hydrogen generation ability of as-synthesized CdS/Metal Oxide/GO was determined by performing photocatalytic water splitting experiment. In order to study the relative hydrogen generation with CdS/Metal Oxide/GO, water splitting experiment for CdS NPs and GO were also performed. The H_2 evolution rates under visible light illumination and the surface area of CdS NPs, CdS/ZnO/GO and CdS/Al_2O_3/GO are shown in Figure 5.8. No appreciable hydrogen was detected by GO under visible light radiation.

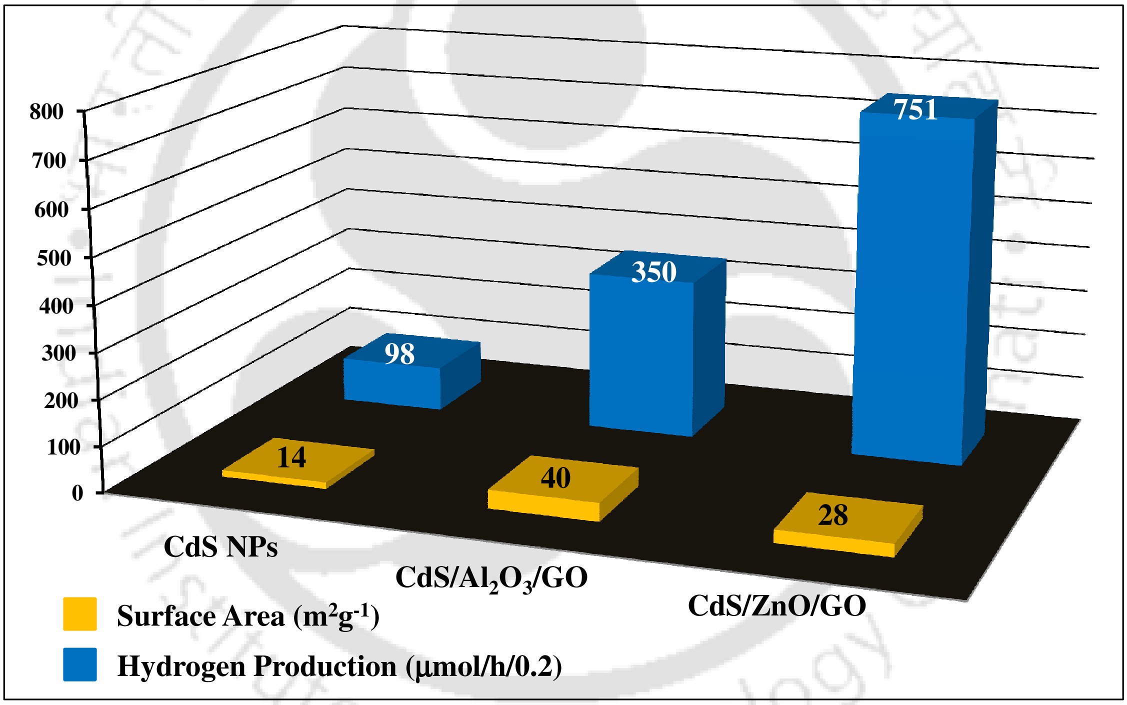

Figure 5.8 Amount of hydrogen produced along with the surface area of CdS NPs, CdS/Al_2O_3/GO and CdS/ZnO/GO photocatalyst under visible light illumination

From Figure 5.8, the enhanced hydrogen production for CdS/Al_2O_3/GO was due to the increased surface area; however, for CdS/ZnO/GO the high hydrogen production efficiency is ascribed due to the enhanced surface to volume ratio for effective charge transfer and less recombination rate of photoinduced charge carriers in comparison to that of CdS NPs. It should be noted that CdS/Al_2O_3/GO has high surface area (40 m^2/g) than

CdS/ZnO/GO (28 m^2/g), but it is the effectual separation of charge carriers in CdS/ZnO/GO which makes it more efficient photocatalyst for hydrogen production.

Based on the reports present in the literature[15-17] we have proposed a mechanism for enhanced photocatalytic hydrogen production in case of CdS/ZnO/GO. To elucidate the mechanism of photocatalytic H_2 generation by the CdS/ZnO/GO, a schematic illustration of the efficient transfer of electrons along with the band positions of CdS and ZnO, was shown in Scheme 5.1.

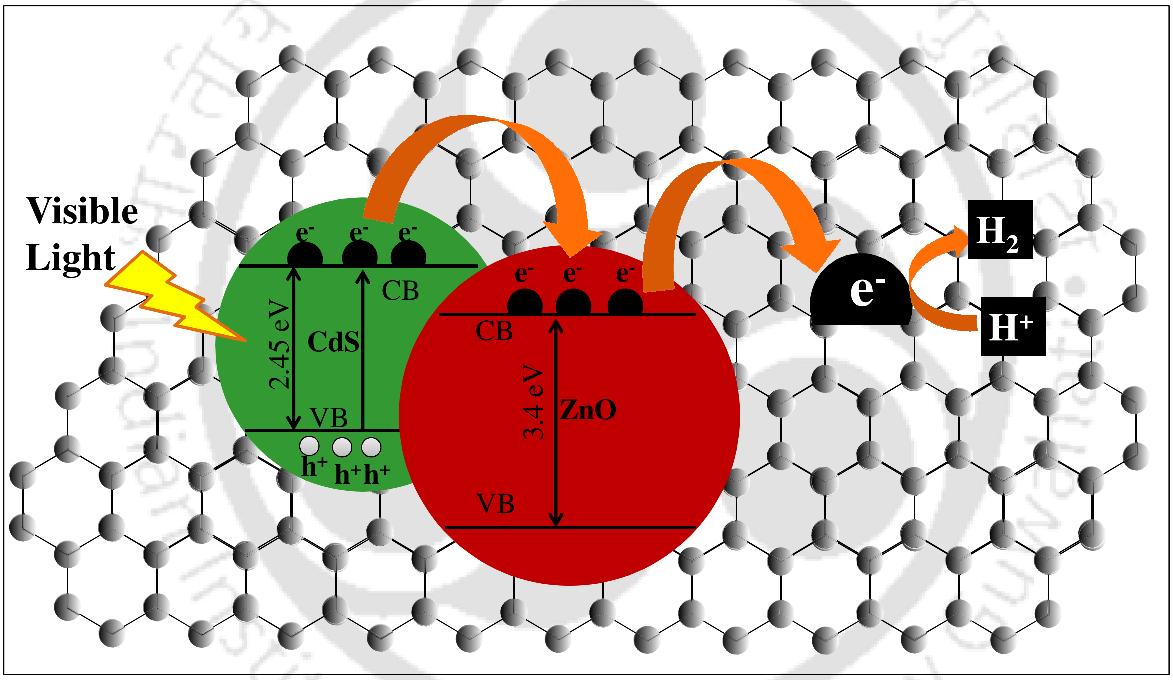

Scheme 5.1 Schematic illustration of the charge separation and the transfer of photo-induced charge carriers in CdS/ZnO/GO system under visible light irradiation; the photo-excited electrons transfer from the CB of CdS to CB of ZnO and from CB of ZnO to the carbon atoms on the graphene oxide sheets, which are easily, react with H^+ to produce H_2

Under visible light irradiation, the electrons (e^-) get excited from the valance band (VB) to the CB of CdS; nevertheless, no charge formation takes place in the CB of ZnO due to its inactivity under visible light. The CB of CdS (–0.88 eV) is in close proximity with the CB of ZnO (–0.22 eV) which facilitates efficient transfer of reductive electrons form the CB of CdS to the CB of ZnO. The reductive electrons in ZnO CB further transfers to the GO because of its high charge carrier mobility, thereby leading the mobilization of these reductive electrons onto the graphene oxide sheet which reduces the recombination rate of photoinduced electrons and holes. Additionally, the unique feature of graphene oxide permits the photocatalytic reaction to take place not only on the surface of semiconductor photocatalyst, but also on the graphene oxide sheet causing enhanced reaction space. Eventually, these reductive electrons react with the adsorbed H^+ ions to produce H_2. Meanwhile, the remaining holes are scavenged by the sacrificial reagents (mixture of Na_2S and Na_2SO_3) present in the solution.

The apparent quantum yield (AQY) for hydrogen generation using CdS/ZnO/GO, CdS/Al_2O_3/GO and CdS NPs was calculated to be around 30%, 14% and 4%. The AQY for CdS/ZnO/GO was almost two times higher than that of hierarchical CdS@ZnO reported in chapter 3A section 3A.3.6. Enhanced hydrogen production rate for CdS/ZnO/GO is mainly attributed to effective charge separation and extended photo-response in visible region due to the presence of GO sheet. The advantage of CdS/Metal Oxide/GO photocatalyst is the enhanced hydrogen production rate without addition of any noble metal co-catalyst such as Pt, Pd, Ru, Rh etc, which makes photocatalytic process inexpensive. Co-catalyst has low band positions due to which the addition of any co-catalyst assists effectual charge separation of electron and holes thereby making the photocatalytic process more efficient. Based on this conviction, CdS/Oxide/GO has been synthesized which has been proven as an efficient photocatalyst by providing large surface area for effective charge transfer and less recombination rate of photoinduced charge carriers due to the presence of GO sheet.

5.3.5. Photocatalytic Dye Degradation

Along with hydrogen production, CdS/Metal Oxide/GO exhibited excellent photocatalytic activity for the degradation of organic dye. The dye degradation experiments were performed using CdS NPs, GO and CdS/Metal Oxide/GO photocatalysts with methyl orange as a reference dye. The degradation of dye with these photocatalysts was studied by measuring the concentration of the dye after irradiation with visible light for varying time periods. The concentrations of dye were measured by monitoring the absorption peak at 464 nm. The absorption spectra of dye with CdS/Al_2O_3 and CdS/ZnO in presence of GO at different time interval are shown in Figure 5.10 whereas with CdS NPs and GO are shown in Figure 5.9. The concentration of un-degraded dye relative to its initial concentration (C/C_0) after visible light irradiation in presence of GO, CdS NPs and CdS/Metal Oxide/GO at different time intervals is shown in Figure 5.11.

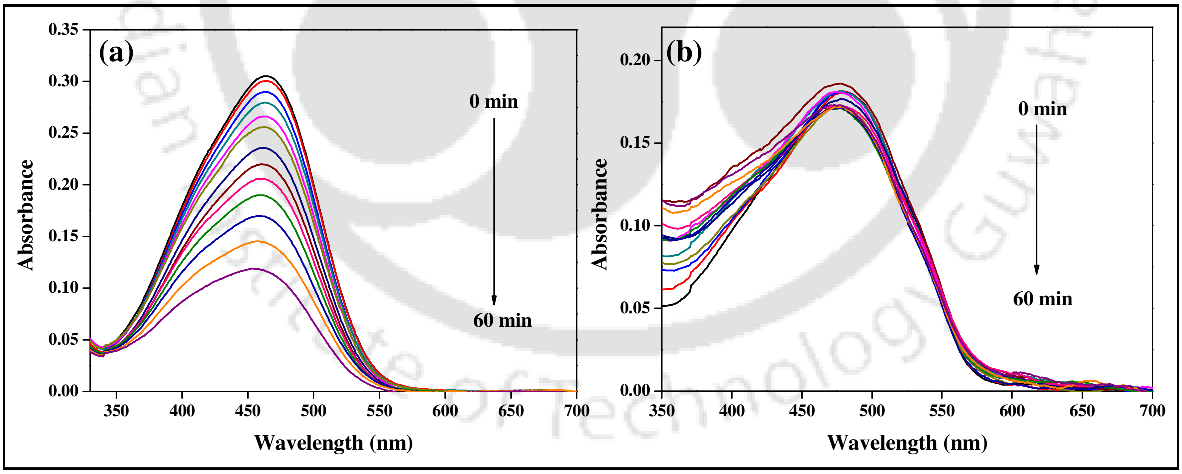

Figure 5.9 UV-Vis absorption spectra of methyl orange with (a) CdS nanoparticles and (b) graphene oxide in 60 min interval

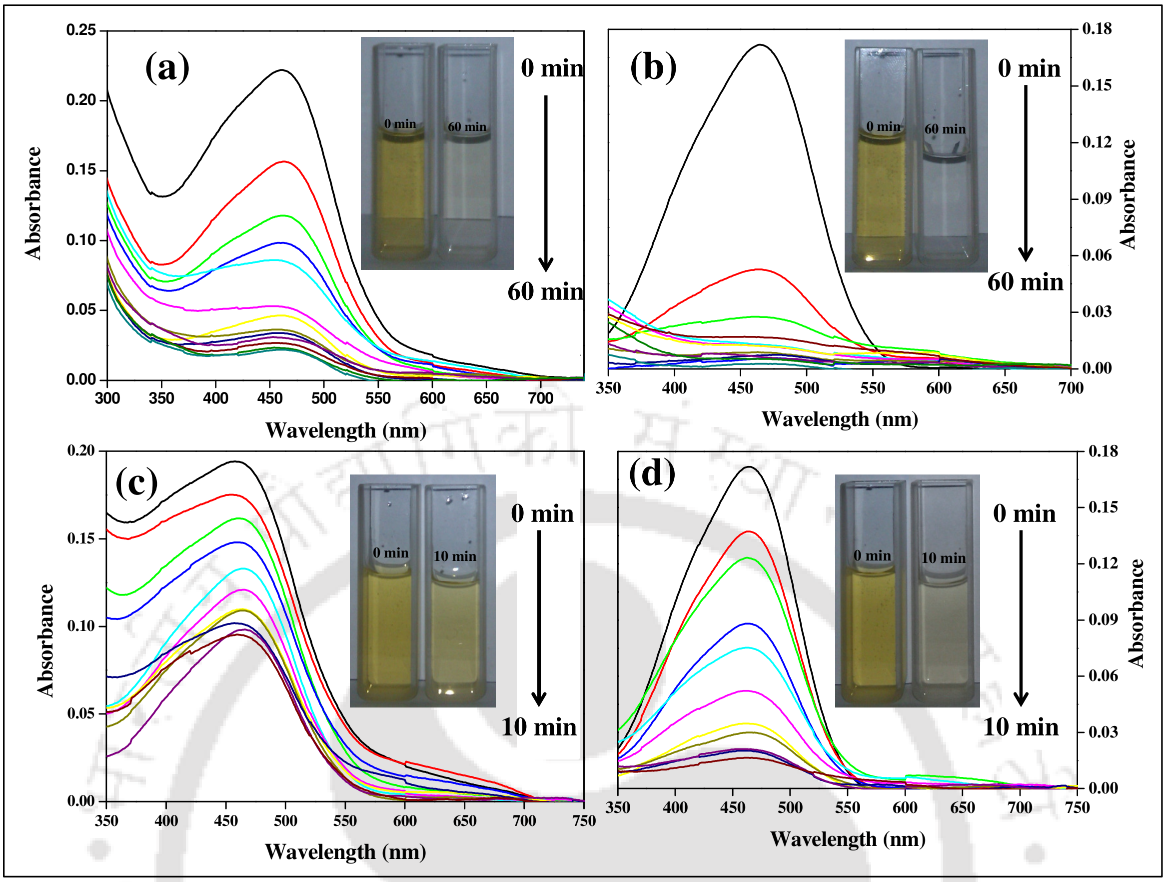

Figure 5.10 UV-Vis absorption spectra of methyl orange with (a) CdS/Al_2O_3/GO and (b) CdS/ZnO/GO in 60 min interval while (c) CdS/Al_2O_3/GO and (d) CdS/ZnO/GO in 10 min interval

From Figure 5.11, highest degradation of dye was achieved for CdS/ZnO/GO compared to CdS/Al_2O_3/GO, CdS NPs and GO. Photodegradation of the dye follows a first order decay kinetics with an apparent first order linear transform $\ln(C/C_0) = -k_{app}t$,[18] as shown in Figure 5.11, where C_0 and C represent the concentration of dye before and after the irradiation respectively, k_{app} is the apparent first-order reaction rate constant representing the reaction rate and calculated from the slope of the plot (Figure 5.11). The degradation efficiencies (E_{ff}) for GO, CdS/ZnO/GO and CdS/Al_2O_3/GO were calculated based on the initial and final concentration of the dye.[19] It was found that within 10 min of irradiation, 85% and 51% of dye degradation was achieved (Figure 5.12) whereas, 99% and 90% degradation occurred within 60 minutes in presence of CdS/ZnO/GO and

$CdS/Al_2O_3/GO$ respectively. The improved efficiency of dye degradation could be mainly attributed to enhanced surface area for mass transfer and facile charge transfer due to the presence of GO sheet which is also responsible for the increased hydrogen production rate.

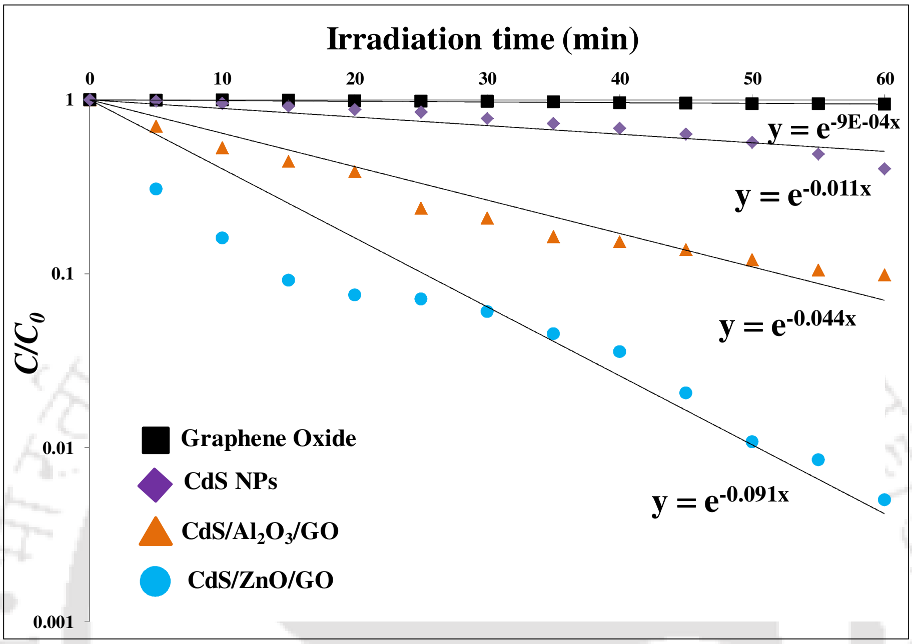

Figure 5.11 Evolution of apparent rate *versus* irradiation time in the presence of GO, CdS NPs, $CdS/Al_2O_3/GO$ and CdS/ZnO/GO photocatalyst at 60 min time interval

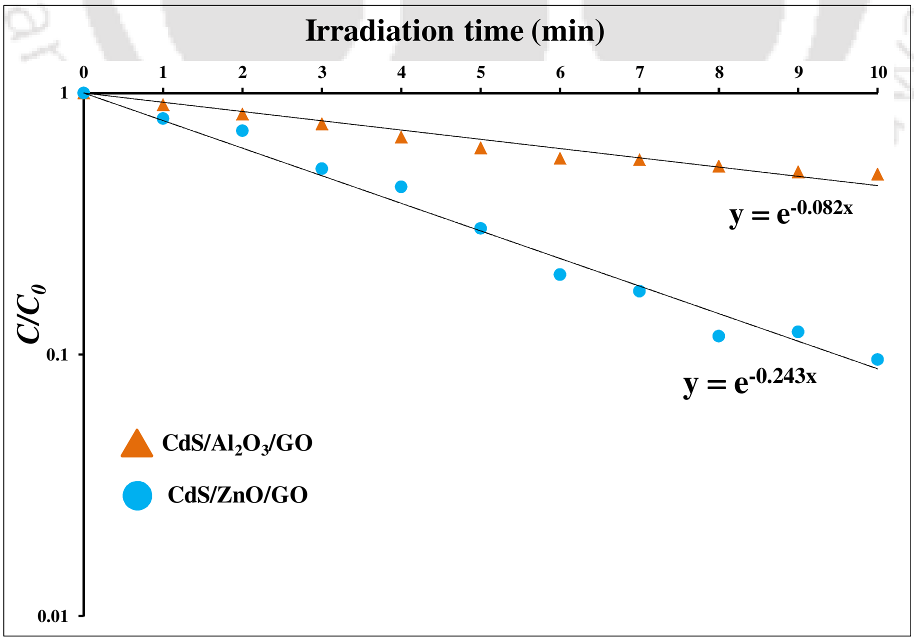

Figure 5.12 Evolution of apparent rate *versus* irradiation time in the presence of $CdS/Al_2O_3/GO$ and CdS/ZnO/GO photocatalyst at 10 min time interval

The proposed schematic of the mechanism for the degradation of methyl orange by CdS/ZnO/GO is shown in scheme 5.2.

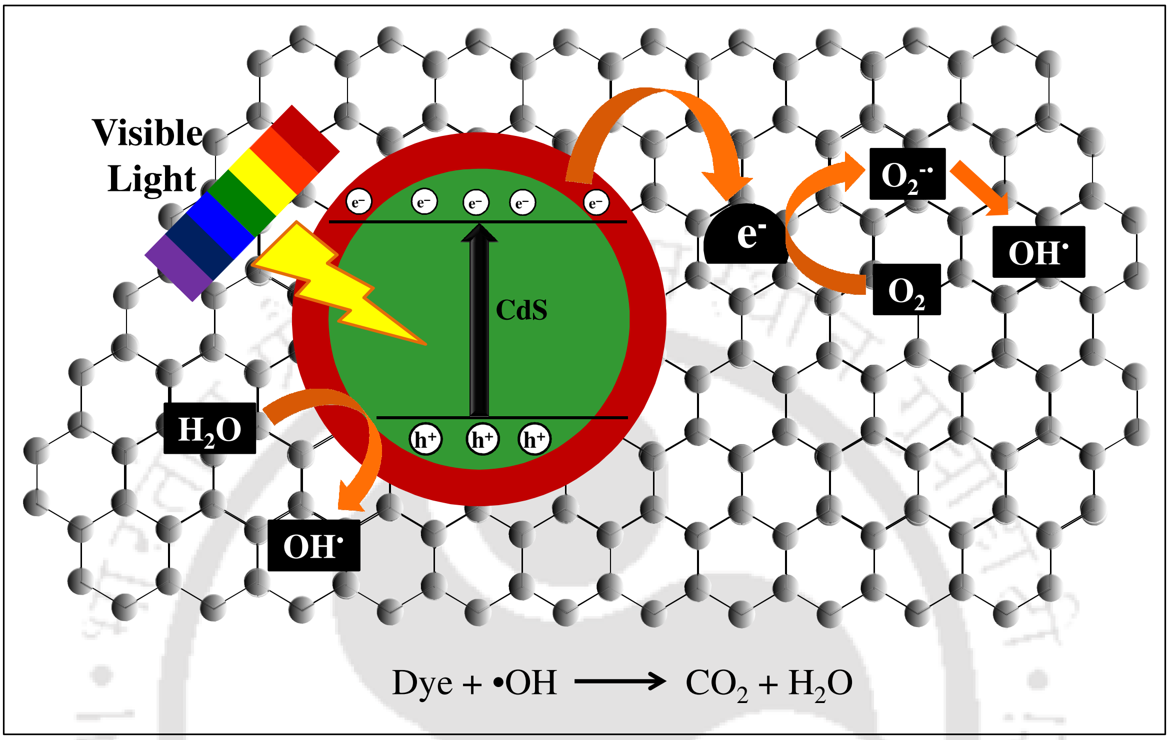

Scheme 5.2 Schematic illustration of the charge separation, transfer of electron to graphene oxide sheet and dye degradation mechanism in CdS/ZnO/GO photocatalyst under visible light irradiation

5.3.6. Proposed Mechanism for the Degradation of Methyl Orange

The proposed mechanism of dye degradation is shown in scheme 5.3 which involves several steps. Irradiation of visible light leads to the formation of electrons in the CB and holes in the VB of semiconductor. The photoinduced electrons in the CB of CdS can get transferred to the CB of ZnO (step 1). The reductive electrons in ZnO CB further transfers to the GO (step 2) which induces the reduction of molecular oxygen O_2 to superoxide radical anion $O_2^{\bullet -}$ (step 3). In aqueous medium, the hole in the VB of CdS oxidizes the water molecule to generate hydroxyl radical (step 4). The hydroxyl radicals can recombine to form H_2O_2 (step 5). H_2O_2 can react with reactive superoxide radical anion to regenerate hydroxyl radical (step 6) which causes the decomposition of organic dye to carbon dioxide and water (step 7).[20]

$$
\begin{array}{lcll}
\mathbf{CdS/ZnO + h\nu} & \longrightarrow & \mathbf{CdS(h^{+})/ZnO(e^{-})} & \textbf{Step 1} \\
\mathbf{ZnO(e^{-})} & \xrightarrow{\textbf{transfer}} & \mathbf{GO(e^{-})} & \textbf{Step 2} \\
\mathbf{GO(e^{-}) + O_2} & \longrightarrow & \mathbf{O_2^{\bullet -}} & \textbf{Step 3} \\
\mathbf{CdS(h^{+}) + H_2O} & \longrightarrow & \mathbf{{}^{\bullet}OH + H^{+}} & \textbf{Step 4} \\
\mathbf{{}^{\bullet}OH + {}^{\bullet}OH} & \longrightarrow & \mathbf{H_2O_2} & \textbf{Step 5} \\
\mathbf{H_2O_2 + O_2^{\bullet -}} & \longrightarrow & \mathbf{{}^{\bullet}OH + {}^{-}OH + O_2} & \textbf{Step 6} \\
\mathbf{Dye + {}^{\bullet}OH} & \longrightarrow & \mathbf{CO_2 + H_2O} & \textbf{Step 7}
\end{array}
$$

Scheme 5.3 Proposed mechanism for the degradation organic dye by CdS/ZnO/GO under visible light irradiation

5.3.7. Reusability of the catalyst for photodegradation of dye

In order to check the reusability of the photocatalyst, organic dye degradation experiments were carried out with catalyst CdS/ZnO/GO.

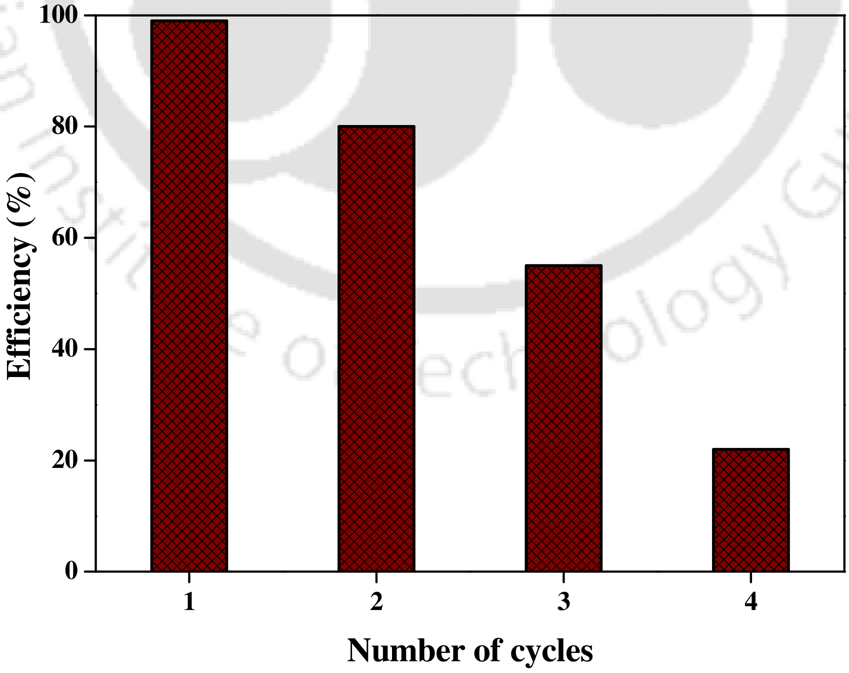

Figure 5.13 Four cycles of the degradation of methyl orange by CdS/ZnO/GO hybrid under visible light irradiation

It was found that up to third cycle more than 50% degradation of methyl orange was achieved (Figure 5.13). Therefore, the stability of the photocatalyst is generally good and has not been photo-corroded during the photocatalytic degradation of reference dye, which is very important for its practical applications.

5.4. Conclusion

1- We have demonstrated a single step hydrothermal synthesis of CdS/Metal Oxide and evaluated their photocatalytic activity with 1wt% graphene oxide.

2- Highly efficient hydrogen production was achieved using the CdS based hybrid materials (AQY ~ 30% for CdS/ZnO/GO; AQY ~ 14% for CdS/Al_2O_3/GO).

3- Additionally, CdS/Metal Oxide/GO displayed highly efficient photodegradation of methyl orange dye.

4- The kinetic study of methyl orange degradation by CdS/Metal Oxide/GO revealed that decay follow first order kinetics with apparent rate constant (k_{app}) value 0.091 min^{-1} for CdS/ZnO/GO and 0.044 min^{-1} for CdS/Al_2O_3/GO.

5- High photocatalytic activity of CdS/ZnO/GO is attributed to the facile charge transfer between the photocatalyst and graphene oxide in comparison to CdS/Al_2O_3/GO.

6- Present study opens up new possibilities for the development of highly efficient visible light driven photocatalyst by the use of graphene oxide.

References

1) Berr, M.; Vaneski, A.; Susha, A. S.; Rodríguez-Fernández, J.; Döblinger, M.; Jäckel, F.; Rogach, A. L.; Feldmann, J. *Appl. Phys. Lett.* **2010**, *97*, 093108.

2) Li, Y.; Du, J.; Peng, S.; Xie, D.; Lu, G.; Li, S. *Int. J. Hydrogen Energy* **2008**, *33*, 2007.

3) Amirav, L.; Alivisatos, A. P. *J. Phys. Chem. Lett.* **2010**, *1*, 1051.

4) Chen, Y.; Wang, L.; (Max) Lu, G.; Yao, X.; Guo, L. *J. Mater. Chem.* **2011**, *21*, 5134.

5) Park, H.; Choi, W.; Hoffmann, M. R. *J. Mater. Chem.* **2008**, *18*, 2379.

6) Wang, Y. B.; Wu, J. C.; Zheng, J. W.; Xu, R. *Catal. Sci. Technol.* **2011**, *1*, 940.

7) Woan, K.; Pyrgiotakis, G.; Sigmund, W. *Adv. Mater.* **2009**, *21*, 2233.

8) Silva, C. G.; Faria, J. L. *ChemSusChem* **2010**, *3*, 609.

9) Leary, R.; Westwood, A. *Carbon* **2011**, *49*, 741.

10) Peng, T.; Zeng, P.; Ke, D.; Liu, X.; Zhang, X. *Energy Fuels* **2011**, *25*, 2203.

11) Wang, P.; Zhai, Y.; Wang, D.; Dong, S. *Nanoscale* **2011**, *3*, 1640.

12) Xiang, Q.; Yu, J.; Jaroniec, M. *Chem. Soc. Rev.* **2012**, *41*, 782.

13) Hummers, W.; Offeman, R. *J. Am. Chem. Soc.* **1958**, *80*, 1339.

14) Williams, G.; Seger, B.; Kamat, P. V. *ACS Nano* **2008**, *2*, 1487.

15) Hotchandani, S.; Kamat, P. V. *J. Phys. Chem.* **1992**, *96*, 6834.

16) Tak, Y.; Kim, H.; Lee, D.; Yong, K. *Chem. Commun.* **2008**,4585.

17) Hou, J.; Wang, Z.; Kan, W.; Jiao, S.; Zhu, H.; Kumar, R. V. *J. Mater. Chem.* **2012**, *22*, 7291.

18) Li, X.; Wang, D.; Cheng, G.; Luo, Q.; An J.; Wang, Y. *Appl. Catal. B: Enviorn*. **2008**, *81*, 267.

19) Zhang, H.; Wu, P.; Li, Y.; Liao, L.; Fang, Z.; Zhong, X. *ChemCatChem* **2010**, *2*, 1115.

20) Konstantinou, I. K.; Albanis, T. A. *Appl. Catal.,B: Enviorn.* **2004**, *49*, 1.

List of publication(s)

1) **Ziyauddin Khan**, Tridip Ranjan Chetia, Mohammad Qureshi; *Nanoscale*, **2012***, 4*, 3543.

2) **Ziyauddin Khan**, Momina Khannam, N. Vinothkumar, Mahuya De, Mohammad Qureshi; *J. Mater. Chem.*, **2012**, *DOI: 10.1039/c2jm31148h.*

3) Dipankar Barpuzary,† **Ziyauddin Khan**,† N. Vinothkumar, Mahuya De, Mohammad Qureshi; *J. Phys. Chem. C*, **2012**, *116*, 150. († ***Authors have equal contribution***)

4) **Ziyauddin Khan**, Dipankar Barpuzary, Oruganti Baswant, Sanjeeb Sutradhar, Mohammad Qureshi; *Mater. Lett.*, **2011**, *65*, 1168.

5) Mohammad Qureshi, **Ziyauddin Khan**, S. Sundar Manoharan; *Chem. Phys. Lett.*, **2009**, *473*, 184.

6) **Ziyauddin Khan** and Mohammad Qureshi; "Graphene Oxide based Visible Light Driven Photocatalyst based on CdS-Metal Oxide hybrids for Highly Efficient Hydrogen Generation and Organic Dye Degradation" (*manuscript submitted*)

7) **Ziyauddin Khan**, Momina Khannam, V. Anil Kumar, C. V. Sastri, Mohammad Qureshi; "Rationally Designed Hierarchical 3D ZnO/CdS and 3D Al_2O_3/CdS Heteroarrays for Efficient Visible light driven Photocatalysis" (*manuscript under preparation*)

8) **Ziyauddin Khan** and Mohammad Qureshi; "Highly Efficient Photocatalytic Hydrogen Generation by Water Reduction from $BaZrO_3$ doped Ta" (*manuscript under preparation*)

Presentation in Conferences/Symposia/Workshops

1) **Ziyauddin Khan** and Mohammad Qureshi, "Synthesis of Novel 3D SrS/CdS Photocatalyst with Excellent Performance for Dye Degradation" *Conference on Photochemistry & Luminescence*, **2012**, *50*.
2) **Ziyauddin Khan** and Mohammad Qureshi, "Synthesis of Novel Hyperbranched 3D SrS/CdS Microstructures: Application towards Efficient Hydrogen Generation and Dye Degradation" *International Symposium on Advances in Chemical Sciences-2012*, **2012**, *30*.
3) **Ziyauddin Khan** and Mohammad Qureshi, "Synthesis of Novel Pompon-like 3D CdS/metal oxide Hierarchical Microstructure and their application towards Efficient Photocatalysis" *International Conference on Nanoscience and Technology*, **2012**, *299*.
4) **Ziyauddin Khan** and Mohammad Qureshi, "Synthesis of Novel Three Dimensional CdS based photocatalyst and its Application for Efficient Hydrogen Generation by Water Splitting" *Indo-US Bilateral Workshop on Nanoparticle Assembly: From Fundamentals to Applications*, **2011**, *65*.
5) **Ziyauddin Khan** and Mohammad Qureshi, "Directed Growth of 1D-Cadmium Sulfide by chemically anchored metal oxide nanoparticle for photocatalytic water reduction" *2nd International Conference on Advanced Nanomaterials and Nanotechnology*, **2011**, *191*.
6) **Ziyauddin Khan** and Mohammad Qureshi, "Design of Systematic Oriented 1D CdS nanowires onto ZnO nanoparticles" *International Conference on Chemistry: Frontiers and Challenges*, **2011**, *25*.

7) **Ziyauddin Khan** and Mohammad Qureshi, “Directed Growth of 1D-CdS by Chemically Anchored Metal Oxide nanoparticle for efficient Hydrogen Generation” *International Symposium on Material Chemistry*, **2010**, *213*.